

Toward Electrochemical Studies on the Nanometer and Atomic Scales: Progress, Challenges, and Opportunities

Sergei V. Kalinin,^{*,†} Ondrej Dyck,[†] Nina Balke,[†] Sabine Neumayer,[†] Wan-Yu Tsai,[†] Rama Vasudevan,[†] David Lingerfelt,[†] Mahshid Ahmadi,[‡] Maxim Ziatdinov,[†] Matthew T. McDowell,[§] and Evgheni Strelcov^{||}

[†]Center for Nanophase Materials Sciences, Oak Ridge National Laboratory, Oak Ridge, Tennessee 37831, United States

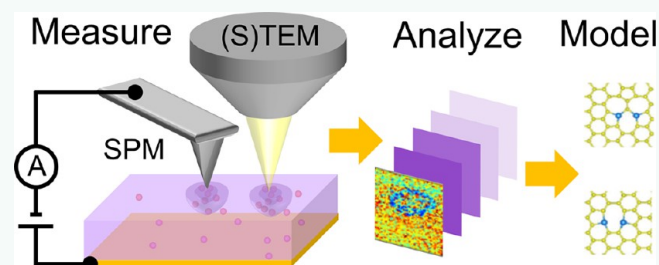
[‡]Joint Institute for Advanced Materials, Department of Materials Science and Engineering, University of Tennessee, Knoxville, Tennessee 37996, United States

[§]George W. Woodruff School of Mechanical Engineering and School of Materials Science and Engineering, Georgia Institute of Technology, Atlanta, Georgia 30332, United States

^{||}Institute for Research in Electronics and Applied Physics, University of Maryland, College Park, Maryland 20742, United States

ABSTRACT: Electrochemical reactions and ionic transport underpin the operation of a broad range of devices and applications, from energy storage and conversion to information technologies, as well as biochemical processes, artificial muscles, and soft actuators. Understanding the mechanisms governing function of these applications requires probing local electrochemical phenomena on the relevant time and length scales. Here, we discuss the challenges and opportunities for extending electrochemical characterization probes to the nanometer and ultimately atomic scales, including challenges in down-scaling classical methods, the emergence of novel probes enabled by nanotechnology and based on emergent physics and chemistry of nanoscale systems, and the integration of local data into macroscopic models. Scanning probe microscopy (SPM) methods based on strain detection, potential detection, and hysteretic current measurements are discussed. We further compare SPM to electron beam probes and discuss the applicability of electron beam methods to probe local electrochemical behavior on the mesoscopic and atomic levels. Similar to a SPM tip, the electron beam can be used both for observing behavior and as an active electrode to induce reactions. We briefly discuss new challenges and opportunities for conducting fundamental scientific studies, matter patterning, and atomic manipulation arising in this context.

KEYWORDS: electrochemistry, atomic manipulation, atomic force microscopy, scanning tunneling microscopy, scanning transmission electron microscopy, electrochemical strain microscopy, Kelvin probe force microscopy, density functional theory, deep convolutional neural network



Electrochemical phenomena underpin the operation of an enormous range of devices and technologies, spanning energy storage and conversion,^{1,2} water desalination,³ electrochemical and electrocatalytic synthesis of metallic and organic compounds,⁴ and applications in information technology devices including memristive and neuromorphic computing and data storage.⁵ Electrochemical phenomena are strongly tied to a material's stability and durability (e.g., corrosion) and are equally important in fields such as biology and medicine, since electrochemical phenomena directly underpin virtually all biological functionalities. Finally, harnessing electrochemical phenomena coupled with other functional behaviors creates pathways to advancing fields such as tunable electronics (coupling between electrochemistry

and physical functionalities),^{6,7} electrochromic devices (coupling to optical properties),⁸ artificial muscles^{9–11} and molecular electromechanical machines^{12–15} (coupling to mechanics), as well as multiple present day, emerging, and serendipitous applications.

For electrochemical processes in condensed phases, spatial heterogeneity is of fundamental importance. Often, the key mechanism(s) governing electrochemical activity involves highly localized centers and regions that include, for example,

Received: April 8, 2019

Accepted: August 21, 2019

Published: August 21, 2019

electrocatalytic sites in catalysis, nucleation sites in electroplating, phase change electrodes, corrosion, insertion sites in intercalation electrodes, and triple-phase boundaries in fuel cells.¹⁶ Macroscopic functionalities are determined by the interplay between the local phenomena at these sites and mass- and electron-transport processes within the material and between the material and the environment. An important aspect of these systems is a tendency for averaging at certain length scales, which allows for the introduction of global macroscopic parameters that describe the overall system. For example, the electrochemical activity of a film can be uniform on length scales much larger than the active site dimensions (say, hundreds of nanometers) but may be highly non-homogeneous on a local (nanometer and atomic) scale. Once such averaged properties are available, they can serve as the basis for construction of macroscopic effective medium models. Some systems, however, do not allow for efficient averaging, such as certain forms of corrosion dominated by a small number of initial nucleation sites or the electrochemical functionalities of single molecular systems. Many physical systems, including ferroelectric relaxors^{17–20} or charge ordered systems^{21,22} that are characterized by degenerate ground states and frustrated interactions, tend to develop complex multiscale heterogeneities.^{23–25} Often, these phenomena are associated with mesoscopic or even macroscopic ionic motion, for example, polarization screening in ferroelectrics.^{26–29} Finally, biological systems are highly structured and heterogeneous, necessitating highly localized studies of local electrochemical activity for applications such as biomonitoring, prosthetics, and brain to computer interfaces.

These considerations present the challenge of probing electrochemical functionalities on the nanometer and ultimately atomic scales. Several recent reviews touched on this subject.^{30–32} Here, we discuss these challenges from the perspective of macroscopic electrochemistry, that is, building upon community-wide accepted macroscopic electrochemical measurements and the associated interpretation and theoretical framework for reducing the measurements to material-specific measurement-independent functionalities. We discuss the challenges in down-scaling classical methods, the emergence of novel probes enabled by nanoscale confinement, and aspects of materials behavior that emerge on the nanoscale as well as the integration of local data into macroscopic models. Scanning probe techniques based on strain and potential detection and hysteretic current measurements are discussed. Finally, we explore the applicability of electron beam methods to probe local electrochemical behavior on the mesoscopic and atomic levels. The application of electron microscopies for the visualization of electrochemical processes is by now well explored. We pose, that much like an SPM tip, an electron beam can be used as an active high-energy electrochemical probe inducing and guiding electrochemical processes on mesoscopic and atomic levels. This will give rise to fundamentally new challenges in quantification and understanding of corresponding mechanisms and new opportunities for mesoscopic- and atomic-scale characterization, matter patterning, and atom-by-atom assembly.

OVERALL FRAMEWORK

The general concept of a measurement involves either pure observation as a function of time or, much more commonly, observation of changes in the system as a function of external stimuli. Challenges in measurement lie in quantification

(measurement errors, noise, *etc.*), the conversion of measured signals to a materials-specific functionality, and selectivity (how other phenomena contribute to the measured signal). For the purpose of this discussion, it is convenient to discuss electrochemical characterization in terms of the locality (global vs local) of the excitation and its detection.

The combination of global excitation and global detection underpins all macroscopic electrochemical measurements based on electrochemical cells or half cells. Here, macroscopic stimuli (bias, current pulse, temperature, illumination) are used, individually or simultaneously, to create the driving force for the desired process. Changes in the system state are probed *via* a macroscopically averaged response, for example, current, reflectance, or changes in the global chemical composition or structure. For nonhomogeneous systems, these measurements offer an average picture of a system's response (meaningful if the system can be self-averaged) and represent the collective effects of local heterogeneities and electronic and ionic transport. The advantage of this approach is that first, it is directly linked to the macroscopic functionality of the application, and second, large detection volumes enable high fidelity measurements.

The global excitation and local detection approaches provide a pathway to probe functionalities locally. Here, of key importance is the detection component, which often relies on an auxiliary signal (*i.e.*, not directly linked to macroscopic functional properties) that serves as a proxy measure of the response. Examples of such approaches include optical microscopy and focused X-ray studies of active electrodes. Similar to global–global measurements, this measurement framework is still directly linked to the macroscopic functionality in the application but provides information on the spatial variability of the process. However, this approach immediately presents the challenges of detection and signal interpretation. Often, the amount of material involved in the local processes is very small, so detection becomes a challenge that is typically addressed using a selective proxy signal, which is related to the relevant electrochemical process (*e.g.*, photon emission or electromechanical strain); however, decoding the relationship between the two to extract the quantitative parameters of the electrochemical process often becomes the bottleneck.

The third paradigm is the local excitation and local detection, which can be seen as a scaling down of the global–global method. Here, the local nature of the excitation allows for probing of the behavior of specific material regions. To highlight the difference with global excitation, consider the example of the electrodeposition process. In a global excitation case, the deposition starts at nucleation centers and rapidly spreads across the surface. Hence, the specific reactivity of most sites toward deposition remains unexplored since they are overtaken by a reaction front initiated elsewhere. Correspondingly, building a comprehensive picture of the deposition process requires measurements at multiple deposition voltages, electrolyte concentrations, or electrode surface states even for the cases when the processes are reversible and possess return point memory. For irreversible processes, only one process history can be observed (*e.g.*, corrosion).

In comparison, local measurements probe the propensity for nucleation at each specific location. The local excitation–local detection measurements offer several interlinked challenges, including scaling down of the classical electrochemical probes, new phenomena that can emerge on transition to the

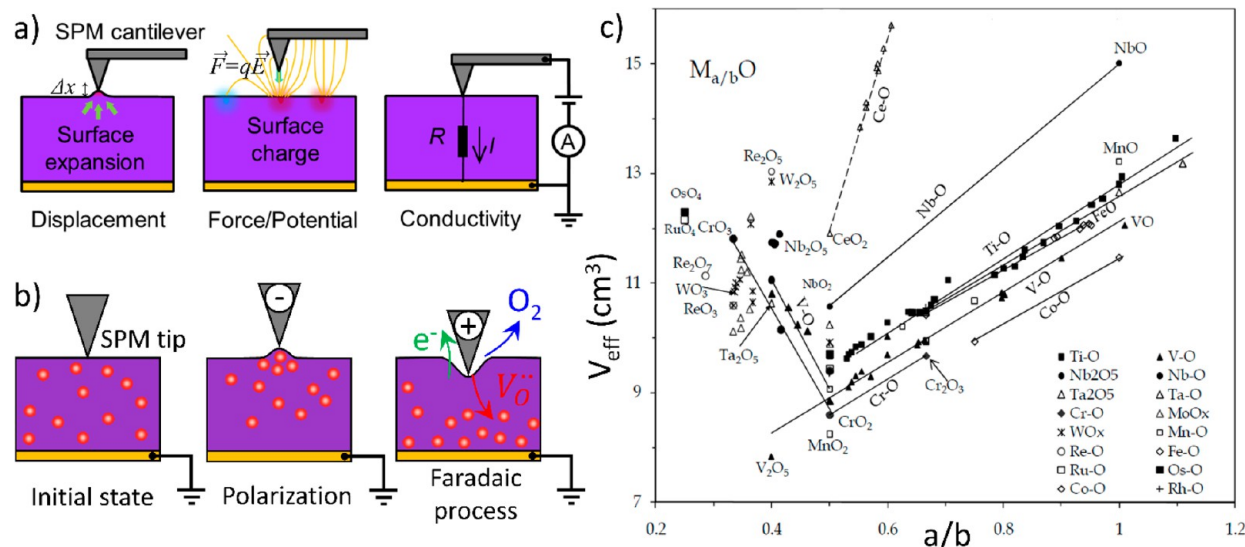


Figure 1. SPM detection methods relevant to electrochemistry. (a) SPM can detect local expansion/displacement, force and local electrostatic potential, or local current associated with an electrochemical process taking place at the tip–surface junction. A solid material under test shown in purple, bottom electrode in yellow. (b) Schematic representation of detecting electrochemical polarization and Faradaic decomposition in solid oxide film *via* registering local expansion–contraction induced by biased SPM tip. Red circles represent positively charged oxygen vacancies. (c) Effective molar volume of metal oxides as a function of oxide stoichiometry as an example of Vegard's law, which links local displacement measured by AFM tip to changes in the chemical composition under it. Adapted with permission from ref 69. Copyright 2008 Springer.

nanoscale, and development of novel probes of local electrochemical behavior (both the probes and theoretical framework for data interpretation in terms of materials-specific functionalities). Notably, they also bring forth a challenge of knowledge integration, that is, knowledge on macroscopic functionalities that is acquired from a set of local materials-specific responses. This challenge, while often underappreciated, is highly nontrivial even when conversion from local measurements to materials properties is straightforward. In comparison, the difficulties are well recognized in the theoretical community involved in, for example, multiscale modeling, where the search for appropriate methods for connecting the length scales based on suitable averaging, information compression,³³ *etc.* remains an active area of research.

Finally, local excitation and global detection is somewhat similar to the local–local case in terms of the challenges and opportunities it offers, with the additional requirement for high selectivity of the probes. Cathodoluminescence (or other optical detection techniques) is the best example of such measurement approaches.

It is also important to mention closely related issues of measurement and modification, which are relevant to local electrochemical probing. Local probes create local stimulus in materials, resulting in changes in their structure or composition. These changes can differ in terms of reversibility ranging from fully reversible to fully irreversible or can comprise both components (*e.g.*, aging in batteries).³⁴ The degree of reversibility is naturally tied to measurement strategies. For example, fully reversible processes enable measurement strategies based on multiple measurements at each spatial location, including lock-in detection, boxcar averaging, and pump-probe approaches. At the same time, irreversible measurements require single-event detection, with the associated measurements challenges. This necessarily affects the spatial resolution, which is now limited by the

size of the region that experiences irreversible change. However, irreversible processes also allow local manipulation and fabrication. While not being the purpose of electrochemical studies *per se*, it is a useful and closely related set of phenomena that can be further employed for meso- and atomic-scale fabrication and will be discussed here.

A second important aspect is the presence of hysteretic phenomena that can necessitate complex measurement modalities based on multiple hysteresis loops as well as exploration using first-order reversal curve methods. Notably, approaches such as the Preisach representation for hysteretic systems cannot be assumed to be applicable *a priori*, and their applicability,^{35,36} role of kinetic effects,³⁷ and physical nature of individual hysterons needs to be assessed in each specific case.^{38–41} Furthermore, even if the system possesses macroscopic return point memory (*i.e.*, a reproducible hysteresis loop), the microscopic return point memory (*i.e.*, identical microscopic states corresponding to a given set of macroscopic descriptors) needs to be established.^{42,43}

The primary strategies for concentrating the stimulus field while also allowing for concurrent nanoscale and atomically resolved imaging are scanning probe microscopy (SPM) and electron microscopy (EM). We note that strategies based on the use of micro- and nanoelectrodes generally do not allow for spatially resolved imaging, since the electrode pattern, while isolating microscopic volume, is fixed. Here, we discuss the advances in both SPM and EM, highlighting basic principles, unresolved challenges, and future opportunities for probing electrochemical phenomena at the nanometer and atomic scales. We note that in SPM and EM, the probe can be used both to visualize the electrochemical process induced by macroscopic stimuli (*e.g.*, macro- or microelectrodes) and to induce an electrochemical process (and detect it) locally. Therefore, throughout the manuscript, we emphasize the connections between mesoscopic imaging in SPM and EM, tip-induced electrochemical probing in SPM on mesoscopic and

atomic levels, and the use of the electron beam as an active electrochemical probe on the mesoscopic and atomic scales.

ELECTROCHEMICAL PROBING BY SCANNING PROBE MICROSCOPY

SPM is based on the principle of a local solid probe (the SPM tip) interacting with the surface *via* short-range repulsive forces or long-range van der Waals, electrostatic, or magnetic interactions. The two primary paradigms for SPM are scanning tunneling microscopy (STM) and atomic force microscopy (AFM). STM is based on the detection of a tunneling current between the biased metallic probe and a conductive sample and using this current as a feedback signal. AFM uses the mechanical force, detected *via* mechanical deflection of a nanofabricated cantilever, the change in oscillation amplitude and phase of the cantilever, or the resonance frequency shift of the cantilever or the tuning fork, as a feedback signal.

The first implementations of force-based surface characterization can be traced to early 20th century profilometric tools, whereas current-based topography tracing was originally reported by the NIST team (Topographiner).⁴⁴ However, the true advent of the field was heralded by the seminal developments by Binnig and Rohrer, who demonstrated that tunneling current detection can be harnessed to yield atomic resolution,^{45,46} instantly gaining the attention of the scientific community worldwide. In the context of electrochemical studies, AFM was first used to measure the topographic changes of the surface of biased macroscopic electrodes submerged in electrolyte.^{47–50} The development of AFM⁵¹ has further created opportunities for probing mechanical,^{52–54} electromechanical,^{55–57} optical,⁵⁸ electrostatic,^{59,60} and magnetic interactions,^{61–63} effectively opening the nanoworld for studies *via* benchtop tools. Many of these characterization modes were incorporated in liquids and therefore can be used for electrochemical characterization.

The measured signals in SPM techniques are generally forces and currents (Figure 1a). For analyses of any SPM modalities, it is important to define which signal is used as the topography feedback to establish the relative position of the probe and the surface and which signal is used for the detection of the associated functionalities. Notably, changes in topography can strongly affect measured signals *via* the finite response time of the electronics or fundamental dependence of the measured interactions on topographic gradients or local curvature, giving rise to topographic cross-talk.⁶⁴ In many cases, the measured signal represents the sum of multiple components that can be fundamentally inseparable given the experimental constraints and fundamental physics of probe–surface interactions. Correspondingly, the development of SPM to address a specific set of phenomena should generally take into account cross-talk and separability issues.⁶⁵

Below, we discuss the SPM-based strategies for probing electrochemical phenomena on the nanoscale. First, strategies based on the detection of bias-induced strains, collectively referred to as electrochemical strain microscopy (ESM) and spectroscopy, are discussed. Next, the application of potential-sensitive SPM for probing the potential distributions in lateral electrochemical devices and the extraction of materials-specific information are discussed. Finally, strategies based on current detection in liquids and hysteretic current measurements for solids are considered.

ELECTROCHEMICAL STRAIN MICROSCOPY

An intrinsic aspect of electrochemical processes in solids is the emergence of electrochemical strains.^{66,67} These can include simple changes in molar volume due to the change of chemical composition and more subtle phenomena associated with the interplay between electrochemical polarization and electrostriction. This intrinsic coupling between electrochemical phenomena and strain enabled the development of SPM applications for electrochemical probing⁶⁸ that exploit the extremely high sensitivity of AFM to vertical displacements. An illustration of this detection mechanism is given in Figure 1b that depicts polarization and Faradaic decomposition of a metal oxide film upon application of a voltage bias to a conductive AFM tip in contact with the surface. The tip serves as an electrode, repelling or attracting mobile oxygen vacancies, while simultaneously detecting local expansion-contraction, which is proportional to the local vacancy concentration. At very high positive voltages, the oxide decomposes under the tip according to $2\text{O}_\text{O}^\times - 4e^- \rightarrow 2\text{V}_\text{O}^\bullet + \text{O}_2\uparrow$ (Kröger–Vink notation used). Figure 1c shows how the molar volume of common metal oxides depends on the oxide stoichiometry⁶⁹ (*e.g.*, concentration of oxygen vacancies), demonstrating the origin of the Vegard strain.⁶⁶ Similar dependencies exist for ionic species other than oxygen vacancies in solid ion conductors (*e.g.*, Li^+ , Na^+ , F^-).

To provide a measure of the AFM sensitivity to local chemical changes in solids, we note that the lattice parameter change of Li_xCoO_2 , one of the most common cathode materials used in Li ion batteries, upon delithiation from $x = 1$ to $x = 0.5$ is about 30 pm.⁷⁰ The sensitivity of AFM to the dynamic surface deflection at the resonance frequency of the cantilever (typically 0.1 to 1 MHz) is on the order of 1 pm, well below the atomic radius of hydrogen of 53 pm. Thus, detecting the lithiation–delithiation process *via* AFM is expected to provide information on the change in the state-of-charge of about 10% over one unit cell of the material. Combined with a typical lateral resolution of ~ 10 nm, AFM allows for probing of the electrochemical transformations in volumes a billion times smaller than those amenable to classical Faradaic current-based measurements. This estimate, while simplified, provides a clear incentive for developing and exploring SPM-based electrochemical probes.

This approach is implemented in ESM⁷¹ and associated time and voltage spectroscopies. In ESM, a high-frequency voltage is applied to the SPM probe in contact with the solid material surface. This probing voltage can induce electrochemical strains, either due to direct coupling to the ionic motion or electrochemical polarization and electrostrictive and flexoelectric strains. For ferroelectric and piezoelectric materials, an additional contribution will be piezoelectric strains, similar to the image formation mechanisms of piezoresponse force microscopy (PFM). This dynamic response is detected by AFM electronics and provides a measure of the local electrochemical activity of the surface. Moreover, the measured response can be influenced by the electric field distribution and ionic concentration as well as nonionic contributions.

To obviate the topographic cross-talk and decouple the topography and intrinsic material responses, the measurements are ideally performed in the band excitation (BE)^{72–74} or dual amplitude resonant tracking (DART)⁷⁵ modes, additionally providing insight into local mechanical properties of the material. Here, we do not discuss the mechanisms of the

topographic cross-talk and its compensation *via* BE and DART but refer the reader to relevant publications and reviews.⁷⁴

ESM has been used to study ion diffusion in a lithium battery cathode.⁷⁶ Figure 2a shows the surface topography of a

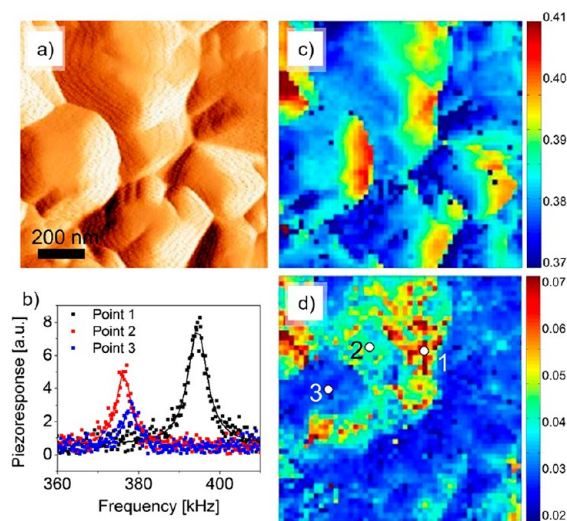


Figure 2. ESM on a LiCoO₂ surface. (a) Deflection signal of $1 \times 1 \mu\text{m}^2$ area showing topography of sample with its grains. (b) Frequency spectra of mechanical response of AFM cantilever at specific locations shown in (d) to periodic voltage oscillations of tip. (c) Resonance frequency and (d) resonance amplitude of contact resonance peak measured in a 50×50 point grid in same area shown in (a). Reprinted with permission from ref 76. Copyright 2010 Springer Nature.

LiCoO₂ (LCO) film with its grainy structure. The surface was overlaid with a 50×50 grid of points, and the tip was sequentially moved to each of these locations, exciting the sample locally with an AC voltage and measuring the local response in the form of deflection *vs* AC frequency curves. The corresponding BE response curves, showing the magnitude of electromechanical response as a function of frequency, are shown in Figure 2b. Note that the material exhibits strong electromechanical coupling, despite the fact that it is nonferroelectric. The resonance frequency extracted from the positions of the resonance curves is shown in Figure 2c and contains information on the mechanical properties of the surface and local topography. Finally, the magnitude of the electromechanical response, which is a measure of local electrochemical activity/ionic transport, is shown in Figure 2d. Note the clear grain contrast, showing that some grains and terminations are electromechanically active and others are not. Notably, the planar grain surfaces parallel to the LCO layers generally exhibit zero response, whereas the slopes show a nonzero response. This generally agrees with the imaging formation mechanism in Figure 2, where the origin of the measured signal is the ionic motion, since in LCO the ions are expected to move along but not perpendicular to the layers.⁷⁷ The apparent dissimilarity between the maps of electrochemical activity (Figure 2d) and topographic maps (Figure 2a,c) attests to the absence of topographic cross-talk and confirms the applicability of the ESM method toward exploring electrochemical phenomena on the nanoscale.

An example for such nanoscale electrochemical studies is mapping of the local activation energy for ionic diffusion, which can be extracted by measuring the ESM signal from a

certain material at various temperatures.⁷⁸ While macroscopic methods can only provide average values for the activation energy, nonhomogeneous cathode and anode compositions, defects, and grain orientations can affect the local activation energy at the nanoscale. Figure 3 shows the local distribution

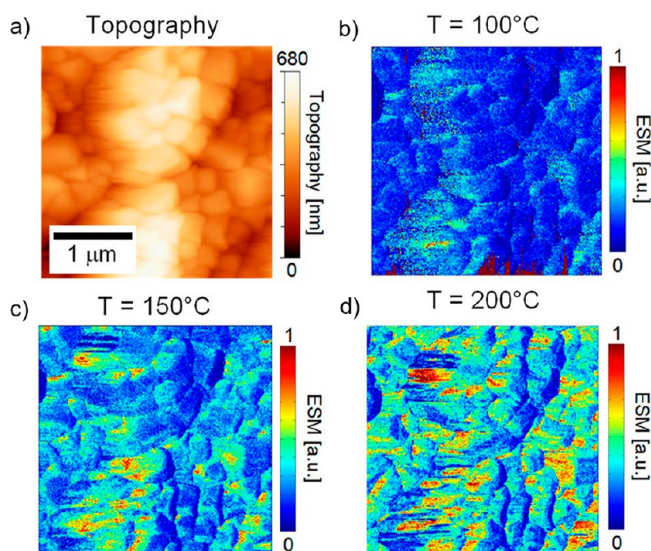


Figure 3. ESM on a LiCoO₂ film. (a) Topography scan and ESM maps measured at (b) 100 °C, (c) 150 °C, and (d) 200 °C. Adapted with permission from ref 78. Copyright 2012 American Chemical Society.

of the ESM signal measured on a LCO film surface (Figure 3a) for three selected temperatures: 100 °C, 150 °C, and 200 °C (Figure 3b–d respectively). The ESM signal reproducibly strengthens with increasing temperature, which indicates an increase in ionic mobility, whereas control experiments allow us to rule out artifacts due to changes in the tip–sample contact, surface water layers, and mechanical properties of the sample.

Overlaying the ESM signal measured at 200 °C on a three-dimensional (3D) plot of the surface topography highlights the spatial distribution of the response and shows the ESM correlation with sample height (Figure 4a). A low response (indicated by the dark blue color) often coincides with very steep height changes. In addition, homogeneous ESM contrast is observed on some grains (*e.g.*, grain marked in red) as well as split ESM contrast on different grain facets (black and orange framed grains).

Arrhenius plots are obtained for each of the red, black, and orange highlighted areas (Figure 4a) by plotting the logarithm of the average ESM signal as a function of $1/T$ ($1/\text{temperature}$) (Figure 4b). The activation energy for each area is extracted from the slope of the Arrhenius plot, which is multiplied by a factor of 2 that takes into account that the ESM signal scales with the square root of the diffusion coefficient. An activation energy of 0.26 eV is obtained, which is in good agreement with macroscopic measurements⁷⁹ and theoretical calculations.⁸⁰ The different ESM signal strength obtained for grains that show similar activation energies originates from strongly anisotropic Li-ion diffusivity⁷⁷ that results in alignment of diffusion paths along the LCO {100} planes. If there is an angle between the driving electric field and the preferred diffusion direction, the effective field component acting on the Li-ions is lowered, resulting in a change of the ESM signal.

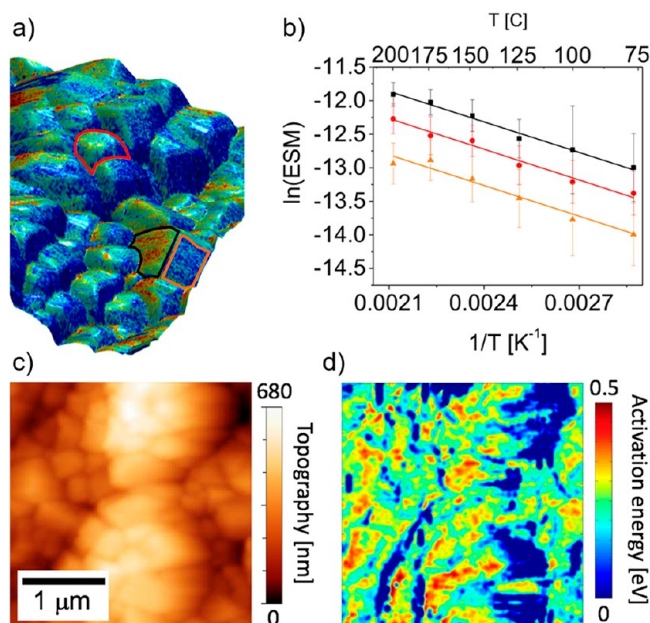


Figure 4. Activation energy analysis. (a) Three-dimensional topography plot overlaid with the local ESM signal measured at 200 °C. (b) Arrhenius plots for the grains framed in red, black, and orange in (a). (c) Topography image and (d) corresponding map of calculated activation energy. Adapted with permission from ref 78. Copyright 2012 The American Chemical Society.

Other factors that contribute to the ESM, such as the Vegard tensor and Poisson ratio, are dependent on crystallographic orientation, which varies within the measured sample area. Therefore, the ESM signal provides qualitative information regarding the number of Li ions that are moved by the probing field in the different grains. However, some spatial differences in activation energy occur across the grains (see Figure 4c,d). Low-energy values coincide with steep sample areas, indicating that a poor tip–sample contact is the origin of this contrast. Within grains, the activation energy is quite homogeneous, with some grain boundaries showing lower values. The concept of using temperature-dependent ESM to extract the local activation energy can be extended to other materials exhibiting volume changes dependent on changes in local ion concentrations.

The strain-based detection approach embodied in ESM can be further extended to probe local time and voltage dynamics. Here, in addition to the probing AC voltage excitation of small amplitude, a DC bias offset on the tip is varied with time, and the dynamic response is measured.^{71,76,81,82} A prototypical example of such measurements is voltage spectroscopy, where the DC bias follows a triangular ramp and the response is measured *vs* the applied voltage, giving rise to hysteresis loops similar to cyclic voltammetry (except that surface displacement rather than electrode current is measured).^{83,84} However, care must be taken that the measured signal does not originate from electrostatic interactions, especially if charge injection into the sample surface occurs as is commonly observed.^{85,86}

AC and DC probing voltages used in ESM further allow for studying irreversible electrochemical processes on the nanoscale.^{81,82} This approach is illustrated for resonance frequency measurements on a Li-ion conducting glass-ceramic (LICGC) similar to the example in Figure 1b, where a low voltage applied to the sample *via* an AFM tip polarizes it locally,

whereas a larger bias triggers a Faradaic reaction under the tip.^{81,82} Under the biased tip, LICGC undergoes the chemical reaction $\text{Li}^+ + e^- \rightarrow \text{Li}_{(s)}$ resulting in the formation of Li-metal particles on the surface that are dependent on the applied voltage. This chemical process manifests as shifts in the resonance frequency of the ESM signal, reflecting topographic changes during particle nucleation. Correspondingly, voltage values at which the frequency jumps occur provide information on the local nucleation bias. Using these jumps as a feedback can therefore provide a map of nucleation biases across the sample surface.

Similar approaches can be implemented using current-based and displacement-based measurements. Figure 5 shows the

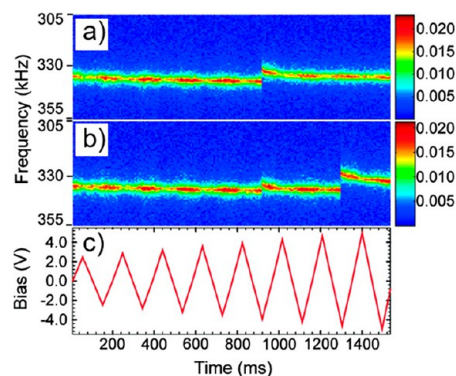


Figure 5. ESM as a function of frequency, bias, and time. Two-dimensional ESM amplitude spectrogram with (a) one and (b) two frequency shifts associated with particle formation. (c) DC voltage envelope waveform applied to a LICGC surface. Reprinted with permission from ref 81. Copyright 2011 The American Chemical Society.

ESM signal as a function of the AC voltage frequency, the applied DC bias, and time. The time and bias at which these shifts (discontinuities in the resonance frequency trace) occur indicate a nucleation bias of -4 V for electrochemical Li-ion extraction from the LICGC surface. This irreversible ionic transport can further be characterized by analyzing the number of Li atoms in a formed particle, which can be estimated from the area and volume of the particle. Figure 6a shows a topographic image of particles formed on LICGC after applying DC voltages from 3 to 6 V. The bias dependence of the particle volume and area is shown in Figure 6b, which indicates an activation voltage of ~ 4 V and a linear size–bias relationship at higher biases. Activation biases provide information on the nucleation bias (or reaction onset voltage), whereas the signal evolution after nucleation allows insight into the kinetics of the bias-induced particle growth.^{81,82,87–89} Since the reduction reaction requires an equal number of electrons and Li ions, the ratio between Li atoms in a particle and the number of transferred electrons as inferred from current measurements is expected to be equal to 1. While small deviations might be ascribed to experimental conditions, values close to 1 observed experimentally (if the reaction is performed in a glovebox) provide further evidence that the observed electrochemical reaction can indeed be ascribed to the reduction of Li^+ ions to Li metal.

In addition to detecting the AC component of the ESM signal and acquiring topography scans after voltage spectroscopy, electrochemical reactions associated with particle growth can also be traced by monitoring a calibrated AFM z-sensor,

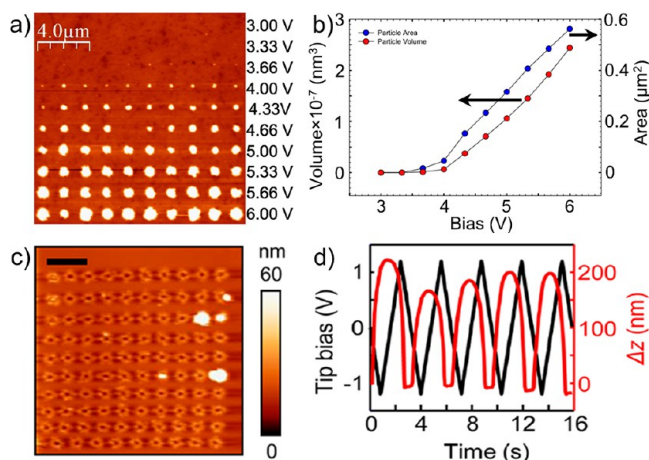


Figure 6. Formation of metallic nanoparticles on ion conductor surfaces. (a) Topographic image of LICGC surface after applying DC voltages of different amplitude with AFM tip. Particles of metallic lithium grow at tip parking locations. (b) Particle volume and area as a function of bias from (a). Reprinted with permission from ref 82. Copyright 2012 IOP Publishing. (c) Topographic image of silver-ion conductor after bipolar voltage sweep was applied to surface with AFM tip. Particles grow and partially dissolve at tip parking locations. (d) Voltage waveform and AFM z-sensor reading as a function of time showing how metallic silver particles reversibly form. Reprinted with permission from ref 90. Copyright 2015 The American Chemical Society.

providing calibrated, real-time information on the vertical cantilever displacement. This approach is especially advantageous if the studied electrochemical processes lead to particle formation, which can then be monitored while simultaneously applying DC voltages. This method for strain-based detection of ionic mobility was used to gain insight into local ionic processes in silver-ion conducting glasses and copper indium thiophosphate CuInP_2S_6 (CIPS).⁹¹ Figure 6c shows a topographic image of the surface of a silver-ion conducting glass that was biased with the AFM tip. Metallic silver particles formed and partially dissolved at the tip parking locations following the reaction: $\text{Ag}^+ + e^- \rightleftharpoons \text{Ag}$. The bias waveform and change in the z-sensor signal over time are shown in Figure 6d. Unlike more reactive lithium, silver particles can grow and be dissolved reversibly. Yang *et al.*⁹⁰ studied the growth mechanism of silver particles, their interactions, and the influence of humidity on the system, which reveal the nonlocality of AFM electrochemical measurements due to restriction of the counter-reaction.

CIPS, possessing ion conductivity (Cu^+), also shows reversible particle formation on the surface that can be controlled by voltage polarity, sample composition, frequency, and temperature. At negative voltages, big particles having a height of ~ 10 nm form on the CIPS surface, which is not observed on an interspersed, Cu-free $\text{In}_4(\text{P}_2\text{S}_6)_3$ (IPS) phase (Figure 7a). Cycling back to positive voltages reverses the particle formation, as indicated by displacement values close to 0 nm. The shape of the displacement curve indicates history dependence, with high values only occurring if preceding voltages are negative.⁸² The map of maximum displacement shown in Figure 7b highlights the difference in particle growth between CIPS (high values) and IPS (dark areas), indicating that the electrochemical reaction for particle growth involves Cu-ions and that the resulting particles are metallic Cu. Moreover, the observed displacement exhibits a pronounced

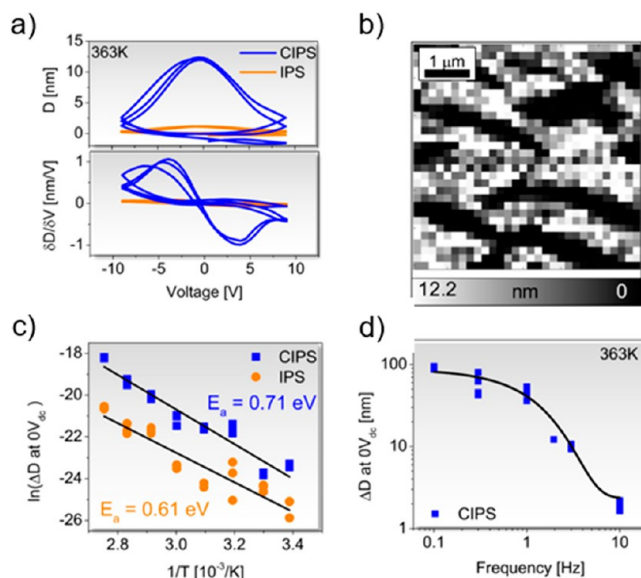


Figure 7. Reversible particle formation in CIPS. (a) Vertical cantilever displacement, D , and derivative as a function of applied voltage at 363 K. (b) Spatial distribution of maximum displacement at 363 K corresponding to chemical phases, where low values correspond to Cu-free IPS and high values correspond to CIPS. (c) Arrhenius plots and extracted activation energies for CIPS and IPS. (d) Frequency dependence of displacement measured at 0 V within CIPS area. Reprinted with permission from ref 91. Copyright 2018 American Chemical Society.

dependence on temperature and frequency. Similar to the temperature-dependent ESM signal discussed above, activation energies can be extracted from Arrhenius plots of the cantilever displacement, as shown in Figure 7c for CIPS and IPS (0.71 and 0.61 eV, respectively). As characteristic of slow ionic diffusion processes, the observed displacement decreases with increasing frequencies (Figure 7). Therefore, monitoring the vertical displacement of the cantilever during voltage spectroscopy can provide a wealth of information on the nature and characteristics of ionic processes and electrochemical reactions.

This brief summary further points to the challenges associated with the ESM measurements. The first is quantification of the measurements, that is, translation from the measured ESM signal on the photodetector to a material expansion in pm/V. While simple calibration of the cantilever sensitivity in the noncontact modes is a well-established practice in SPM,^{93–96} contact mode calibration represents a significantly more complex problem due to coupling of the higher-order flexural modes.⁹⁷ Depending on the ratio between the cantilever spring constant and contact stiffness of the tip–surface junction, the corresponding calibration factors can become zero or can change sign. Correspondingly, quantitative measurements of the ESM signal require either precise calibration or use of alternative detection schemes based on interferometric systems.⁹⁸

The second key consideration is the separation between electromechanical interactions and electrostatic forces. Here, a large electric field at the tip–surface junction results in electrostatic interactions between the probe and the surface (somewhat similar to the adhesive forces in Maugis models for contact mechanics) and the resultant surface deformation. Notably, from classical electrostatics, the field structure of a metallic tip in contact with a dielectric surface contains an

essential singularity at the perimeter of the contact zone, precluding direct numerical evaluation of these forces.^{99,100} Experimentally, for materials with a strong electromechanical response, the bias-induced strain dominates the effect of the electrostatic forces. However, these can be comparable for electrochemical systems and weak piezoelectrics. At this point, no strategies exist for separating these interactions beyond classical tuning of the sample composition and environment.⁶⁵

A third challenge in determining the responses is the relationship between measured electrochemical strain and materials properties, including diffusion coefficients and ionic concentrations. This requires the development of analytical and numerical models for the ESM response, along with strategies for data inversion. The analytical theory of ESM was developed by Morozovska *et al.* for one-dimensional (1D)⁶⁸ and 3D rotationally invariant cases.⁸³ For diffusion controlled cases in a linear material, where the SPM tip is considered as a source of mobile ions (generated as a result of a fast voltage controlled reaction process) and the electroneutrality in the material is maintained, the analytical solutions can be readily obtained.⁸³ For more complex cases including migration–diffusion dynamics and considering exclusion effects, a number of numerical analyses have been reported.^{101,102}

Generally, advances in modern numerical techniques and the relative simplicity of the tip–surface junction geometry render numerical solutions of the drift-diffusion equations relatively straightforward. Worthy of attention, however, is the role of exclusion effects, high-field effects that can significantly affect transport coefficients, and especially the appropriate boundary conditions on the tip–surface junction for nonblocking surfaces. Second, the development of numerical schemes for data inversion and recovery of materials properties from the measured signals are extremely important given the numerical model and necessitate development of relevant Bayesian inference and uncertainty quantification schemes. Therefore, further analysis is necessary to establish approximate numerical relationships between electrochemical mechanisms and materials responses. However, once implemented, the true potential of ESM becomes extremely promising, enabling full characterization of electrochemical processes on the nanometer level, including the role of individual defects on electrochemical reactivity and exploring collective reaction phenomena.

Two more factors should be noted in this regard. The first is the intrinsic electrochemistry of the surface, including electron and ion traps due to surface disorder and the electrochemistry of the surface water layers.^{103–105} Given the extremely small signal generation volume of SPM and the higher mobility of surface ions, surface phenomena can strongly contribute to the measured signal. While being detrimental to probing intrinsic electrochemical phenomena of the studied material, it nonetheless opens a pathway for probing surface electrochemistry as discussed in more detail in the following sections.

Second of interest is the multimodal imaging by ESM and structure- and chemically-sensitive probes. Focused X-ray methods provide information on a material's structure with ~10 nm resolution, allowing insight into the nature of grain boundaries, extended defects, and dislocations.^{104,106–108} Techniques such as micro-Raman^{109–111} and time-of flight secondary ion mass spectrometry (ToF-SIMS) provide information on the chemical state of the surface. Recent studies enabled by combined AFM-ToF-SIMS instruments have provided insight into the chemical changes during AFM

scanning and biasing.^{112–116} Further developments of these methods and the associated workflows based on image registration will enable comprehensive probing of chemistry and electrochemistry of surfaces and nanoscale volumes and elucidating the concurrent structural and chemical changes.

POTENTIAL DETECTION

The key element of macroscopic electrochemistry is the concept of the electrode potential of a given reaction, which is measured or calculated relative to a reference electrode.¹¹⁷ While reference electrodes were successfully incorporated into scanning electrochemical microscopy¹¹⁸ and similar SPM techniques involving a liquid electrolyte (discussed below), their use in all-solid-state SPM measurements is extremely challenging and has not been realized experimentally (in part due to large voltage drops in low-conductivity systems, commonly referred to as IR drops). Nevertheless, since the AFM is sensitive to local electrostatic charge and force, it can be used to detect the sample's surface potential and its evolution, which can be a substitute for the electrode potential. The electrostatic force acting on a conductive AFM tip oscillating above a sample surface (noncontact or tapping mode) brings about a shift in the cantilever's oscillating frequency, amplitude, and phase. Thus, the simplest method of detecting the distribution of charged species (ions) in a sample is tracking the resonance amplitude or frequency (electrostatic force microscopy (EFM) and its derivatives).^{119–122}

A more advanced technique, Kelvin probe force microscopy (KPFM), converts the shifts in the resonance amplitude or frequency into the contact potential difference between the tip and sample. The conversion can happen in real time *via* an electronic feedback loop that minimizes the shifts (classical closed-loop KPFM)¹²³ or *via* postprocessing of the collected data (open-loop detection).^{124,125} The band diagrams for noninteracting electronically conductive sample and tip are shown in Figure 8a, left panel. Due to the difference in their Fermi levels (E_F), both objects will have different work functions (ϕ) given by the difference in E_F and vacuum level, E_V : $\phi = E_V - E_F = \Delta\chi - \bar{\mu}$ ($\Delta\chi$ is the surface dipole barrier and $\bar{\mu}$ is the chemical potential of electrons in the material).^{126,127} When the sample and tip are allowed to exchange electrons (*via* tunneling, direct contact, or a connecting wire), their Fermi levels will equilibrate and both objects will become charged, with the contact potential difference (CPD) between them given by $V_{CPD} = \frac{\phi_{tip} - \phi_{sample}}{e}$, where e is the elementary charge (Figure 8a central panel).¹²⁸ The CPD (or Volta potential difference) creates an electrostatic force on the cantilever, which can be nullified by applying an external voltage equal to V_{CPD} (Figure 8a right panel). The tip's work function can be determined *via* calibration against highly oriented pyrolytic graphite, and, thus, the KPFM effectively probes the sample's work function. If the sample is biased externally, the total KPFM signal will be the sum of the V_{CPD} and that external bias. While most of the samples can be grounded to exclude this additional contribution, electrochemical devices, such as batteries and fuel cells, usually have built-in voltages that cannot be nullified and their KPFM signals are intrinsically convoluted. KPFM measurements on electronic insulators are usually interpreted in terms of electrostatic potential created by surface or bulk charges existing in the sample,¹²⁸ which can be highly mobile in the case of a pure ionic conductor. KPFM can provide information

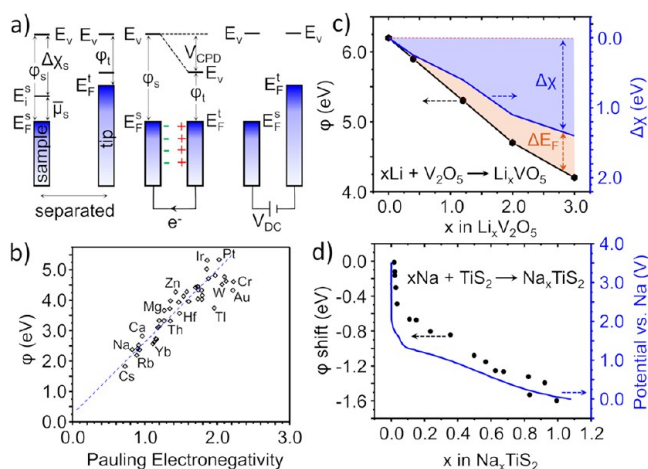


Figure 8. Work function and contact potential difference. a) Principle of KPFM operation: shown are band diagrams of a grounded metallic sample and conductive AFM tip, vacuum levels (E_V), electron chemical potentials ($\bar{\mu}$), surface dipole barrier ($\Delta\chi$), and electrostatic potential energy of electrons (E_s). When tip and sample (that have different work functions, ϕ) are separated, they do not interact (left panel). Once they are brought into close proximity, electrons will flow to equilibrate the Fermi levels (E_F). This process will charge the two objects, shifting the vacuum level and creating a Volta potential (or contact potential) difference, V_{CPD} , between them. Application of an external voltage $V_{DC} = V_{CPD}$ will restore the initial state. b) Work function of elemental metals vs Pauling electronegativity. Reprinted with permission from ref 136. Copyright 1974 American Institute of Physics. (c) Variation of work function, Fermi energy, and surface dipole of V_2O_5 during lithiation. Reprinted with permission from ref 137. Copyright 2006 Elsevier. (d) Work function shift and electrode potential of TiS_2 (vs metallic Na) during sodium intercalation. Reprinted with permission from ref 138. Copyright 2004 The American Chemical Society.

on charge distribution on the atomic level in ionic crystals¹²⁹ and even inside individual organic molecules.¹³⁰ More details about different KPFM modalities, resolution limits, sensitivity, and artifacts can be found elsewhere.^{127,128,131–135}

The material's work function is a measure of its chemical oxidation state, much like the electrode potential. For pure elements, the work function is proportional to their electronegativities (Gordy-Thomas Law, Figure 8b).¹³⁶ Reduction of a solid material decreases its work function, as illustrated by lithiation and sodiation of V_2O_5 ¹³⁷ and TiS_2 ¹³⁸ in Figures 8c and d, respectively (a similar trend also exists for binary oxides¹³⁹). This decrease is due to both lowering the Fermi level of the substance and changes in the surface dipole (Figure 8c). A direct comparison between the TiS_2 electrode potential and work function as sodium intercalates is shown in Figure 8d as an example of a significant similarity between the two observables. Finally, the electrode potential is simply equal to the Volta potential (CPD) between a metal and a reference metallic electrode at the point of zero charge.¹¹⁷ Thus, although liquid-less AFM techniques do not directly measure the sample's electrode potential, they provide an alternative electrochemical descriptor in the form of CPD or a sample's work function.

The application of KPFM and EFM-like techniques to electrochemical studies has been limited, but several interesting studies of Li-ion batteries (LIB) have been reported that endeavor to unravel the battery aging mechanism by not only

looking at the material's morphology-structure-performance relationships but also by detecting functional changes at the nanoscale, such as potential distribution at the interfaces and contact resistance. Zhu *et al.*¹⁴⁰ investigated an all-solid-state thin film LIB consisting of a $LiNi_{1/3}Co_{1/3}Mn_{1/3}O_2$ cathode, lithium phosphorus oxy-nitride (LiPON) electrolyte, and a TiO_2 anode, as shown in Figure 9a. A biased conductive AFM tip acted as an anode current collector when the battery was charged/discharged by scanning an anode area of $1 \times 1 \mu m^2$ in contact mode. The voltage waveform used for writing is shown in Figure 9b, lower graph. Following writing, the tip was lifted to 40 nm above the surface and the poled area was imaged in KPFM mode. The change in the surface CPD can be due to multiple factors, such as electronic charge injection and trapping in the oxide, a shift in the Fermi level, Li^+ ion migration, and surface H^+ and OH^- ion migration, and since the measurements were performed under ambient conditions, the authors compared behavior of the LIB with that of a TiO_2 film. In Figure 9b, the top graph shows that the surface potential shift (relative to the not biased state) of both the LIB and single TiO_2 layer follows the polarity of the applied bias voltage. Moreover, the first poling at positive bias generated equal CPD shifts in both systems. However, subsequent cycling linearly increases the CPD shifts in the single TiO_2 layer with each cycle, whereas the battery anode surface potential is repeatedly alternated between nearly fixed values. This observation can be explained by electronic charge injection/trapping and redistribution/accumulation of the H^+/OH^- screening surface ions in single layer TiO_2 . The same can explain the CPD shift in the LIB during the first positive bias writing. Subsequent biasing of the LIB initiates a reversible lithiation of the anode and cycling between two phases with stable CPD shifts: $TiO_2 + xLi^+ + xe^- \rightleftharpoons Li_xTiO_2$. This is a good example demonstrating various contributions to the CPD. The LIB surface potential hysteresis is stable with small shifts in the negative bias region (Figure 9c), indicative of accumulation of the incompletely delithiated Li_xTiO_2 phase. Note that this phase-coexistence potential stability effectively provides an internal reference electrode for the system. The one-phase TiO_2 sample lacks a stable CPD, since a variable amount of charge can be injected into it. Comparison of the CPD and topographic maps of the LIB recorded after ± 3 V poling shows that the grains are less responsive to biasing than the grain boundaries, which implies an enhanced Li^+ ion transport along the latter.

Using KPFM on conventional LIBs is more challenging due to the presence of conductive and potential-screening liquid. In 2011 Nagpure *et al.*¹⁴¹ used cylindrical LIBs with $LiFePO_4$ cathodes in a post-mortem KPFM study. The batteries were charged, discharged, and then disassembled in air. Small portions of the cathode strip were then cut out and imaged by KPFM in air. It was found that the fresh samples had a larger charge sustaining capacity than the aged ones, but the study did not show any spatial variability in the CPD maps. The Kholkin group employed a similar approach to study graphite anodes:¹⁴² A LIB was discharged, disassembled in a glovebox, and the graphite anodes were washed, embedded in epoxy, polished, and imaged by KPFM in air. Two kinds of batteries were investigated: fresh (discharged at 1C rate) and aged (discharged at 16C). KPFM images and histograms of the graphite anodes of these two samples are shown in Figure 9d,e, respectively. Large graphite grains of the fresh sample have sharply outlined regions of lower potential in their cores, and

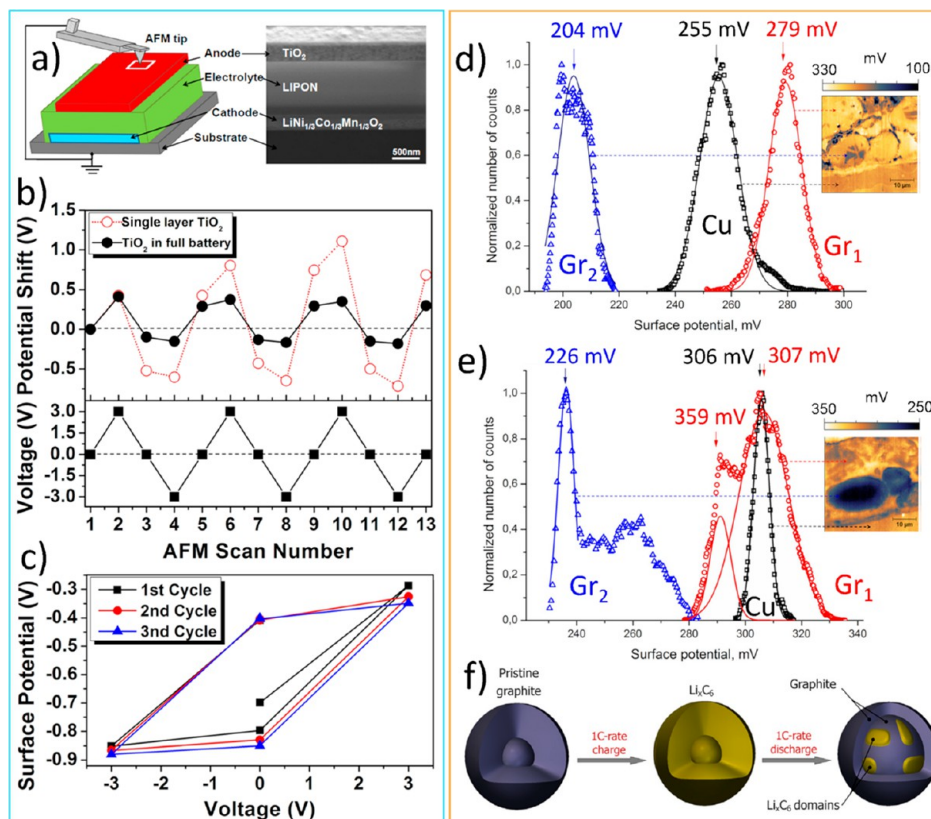


Figure 9. KPFM of battery anode materials. (a) Schematic of experimental setup for cycling an all solid-state LIB and measuring CPD on its TiO₂ anode and SEM image of a cross-section of the battery showing its layered structure. Battery was cycled by applying a voltage bias to the tip (in contact with the anode) relative to the cathode. KPFM performed by lifting the tip and scanning following each charge/discharge step. (b) Average CPD shift of TiO₂ anode (both single layer and full battery) and applied voltage as a function of measurement sequence. (c) CPD evolution during battery cycling vs battery voltage. Reprinted with permission from ref 140. Copyright 2012 American Institute of Physics. (d) Histogram of CPD distribution and KPFM map (inset) of region in a graphite anode of fresh LIB. Arrows indicate areas in image corresponding to that potential. (e) Histogram of CPD distribution in KPFM map (inset) of region in a graphite anode of the aged LIB. (f) Proposed “mosaic” model of graphite particle incomplete delithiation. Adapted with permission from ref 142. Copyright 2014 Elsevier.

the CPD map distribution has three narrow peaks corresponding to the inside of the grains, outer part of the grains, and the copper current collector. The aged sample (Figure 9e), on the contrary, has a narrow copper peak and two very broad overlapping graphite peaks corresponding to an almost linear potential drop from the periphery to the core of a large grain seen in the image. Luchkin *et al.*¹⁴² conclude that the observed intragranular potential variations are due to the presence of a Li⁺ gradient (via an oxide/hydroxide/carbonate film on the surface of the graphite formed after exposure of the samples to air). Thus, the lowest CPD in the maps correspond to the highest lithium content and large grains of the aged sample did not delithiate properly upon fast-rate discharging. They point out that this incomplete delithiation correlates well with the loss of specific capacity observed previously in the LIBs cycled at a high rate. The reason for Li⁺ trapping in the grains was explained with mosaic and radial models. At low discharge rates, Li is trapped in the core of graphite grains in separate islands, whose boundaries are pinned by localized crystallographic defects (Figure 9f) forming a mosaic-like Li distribution (Figure 9d). High discharge rates limit the time of Li⁺ migration and the grain cores remain uniformly lithiated. Obviously, the first mechanism is size independent, while the second depends on the grain size. The authors conclude that with a proper calibration, KPFM can be used to provide

quantitative information about the Li distribution in the battery materials and help understand the aging mechanisms of LIBs.

An *in situ*, rather than post-mortem, KPFM study of a working LIB was reported by Masuda *et al.*¹⁴³ The all-solid-state battery had a compound cathode including LiCoPO₄, binder, and Pd as current collector. The KPFM measurements were performed in a cross-sectional mode in a dry nitrogen atmosphere (Figure 10a). The researchers focused on the cathode–electrode interface in two states of charge: charged and discharged battery, as indicated by the blue circles in (Figure 10b) master curve. The topography of the selected region (Figure 10c) was rather smooth and featured several voids. The same area was mapped with energy dispersive spectrometry (EDS) in scanning electron microscopy (SEM), providing information on the distribution of the active cathode material and Pd particles (Figure 10d). This map was used as a mask to highlight regions of different composition in a KPFM image of the same region in the uncharged state (Figure 10e). The Pd grains have a much lower CPD (higher work function) than the cathode and electrolyte grains (containing Co and Ti, respectively). The situation changes once the battery is charged (Figure 10f): The Pd electrode on the right and electronically conductive Pd grains display a high CPD, while the LiCoPO₄ material has a lower potential. The right side of

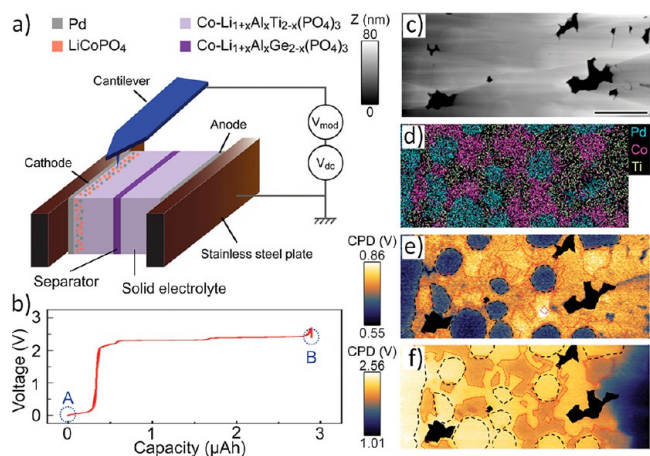


Figure 10. *In situ* KPFM of a cathode material in a working battery. (a) Schematic of *in situ* KPFM scanning of a LIB cross-section in the cathode region. (b) Charging curve of battery with states A and B selected for KPFM probing. (c) Topographic map of cathodic region, (d) corresponding EDS map showing distribution of materials components, (e) CPD map of same region in initial A state with grain boundaries defined by EDS mapping, (f) CPD map of same region in charged state B with overlapping composition mask. Adapted with permission from ref 143. Copyright 2017 Royal Society of Chemistry.

Figure 10f displays the boundary between the cathode region and electrolyte, where a 0.8–1 V potential drop occurs. Note that unlike the case of an uncharged battery, the CPD map is a convolution of the electrostatic potential and change in the work function of the material due to delithiation. The internal resistance of the battery that controls its performance is determined by the sum of electrostatic potential drops across each of the interfaces between the materials comprising the battery. While most of the recent progress in solid-state LIBs has been dedicated to finding electrolytes with the highest ionic conductivity,¹⁴⁴ the requirement for large energy density implies a very thin electrolyte layer (<10 μm), which, even for already known solid-state electrolytes, will have a large enough conductivity so as not to be a limiting factor in the battery performance. Instead, the battery's charging rate will be limited by the interfacial impedances.¹⁴⁴ KPFM is one of the very few techniques that is able to directly probe the potential drop across different interfaces in a working LIB.

Another important electrochemical device besides batteries is the solid oxide fuel cell (SOFC). Since its operation requires elevated temperatures to increase the oxygen-ion conductivity of the constituting electrolyte, studying SOFCs *in operando* by SPM is extremely challenging. Recently, Nonnenmann *et al.*¹⁴⁵ developed the high-temperature environmental chamber schematically shown in Figure 11a. The gas-fed chamber houses the sample that can be heated up to 700 °C in a controlled atmosphere. Imaging is performed through a small opening in the lid of the chamber, thus protecting the sensitive AFM electronics from the high temperature of the sample inside. Nonnenmann *et al.* used this approach to image a working solid oxide fuel cell at 600 °C with scanning surface potential microscopy technique^{146,147}—a method similar to KPFM. A schematic depiction of the fuel cell structure and associated potential distribution is shown in Figure 11b. Similar to the battery case, in which the electrostatic potential distribution between the electrodes is determined by the chemical potential of electrons and Li⁺ ions in each material,

here, the chemical potentials of the H⁺ and O²⁻ ions as well as electrons dictate the electrostatic profile between the electrodes. Figure 11d–l shows topographic and CPD maps and CPD profiles in the cathode, solid electrolyte, and anode of the SOFC.^{145,148,149} These data allowed the estimation of the ion transport activation barrier for the SOFC materials. Other systems have also been explored.^{150,151}

One of the most important challenges in studying charge transport in electrochemical systems is the need to separate the electronic current from the ionic one with high spatial resolution. While the common amperometric techniques such as electrochemical impedance spectroscopy (EIS) suffer from low spatial resolution, KPFM and EFM, having high-resolution, are sensitive to both electronic and ionic processes and only detect the overall charge distribution. Overcoming this challenge is possible by looking at the time domain, since the mobilities and transport coefficients of electronic and ionic charge carriers are vastly different in most materials. Recording the potential evolution over time can help separate the electronic and ionic responses to an electrical stimulus, as shown in Figure 12a. This idea was realized by modifying the scanning surface potential microscopy technique into the time-resolved KPFM (tr-KPFM),^{152,153} which features the high spatial resolution of KPFM and a 20 ms temporal resolution allowing the probing of the bulk and surface charge dynamics. Tr-KPFM has been used in devices with lateral electrodes, which are biased with a voltage step pulse (Figure 12a), triggering charge migration that is detected by the AFM tip. The resulting 3D tr-KPFM data set (potential = $f(x,y,t)$, Figure 12b) is hard to visualize, and the data are typically averaged over the spatial dimension that runs parallel to the electrodes. Figure 12b schematically shows a sample with two lateral electrodes and distribution of surface OH⁻ groups during the bias-on (polarization (P)) and bias-off (relaxation (R)) steps of the experiment. The surface ionic transport, known since Shockley's time,¹⁵⁴ is important for many devices, determining the operation of conductometric gas sensors,¹⁵⁵ electrocatalysts, and affecting the polarization switching in ferroelectric memory devices.¹⁵⁶ Unlike amperometric techniques that are limited by the sensitivity of the current amplifier, tr-KPFM can probe minuscule charge flows, even on insulating surfaces.

Figure 12c–f presents examples of tr-KPFM potential profiling for various materials: activated Ca-substituted BiFeO₃ (Ca-BFO),¹⁵² a LiNbO₃ crystal,¹⁵³ a nanostructured ceria film,¹⁵⁷ and pristine Ca-BFO. The dark blue to green curves denote the systems' responses during the bias-on step and the green to red curves display CPD profiles when the bias was off. The measured surface potential evolution in these materials varies significantly, indicating the difference in the stimulated surface processes and their mechanisms. The pristine Ca-BFO has an almost linear initial potential distribution between the electrodes (Figure 12c, dark blue line) when a 5 V lateral bias is applied to the device. Ten seconds into the bias-on state, the potential profile curves down near the biased electrode (Figure 12c, upper green line), revealing polarization of the film due to accumulation of negative charge in that region. Once the lateral bias is turned off, the surface CPD becomes negative throughout the film (Figure 12c, lower green line), confirming the presence of negative charge. This charge dissipates as the material relaxes over the next 10 s, and the potential profile becomes a flat zero line (Figure 12c, dark red line).

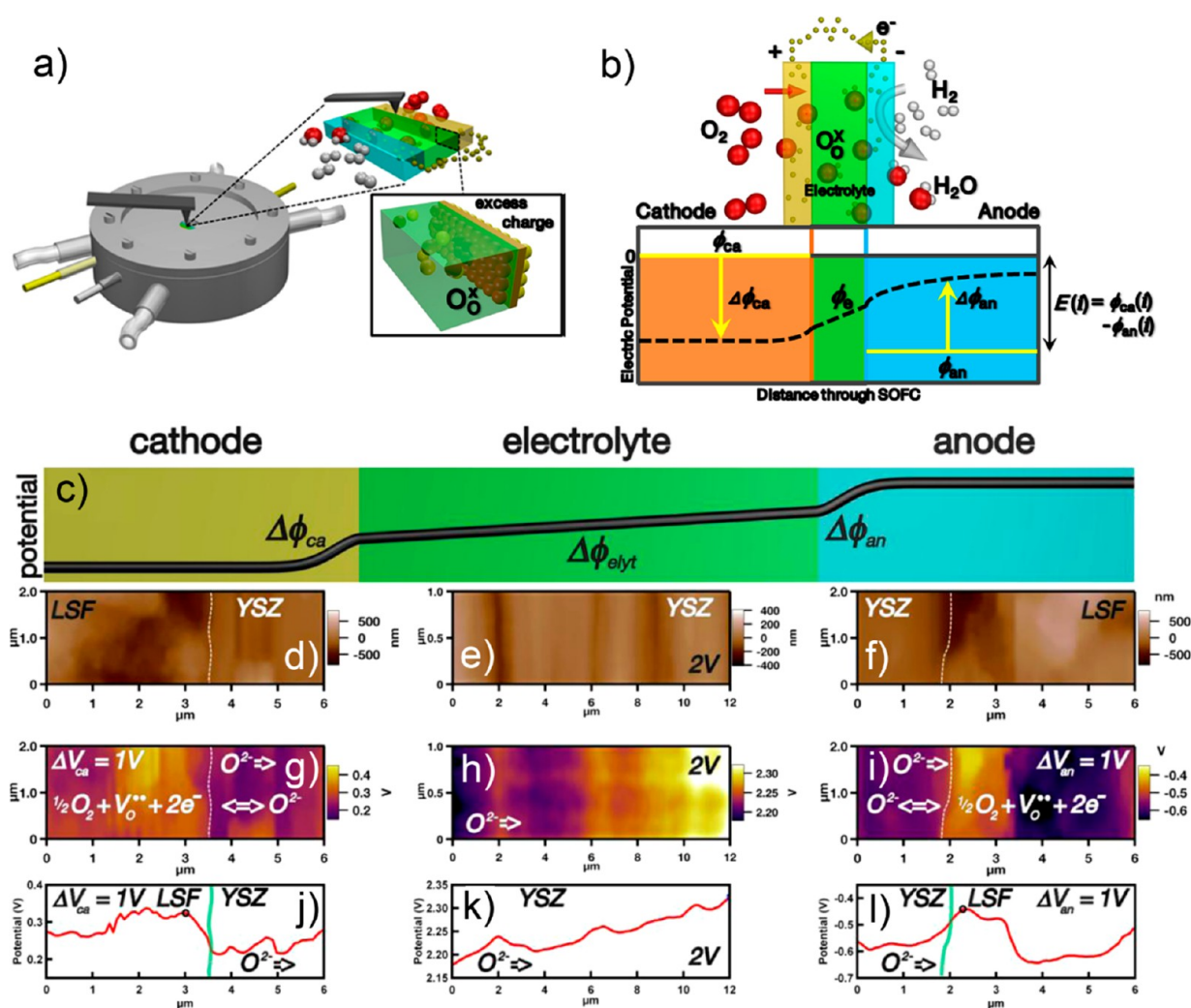


Figure 11. *In situ* hot state KPFM of a working fuel cell. (a) Schematic of environmental hot stage for high-temperature SPM imaging. (b) Operating SOFC schematic with cathodic and anodic reactions and potential distribution between electrodes. (c) Electrostatic potential profile in an ideal SOFC. (d–f) KPFM topographic images, (g–i) CPD maps, and (j–l) CPD profiles in a biased symmetrical LSF-YSZ SOFC at 600 °C (vertical lines represent interfaces). Adapted with permission from ref 145. Copyright 2013 American Institute of Physics.

A strikingly different behavior is manifested by the activated Ca-BFO film, in which positively charged oxygen vacancies have been racked-up by the grounded electrode. Other regions of the film become depleted of oxygen vacancies and acquire an almost metallic electronic conductivity (p-doped semiconductor). The flat CPD region between 45 and 100 μm in Figure 12d is this virtual metallic electrode. All potential drops near the left electrode, where oxygen vacancies have accumulated (Figure 12d, dark blue to green lines). Later, during the bias-off stage, vacancies slowly dissipate, reducing the size of the positive CPD hump (Figure 12d, green to dark red curves). Unlike the semiconducting Ca-BFO, the ferroelectric LiNbO₃ crystal requires a lateral bias of 90 V to become activated, but even at such a high voltage, this material only shows a transient positive charge injection from the biased electrode (Figure 12e, blue curves on the right side). This phenomenon is limited to a narrow region, while the rest of the material is unaffected during both bias-on and -off stages. The ionically conductive nanostructured ceria shows a similar charge injection, which initially accumulates in the material, slowly migrates to the grounded electrode during the bias-on period (Figure 12f, dark blue to green curves) and dissipates

once the electrodes are grounded (Figure 12f, green to red curves).

The presented data are illustrative of the ability of tr-KPFM to probe various charge redistribution processes in materials with a range of conductivities. Since standard KPFM features a time resolution of tens of seconds to tens of minutes, only the last charge state of the material is recorded when the relaxation process is over (*i.e.*, the red line in Figures 12c–f). The observed CPD evolution can be determined by either electronic or ionic charge carriers, whose response times are set by the RC constant of the circuit and the local ionic mobility, respectively. In the case of nanostructured ceria, the RC constant was *ca.* 100 s, which is much larger than the 10 s time frame used for the tr-KPFM measurements. Thus, the electronic response could not have been captured in this case. On the contrary, about 60% of the activated Ca-BFO film had an electronic conductivity of 0.2 S/m or higher and a low oxygen vacancy mobility. The estimated electron response time in this case is lower than 1 μs and thus, no relaxation was observed in the metallic region during the bias-off stage (Figure 12d, red line between 45 and 100 μm). The experimentally observed response times can be extracted

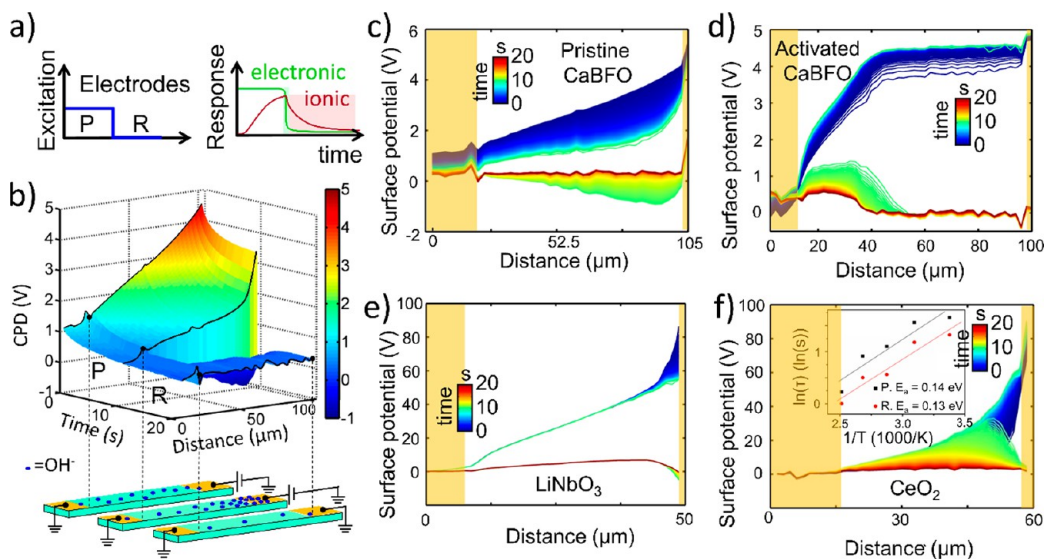


Figure 12. Time-resolved KPFM: the principle and examples. (a) In tr-KPFM a voltage excitation in the form of a step pulse is applied between lateral electrodes of a sample, to which the system responds by redistributing ionic and electronic charge species. CPD is recorded during bias-on (polarization (P)) and bias-off (relaxation (R)) time periods. Separation of electronic and ionic responses is possible due to difference in response times. (b) 3D tr-KPFM data set recorded on Ca-BFO: The four variable (V_{CPD}, x, y, t) data set is averaged over the spatial dimension that runs parallel to the electrodes to generate a 3D plot CPD as a function of interelectrode distance and time. Polarization of surface ions (presumably OH^- groups) observed in CPD profiles and shown schematically below plot. (c–f) Multiple CPD profiles measured at different times between the electrodes (yellow strips on left) for various samples: mixed ionic–electronic conductor (Ca-BFO), ferroelectric (LiNbO_3), and oxygen-ion conductor (CeO_2) of different electrochemical processes probed by tr-KPFM. Inset in (f) shows Arrhenius plot for mean lifetime of charged species of Ca-BFO surface during polarization (P) and relaxation (R). (a–d) Adapted with permission from ref 152. Copyright 2013 The American Chemical Society. (e) Adapted with permission from ref 153. Copyright 2014 Wiley-VCH. (f) Adapted with permission from ref 157. Copyright 2015 The American Chemical Society.

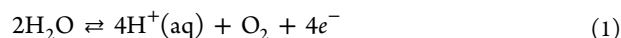
from the potential *vs* time curves fitted to a single exponential decay: $\text{potential}(t) = A + B \times e^{-t/\tau}$. Here *A* and *B* are constants and τ is the mean lifetime of the charged species that causes the potential variation.

For pristine Ca-BFO, the mean lifetime is plotted in an Arrhenius plot shown as inset of Figure 12f. The activation energies for the bias-on and bias-off states are 0.14 and 0.13 eV, respectively. Additionally, the diffusion coefficient of charged species can be estimated as $D \approx d^2/\tau$, where *d* is the interelectrode distance. The calculated room temperature diffusivity ($2 \times 10^{-9} \text{ m}^2/\text{s}$) and activation energy are similar to those for proton transport in bulk water ($D \approx 10^{-8} \text{ m}^2/\text{s}$, $E_a = 0.12 \text{ eV}$).¹⁵² By taking into account that the surface potential evolution was strongly affected by ambient gas humidity in these samples, the observed behaviors can be best explained by generation and migration of the adsorbed protons on the surface of the LiNbO_3 , ceria and pristine Ca-BFO samples. The response of the activated Ca-BFO film may have also been influenced by bulk oxygen vacancies and electronic hole transport.

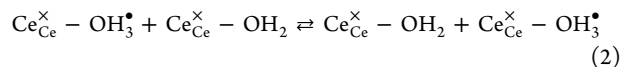
All the case studies discussed lack an important element of quantitative data analysis and interpretation. Although several potential-detecting SPM techniques have been developed and applied to a range of materials and electrochemical devices in the last three decades, the obtained data underwent only minimal analysis, with a typical study presenting CPD maps and deriving qualitative conclusions. A full quantitative analysis approach would require solving the inverse problem by converting the CPD maps into maps of local charge distributions, rates of electrochemical reactions, or ionic mobilities. This challenging problem was partially solved (in one dimension) in early KPFM studies of semiconducting

devices^{158–160} and multielectrode gas sensor systems,¹⁵⁵ and has become an integral part of the so-called energy discovery platform (EDP) approach.^{157,161,162}

The EDP approach seeks to unravel the surface electrochemistry and ionic transport in the studied system through a synergistic combination of sample microfabrication, tr-KPFM, and numerical modeling. Considering the case of nanostructured ceria, it was established that protons were injected from the positively biased electrode. These protons were generated at the triple-phase boundaries (platinum electrode, air, and ceria) through the water splitting reaction:



Injected protons electromigrate *via* the Grotthuss mechanism and diffuse in the adsorbed water layers along the oxide surface:¹⁶¹



The measured surface potential is determined by both diffusion/migration and by generation/annihilation of protons. To deconvolute the coupling between the transport, reaction, and electrostatics contribution to the CPD, the following equations need to be solved:

$$\frac{\partial n_i}{\partial t} = \nabla \times (-D_i \nabla n_i + z_i \mu_i n_i F \nabla \Phi) + (S_i - f_i n_i) \quad (3)$$

$$\nabla^2 \Phi = -\frac{\sum n_i z_i q_0 F}{\epsilon_0 \epsilon_r} \quad (4)$$

where n_i is the local time-dependent concentration of ions ($i = \text{H}^+, \text{OH}^-$), *D* is the ionic diffusivity, *z* is the ion charge, μ is

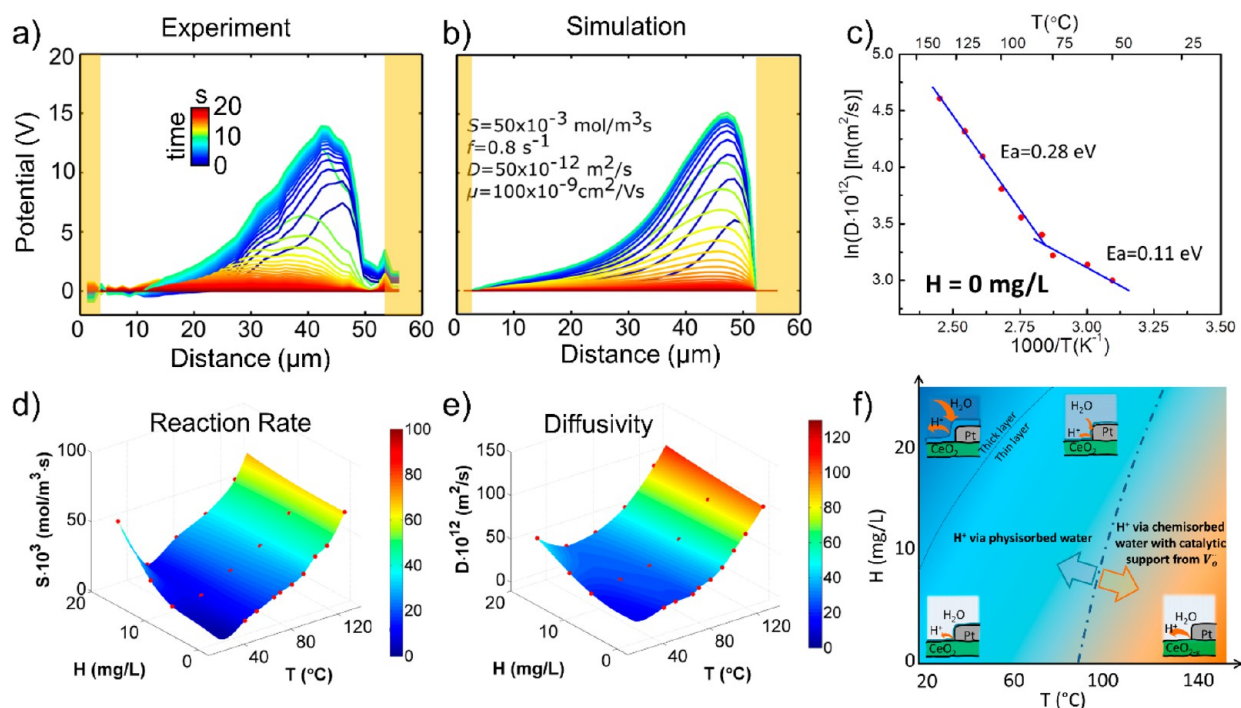


Figure 13. Tr-KPFM and the energy discovery platform method. (a–c) Tr-KPFM measured and COMSOL-simulated surface potential profiles on nanostructured ceria (golden stripes represent lateral electrodes) at 135 °C and 0% relative humidity. For experimental data, potential profiles at end of bias-on and -off periods were subtracted from profile curves at other moments of time. (c) Arrhenius plot of surface proton diffusivity extracted from fits shows crossover at *ca.* 100 °C. (d, e) Dependence of deconvoluted reaction rate and proton diffusivity on air humidity (*H*) and temperature. (f) Schematic phase diagram of different proton conduction regimes in nanostructured ceria, as extracted from the tr-KPFM data. Adapted with permission from ref 161. Copyright 2016 IOP Publishing.

mobility in the electric field, F is the Faraday constant, Φ is the surface potential, S is the rate of generation reaction (for protons rate of eq 1), f is the rate of annihilation reaction (inverse of eq 1), q_0 is the elementary charge, and $\epsilon_0\epsilon_r$ is the ceria permittivity. The rates of proton generation and annihilation are given by eq 1 as

$$S_{\text{H}^+} = \frac{d[\text{H}^+]}{dt} = 2k \times [\text{H}_2\text{O}];$$

$$f_{\text{H}^+} n_{\text{H}^+} = -\frac{d[\text{H}^+]}{dt} = 2k' \times [\text{H}^+]^2 \times p_{\text{O}_2}^{1/2} \quad (5)$$

By solving this set of equations with finite element modeling and appropriate boundary conditions, one can simulate potential profiles between the electrodes as a function of time, which can then be matched to the experimental data by tuning the four parameters that characterize the observed processes: D , μ , S , and f . Figure 13a–b presents the experimental and simulated potential profiles for nanostructured ceria. The extracted system-governing parameters in the form of their dependence on temperature and air humidity are plotted in the phase diagrams shown in Figure 12d–e. The shapes of the 3D surfaces of these plots show some differences, implying different contributions of the reaction rate and proton diffusivity to the tr-KPFM signal.

An Arrhenius plot of the extracted proton diffusivity under dry conditions (Figure 13c) shows a crossover between two transport regimes, with the activation energy changing from 0.11 to 0.28 eV. The crossover temperature is around 100 °C, indicative of physisorbed water desorption, which hampers transport. The reaction rate Arrhenius plot yields only one activation energy, 0.24 eV, a value that is significantly lower

than the activation barrier for the water splitting reaction (equation (1) $E_a^{\text{WSR}} \approx 1.2$ eV). This discrepancy can be explained by recalling that the reaction rate is proportional to both the reaction constant and water concentration, which have opposite temperature dependencies:

$$S_{\text{H}^+} = 2k \times [\text{H}_2\text{O}] = K \times e^{-E_a^{\text{WSR}}/k_B T} \times e^{H/RT} \quad (6)$$

where K is a temperature-independent constant, k_B is the Boltzmann constant, T is the absolute temperature, R is the universal gas constant, and ΔH is the average adsorption enthalpy over the probed temperature range. It follows that the measured activation energy for S is $E_a^{\text{meas}} = E_a^{\text{WSR}} - \frac{\Delta H k_B}{R}$. Hence, the value of $\Delta H = 92$ kJ/mol falls in the range between the adsorption enthalpies of the physi- and chemisorbed species existing in the probed temperature range. As a summary of these findings,¹⁶¹ the proton generation and transport regimes are presented in Figure 13f and reveal how an interplay between the temperature and humidity thermodynamic factors favor the existence of several surface conditions. A thick physisorbed layer of surface water existing on the surface at low temperature and high humidity facilitates proton transport. As the temperature increases and humidity decreases, only a thin physisorbed water layer remains, impeding transport and giving rise to a minimum in the phase diagram of Figure 13d,e. Finally, only chemisorbed water is left on the surface at high temperatures and low humidity. In this regime, proton transport is enhanced by the catalytic influence of oxygen vacancies and high thermal driving force.

Although the EDP approach has proven to be a powerful tool for unraveling reaction and charge transport details, interpretation and deconvolution of the tr-KPFM data may

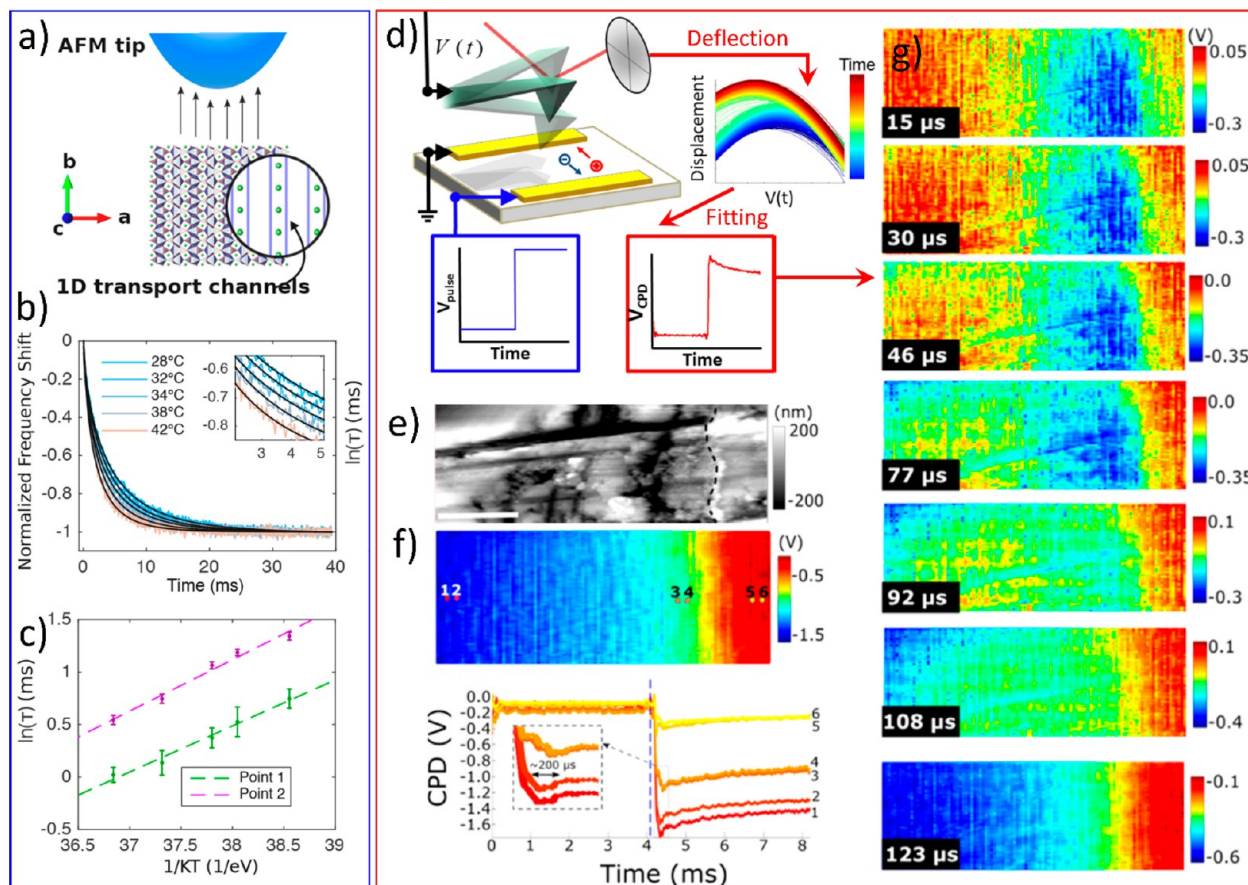


Figure 14. Ionic dynamics captured by other time-resolved approaches. (a) Schematic of electrostatic force spectroscopy measurement on LiFePO_4 . Application of stepped voltage bias to tip activates ionic motion beneath it, which can be registered by monitoring frequency shift of cantilever oscillation. (b) Frequency shift *vs* time plots for different temperatures. (c) Arrhenius plot of relaxation times for two different locations on sample. Adapted with permission from ref 164. Copyright 2017 The American Chemical Society. (d) Schematics of ultrafast F^3R -KPFM imaging approach: While a DC step-pulse is applied between the lateral electrodes on sample activating ion transport, an AC single-frequency bias is applied to AFM tip oscillating above surface, and signal from the photodetector is captured, filtered of noise, and fit to obtain CPD. (e) Topographic image of a $\text{CH}_3\text{NH}_3\text{PbBr}_3$ single crystal with metallic electrode on left (behind dashed line). (f) Time-averaged (over *ca.* 4 ms) CPD map and CPD temporal profiles at selected points on sample. (g) CPD maps at various times after electrode was negatively biased showing field-assisted dynamics of positively charged ions. Adapted with permission from ref 166. Copyright 2017 The American Chemical Society.

become ambiguous or impossible for some complex systems that feature concurrent processes with similar time constants (*e.g.*, double-layer charging or discharging *vs* bulk diffusion). Similar challenges are known for interpretation of impedance spectroscopy data and can be addressed by employing more complex complementary methods.

Triggering ionic motion does not necessarily require a lateral electrode excitation. Rather, a step-like voltage pulse can be applied to the AFM tip itself when it is positioned a short distance (10–15 nm) above the surface of an ion conductor (Figure 14a). Ions underneath the tip are set in motion by its electrostatic field and screen it, affecting the force (and, hence, the resonant frequency) on the cantilever. This approach was implemented in 2004 in time-domain electrostatic force spectroscopy (td-EFS).¹⁶³ A set of frequency *vs* time curves are shown in Figure 14b for a LiFePO_4 crystal. These curves can be fitted to a stretched exponential:

$$\Delta f = (\Delta f_{\text{sat}} - \Delta f_{\text{fast}}) \Delta \left\{ 1 - \exp \left[- \left(\frac{t}{\tau} \right)^\beta \right] \right\} + \Delta f_{\text{fast}}, \quad \text{where}$$

Δf_{fast} is the frequency shift due to fast relaxation (initial sharp drop of frequency), Δf_{sat} is the saturation value, t is time,

β is the stretch factor, and τ is the relaxation time dependent on the local resistivity, R , and capacity, C , of the probed nanoscale volume (*ca.* 40 nm³) and the capacitance, C_V , of the tip–sample gap: $\tau = R \times (C + C_V)$. It has been shown that Arrhenius plots of relaxation times measured microscopically with td-EFS and macroscopic electrical spectroscopy for two different solid-state ion conductors are similar.¹⁶³

An Arrhenius plot for two locations on a LiFePO_4 sample is shown in Figure 14c.¹⁶⁴ The activation energy calculated from the plots is not the energy barrier for a single ion hopping event (E_a), but rather an activation energy for the collective ionic transport through the material: $E_a^* = E_a/\beta$.¹⁶⁴ Knowing the β value, E_a can be recovered from the data. In addition to simply activating ionic transport below the tip, charge can be implanted by bringing the tip into contact with the surface then pulling it away and monitoring the charge dissipation by subsequent KPFM imaging. The created charge gradients can be used to locally change the surface oxidation state and study the interaction of ionic vacancies with surface defects. It has been reported¹⁶⁵ that for samples in high vacuum, charge can be easily implanted in oxygen ion conductors such as yttria-stabilized zirconia and gadolinia-doped ceria, but the surface of

the electronic insulator Si_3N_4 remains unaffected by implantation attempts. These observations confirm that the implanted charge is of an ionic nature, that is, oxygen vacancies. The negative voltage implantation is given by $V_{\text{O}}^{\times} + 2e^{-} \rightarrow V_{\text{O}}^{\bullet\bullet}$, while at the positive polarity, oxygen is evolving: $\text{O}_{\text{O}}^{\times} \rightleftharpoons V_{\text{O}}^{\bullet\bullet} + \frac{1}{2}\text{O}_2 \uparrow + 2e^{-}$. The 2D Poisson and Fick's second law equations can link the KPFM maps with the Gaussian distribution of the implanted charge to the local charge density and ionic diffusivity, as in the 1D case of EDP.

In depth understanding of the nanoscale reactions and charge transport is impossible without detecting all the active processes in the system and capturing the potential dynamics across a wide frequency range. The time resolution of the SPM techniques described above ranged from milliseconds to minutes, whereas the electronic response times in semiconductors and mixed ionic-electronic conductors (MIEC) are on the order of microseconds and below. Expansion into this time domain was recently accomplished by development of the fast free force recovery KPFM ($\text{F}^3\text{R-KPFM}$) method.¹⁶⁶ Similar to tr-KPFM, an excitation DC step-pulse is applied between the lateral electrodes and the tip is AC-biased; however, rather than a single-frequency lock-in detection of the cantilever response in a slow pixel-by-pixel fashion, the entire output of the photodetector is captured in full information capture (G-mode)^{167,168} (at a sampling rate of 1 to 10 MHz), digitally filtered of noise, and fit to extract the CPD dependence as a function of time (Figure 14d). Typically, the time resolution of AFM is fundamentally limited to milliseconds by the cantilever ring-down effect, the time it takes for the cantilever to equilibrate after a sudden perturbation. However, this mechanical bandwidth can be overcome if the cantilever transfer function, $H(\omega)$, is known from a prior calibration. The time-dependent force on the cantilever in the Fourier space can then be calculated as $F(\omega) = Y(\omega)/H(\omega)$, where $Y(\omega)$ is the cantilever displacement (photodetector response).¹⁶⁶ Since the low-pass filter of the lock-in amplifier is eliminated, $\text{F}^3\text{R-KPFM}$ becomes ultrafast and is capable of scanning the sample at normal AFM speeds and having a 10 μs resolution.

As an example, organometallic halide perovskites (OMHPs) possess the unique properties of a mixed conductor with ambipolar ionic-electronic transport characteristics. Recently, OMHPs have demonstrated outstanding multifunctionality in photovoltaics,¹⁶⁹ photodetectors,¹⁷⁰ light-emitting diodes,¹⁷¹ and ionizing radiation sensors¹⁷² and are therefore at the forefront of research activities. Although research on OMHP has made remarkable achievements during the past few years, OMHPs have shown spatial and temporal inhomogeneities in charge transport properties due to anisotropic ion migration and charge distribution. Therefore, it is important to understand the origins of time-dependent phenomena and the spatial localization of processes activated by an external stimulus such as light or an electric field. Figure 14e–g presents mapping results of field-assisted charge transport in an OMHP device, for example, a $\text{CH}_3\text{NH}_3\text{PbBr}_3$ single crystal, in which several different ions are mobile. Topographic and KPFM images averaged over 4 ms of the device are shown in Figure 14e,f, respectively. The metallic electrode is visible on the right side of the images. Selected CPD vs time response curves for several locations are shown in Figure 14f. As can be seen, potential is almost unperturbed on the grounded electrode (as the opposite electrode is biased at -4 V), but

a significant transient is observed on the crystal itself. Time-sliced maps of the region are presented in Figure 14g illustrating the spatial variation of the surface potential evolution due to ion migration.

Here, it was demonstrated that advanced KPFM on lateral devices can be used for visualizing ionic and electronic charge dynamics and electrochemical reactivity across four decades, from 10^{-2} to 10^5 Hz, thereby separating underlying processes based on their response time (tens of μs to several minutes). The potential-detecting SPM techniques provide ample opportunity to study nanoscale electrochemical reactions and ionic/electronic transport, including ion interactions with the local defect structure and interfaces, spatially resolved energy barriers for single-ion hopping and collective ion migration, and temperature and gas environment dependence of reaction rates and regimes. Despite significant challenges arising from the complexities of the studied processes, we expect that the future will see an expansion in the application of these methods to electrochemical systems in a systematic and quantitative way.

Current Detection in Liquids. Classical electrochemical techniques have been developed to study systems containing liquid electrolytes, and, like the SPM electrochemical methods, rely on detection of potential, current and sample expansion. Direct downscaling of electrochemical amperometric measurements to the nanolevel is possible, if a liquid electrolyte is present. Liquid acts as a medium that connects nanoscale reactions under the tip to the reference and counter electrodes hundreds of microns away from the tip by shuttling ionic species. Since 1989, several amperometric in-liquid SPM techniques have been developed, all based on ultramicroelectrodes (UME) connected to a potentiostat and scanned across the sample. UMEs are fabricated from fused glass microcapillaries and can be open at both ends (for ion-selective electrodes) or sealed with a Pt wire. The three most common techniques using UMEs are scanning ion conductance microscopy (SICM),¹⁷³ scanning electrochemical microscopy (SECM),¹¹⁸ and scanning electrochemical cell microscopy (SECCM).¹⁷⁴ In SICM, a potential is applied between the wire inside a hollow electrolyte-filled UME and an external electrode, and ionic current through the UME capillary opening is monitored (Figure 15a). When the UME is far from the surface, this current depends only on the potential, bulk ion concentration of the supporting electrolyte, ion diffusivity and diameter of the opening. When the UME is brought within one tip diameter of the surface of the submerged sample, the gap resistance and local sample conductivity start influencing the detected current, which can be used to measure sample's topography and conductivity. Similarly, in SECM, a sealed UME (Pt wire sheathed with glass and exposed to solution only at the very tip) is used to monitor Faradaic charge transfer current between the tip and the sample (Figure 15b). SECM uses several auxiliary electrodes, including a standard reference electrode, to precisely control the potential applied to UME. Finally, SECCM employs a single or double-barrel (θ -type) micropipette with two metallic wires inside and filled with electrolyte to wet the sample's surface locally *via* the formed meniscus (Figure 15c). Thus, the affected region of the sample and the detected current are localized and not affected by the bulk solution noise. The potential can be applied either between the wires or between one of the wires and the sample.

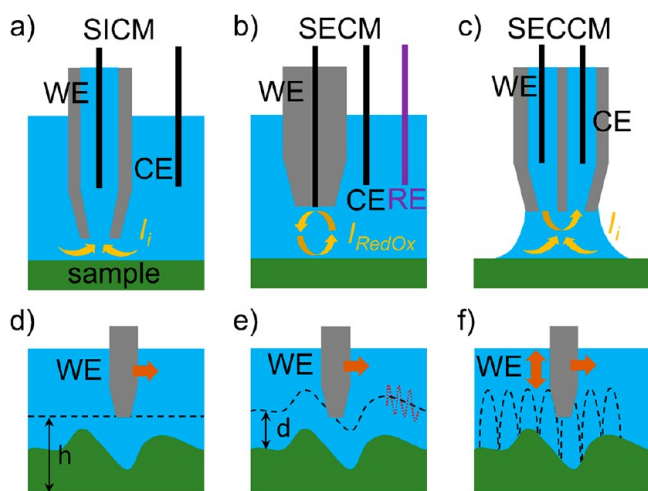


Figure 15. Current-detecting SPM techniques for probing in-liquid electrochemistry. Schematics of (a) SICM, (b) SECM, and (c) SECCM. Modes of operation: (d) constant height, (e) constant distance DC/AC mode, and (f) hopping mode. WE is working electrode, CE is counter electrode, and RE is reference electrode. Dashed lines show the trajectory of the probe, and orange arrows indicate the direction of probe's motion.

All of these techniques can be used in three main modes shown in Figure 15d–f (the names of the modes can differ depending on the technique, for example, SECM AC mode is called scanning vibrating electrode technique). In constant height mode (Figure 15d), the tip approaches the surface until the measured current reaches the set point, and then the surface is scanned while maintaining this set point. This is the most common mode used for SICM and SECM, producing images that are a convolution of the sample's topography and electrochemical activity (conductivity). In constant distance mode, topography is measured separately, and then the tip is kept a constant distance d above the surface, thus only detecting local activity (Figure 15e). This mode can be used in DC or AC variations, when the d -distance is either constant or fluctuates around a constant value by shaking the probe. The AC mode is used with a lock-in amplifier and allows for more precise control of the d -distance. The sample's topography can be measured with SECM/SICM by applying a very small potential to the UME, ensuring that only ionic current flows, and the redox reaction of interest is not initiated. Alternatively, the UME can be a part of the AFM probe, which can measure topography directly.¹⁷⁵ The hopping mode (especially useful for SECCM) can also be used, when the probe reapproaches the surface at each pixel of the forming image, preventing accidental damage of the UME by collision with the surface (Figure 15f).

The resolution of UME-based techniques is lower than that of other SPM methods and is determined by the diameter of the nanopipette opening, or Pt wire electrode. For two decades, spatial resolution of these methods was mainly limited to micrometer or larger scale, but this has been significantly improved in the recent years. Nowadays, typical SICM/SECM probes have opening/tip diameter of 50 to 100 nm, although state-of-the-art probes have been reported with diameters down to 13 nm.¹⁷⁶ The standard vertical resolution of these techniques is about 10 nm.¹⁷⁶

SECM probes are available only from one vendor, and many groups fabricate probes themselves by fusing glass micro-

pipettes, pulling them to nanosizes and then polishing the tip with a focused ion beam. UMEs are hard to work with, as they easily get clogged or blocked by debris, and are sensitive to electrostatic discharge and mechanical vibrations.¹⁷⁷ In addition, nanoelectrodes only produce very small, pA currents. Despite these difficulties, UMEs allow for studying ultrafast reactions and unstable transient species. The gap between the UME and sample is so small that the intermediates can traverse it in a very short time—milliseconds to microseconds—before they disintegrate. For this reason, a lot of work has been dedicated not to spatial surface mapping, as with other SPM techniques, but rather to acquisition of local cyclic voltammogram and approach curves. This way quantitative information about the rate of specific reactions, diffusivity of species, and charge transfer kinetics was obtained. Other advantages of the UME-based techniques include the following: true noncontact mode, allowing for working with very soft samples, such as biological objects; the possibility of probing electrochemistry at the liquid–solid and liquid–liquid interfaces; potential quantitiveness of measurements relying on the presence of reference and auxiliary electrodes and precise current control.

UME-based SPM techniques have been used to image K^+ channels in living kidney cells;¹⁷⁸ probe Li^+ transport in LCO,¹⁷⁹ MnO ,¹⁸⁰ and Si;¹⁸¹ measure electronic conductivity in TiO_2 ;¹⁸² study SEI formation on glassy carbon,¹⁸³ TiO_2 ,¹⁸² and metallic Li;¹⁸⁴ quantify electrochemical activity on $LiFePO_4$ ¹⁸⁵ and $Li_7La_3Zr_2O_{12}$ ¹⁸⁶ surfaces and on Pt,¹⁸⁷ Au,¹⁸⁸ and MoS_2 ¹⁸⁹ nanostructures; detect short-life intermediates such as N,N -dimethylaniline cation radicals,¹⁹⁰ trivalent tin,¹⁹¹ $CO_2^{\bullet-}$,¹⁹² and $O_2^{\bullet-}$.¹⁹³ Below, we present several examples of nanoscale mapping of electrochemical activity in liquids with these techniques (Figure 16).

Unwin's group used SICM to characterize electrocatalytic reactions on individual gold nanoparticles (AuNP) on carbon nanofibers.¹⁸⁸ Employing self-referencing hopping mode and an UME with a tip diameter of about 30 nm, they simultaneously recorded the sample's topography and electrochemical reactivity of borohydride oxidation in alkali aqueous solution. A small voltage, which provided an ionic current feedback, but did not induce BH_4^- oxidation, was used to measure the sample's topography and position the tip 20 nm above the surface at each pixel. Then a larger voltage was applied to measure the local electrocatalytic activity. Figure 16a,b shows SEM and SICM topographic images of a collection of AuNPs. The corresponding normalized current map is shown in Figure 16c. As the nanoparticles catalyze BH_4^- oxidation, the electrolyte around them becomes depleted of these ions and current is locally suppressed. The ring-like shapes of the particles are due to the geometric effect of restricted transport in the gap between the substrate and particle, leading to deeper depletion of this region.

Bard's group investigated catalytic activity of Pt nanoparticles (PtNP) deposited on highly oriented pyrolytic graphite (HOPG) toward the hydrogen oxidation reaction.¹⁸⁷ They employed SECM in constant height mode with a 180 nm tip diameter Pt UME. To separate the sample's topography from activity, a dual redox mediator approach was used. Topography was probed at 0.3 V applied to the substrate and -0.1 V (*vs* Pt) to the tip in electrolyte containing ferrocenyl methyl trimethylammonium ($FcTMA^+$) perchlorate. $FcTMA^+$ was oxidized at the tip to $FcTMA^{2+}$, which was then reduced at the substrate, generating current proportional to the local topography (Figure 16e). Particles were not well-resolved, but

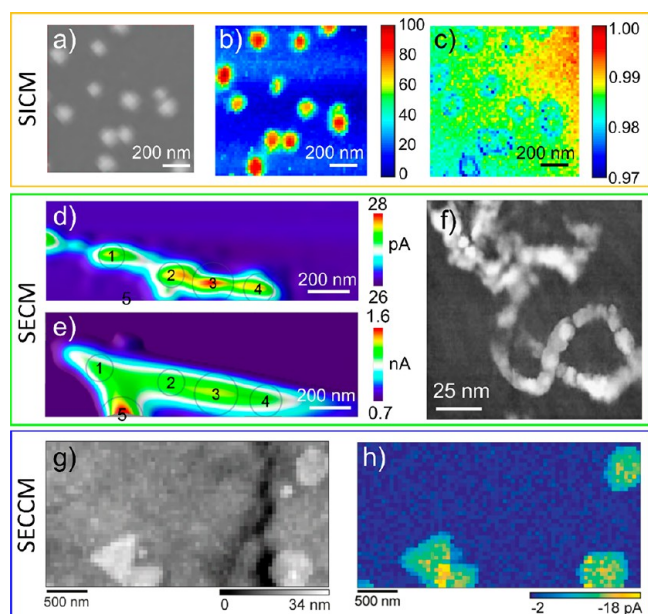


Figure 16. Nanoscale imaging of electrochemical activity in liquids. SICM imaging: (a) SEM image of Au nanoparticles on a carbon fiber, (b) topographic map, and (c) normalized current map ($V = 0.65$ V) of the same region. Measurements were performed in 30 mM NaOH and 3 mM NaBH_4 aqueous electrolyte to probe the nanoparticles catalytic activity in oxidizing BH_4^- . Adapted with permission from ref 188. Copyright 2017 American Chemical Society. SECM imaging: (d) Current map of Pt nanoparticles on HOPG substrate probed at $V_{\text{tip}} = -1.0$ V, $V_{\text{substrate}} = -0.4$ V vs Pt (this map reflects activity of the H^+/H reaction) and (e) current map of the same region recorded at $V_{\text{tip}} = 0.3$ V, $V_{\text{substrate}} = -0.1$ V vs Pt (this map reflects topography of the sample, or activity of the $\text{FcTMA}^+/\text{FcTMA}^{2+}$ reaction). Individual nanoparticles are enumerated. Adapted with permission from ref 187. Copyright 2016 American Chemical Society. (f) A high-resolution image (total current map) of DNA fragments on a mica substrate recorded with SECM. Reprinted with permission from ref 194. Copyright 1999 National Academy of Sciences. SECCM imaging in voltametric hopping mode: (g) topographic and (h) current maps of gold nanocrystals on a glassy carbon substrate at $V_{\text{tip}} = -0.43$ V vs RHE in 100 mM H_2SO_4 visualizing hydrogen evolution reaction activity of the sample. Adapted with permission from ref 189. Copyright 2018 Royal Society of Chemistry.

five of them have been identified. Imaging electrocatalytic activity of the particles was done in a different electrolyte (containing HClO_4) at -1.0 and -0.4 V vs Pt applied to the tip and substrate, respectively. The obtained current maps were fit to simulations, yielding the shape, orientation, and catalytic activity of each particle. An example of high-resolution SECM imaging is shown in Figure 16f.¹⁹⁴ Here, a strand of DNA on a mica substrate was imaged with a tungsten STM tip, which formed an UME with the water meniscus due to high air humidity. Bentley and Unwin have demonstrated high-resolution imaging of gold nanocrystals on glassy carbon substrates with hopping mode SECCM using an UME with a single channel (opening diameter ~ 30 nm).¹⁸⁹ The inner UME wire was a palladium–hydrogen quasi-reference electrode in a 0.1 M HClO_4 solution. Figure 16g shows an SECCM topographic image of the sample with several triangular and hexagonally shaped gold nanocrystals. The corresponding current map, reflecting the activity of the hydrogen evolution reaction, is presented in Figure 16h.

Interestingly, since the gold crystals have the same orientation, the current (activity) of their top (111) surface is the same (-12 pA).

The future development of the UME-based SPM techniques, currently underway, focuses on increasing the spatial resolution, deconvoluting the measured signal into topography and electrochemical activity, combining different techniques together (e.g., AFM-SECM, SICM-SECM, etc.), and using nonaqueous electrolytes for battery research. More information on these methods can be found in several recent reviews.^{176,177,195–198}

Hysteretic I – V Detection in Solids. Amperometric techniques are widely used in electrochemistry to study mass and charge transfer reactions, relaxation processes, to determine Coulombic efficiency of reactions, and the conductivity of electrolytes. It may seem straightforward to use the same methods for SPM electrochemical studies in solids; however, the nanoscale level imposes several limitations that severely affect the implementation of the chosen method or data interpretation. The first challenge was mentioned above: In the all solid-state SPM studies, no reference electrode is present. Second, Faradaic processes in nanoscale volumes generate currents well below the detection limit of existing current amplifiers. Recalling the example given in the ESM section, delithiation of a 20 nm^3 volume of LiCoO_2 to $\text{Li}_{0.5}\text{CoO}_2$ under the tip will cause a local expansion of about 1.2 nm (detectable by ESM) and a current flow of about 20 fA in 1 s (undetectable by current amplifiers). Thus, direct Faradaic current detection by SPM is usually not feasible, as measurable currents in ionic conductors modify the samples on the micrometer, rather than the nanoscale. It is also noteworthy that interpretation of the much more localized ESM results can be ambiguous, since piezoelectric, flexoelectric, Vegard strain, Faradaic, charge injection, chemical dipole, and other effects can contribute to the ESM signal. The third problem of downscaling classical amperometric techniques is the large impedances of the tip–sample junction, roughly given by the spreading resistance equation: $R_S = \rho/4r$, where ρ is the sample's resistivity, and $r \sim 10$ – 100 nm is the tip–surface contact radius.¹⁹⁹ For an ion conductor with a typical resistivity of $10^4\ \Omega\cdot\text{cm}$, $R_S = 2.5\ \text{G}\Omega$. Coupled with typical stray capacitances in AFM systems (10 – 100 pF), this gives an RC constant of an impedance measurement of 4–40 s, obscuring any processes that occur in the sample at lower time scales (note that for potential detection described above, this limitation is irrelevant). For this reason, although AFM-based nanoimpedance spectroscopy imaging methods were introduced in the early 2000s,^{146,147,199} they have not been widely applied to electrochemical systems. A related method, scanning near-field microwave microscopy, has recently been applied to probing metal electrodeposition in a liquid through a thin membrane;²⁰⁰ however, in this method the microwave reflectivity is a proxy signal for the formation of the metallic phase and the microwave radiation does not induce the electrochemical process *per se*.

Overcoming these shortcomings is possible by using the memristive detection scheme implemented in the first-order reversal curve current–voltage (FORC-IV) SPM technique.²⁰¹ Memristive materials are mixed ionic–electronic conductors (MIECs), in which ions act as mobile dopants, modifying the local electronic structure of the material as they electromigrate through the lattice.^{202–204} In continuous media, the cross-dependence of ionic and electronic conductivities can be

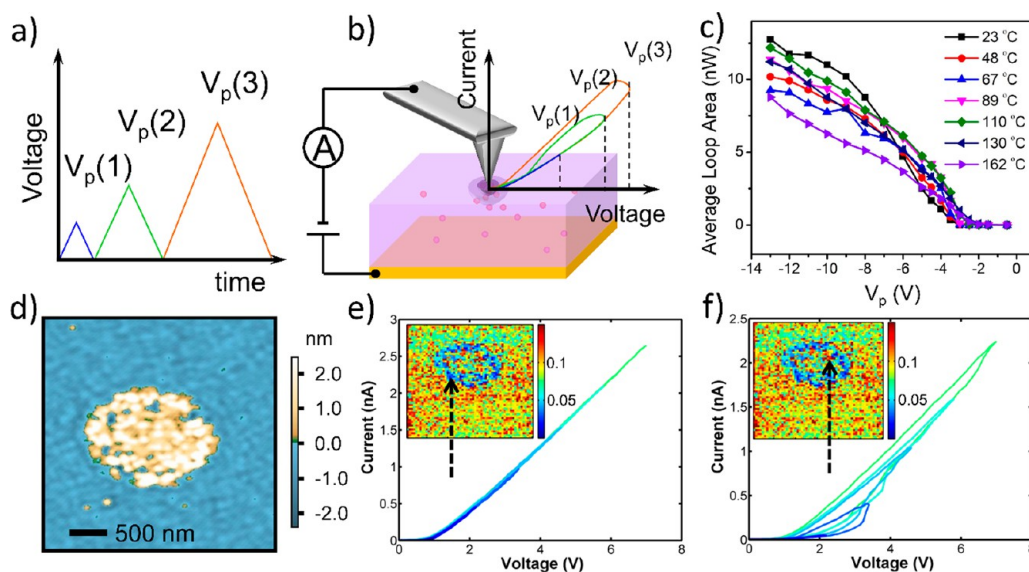


Figure 17. The FORC-IV method for probing local electrochemistry. (a) A train of slowly-varying triangular voltage pulses with ever-increasing peak biases (V_p) applied *via* conductive tip to sample surface (an ionic conductor) as depicted in (b). Current response measured off of the bottom electrode is nonhysteretic at low voltages but becomes hysteretic at higher V_p 's due to motion of ions acting as mobile dopants. The hysteretic IV curves loop area can be plotted as a function of V_p to determine at what voltage ionic transport is activated (threshold voltage, V_{th}). (c) FORC-IV loop area vs V_p for different temperatures as measured on Ca-BFO shows that V_{th} shifts to lower values at higher temperatures. (d) Topographic image of a surface defect with high local conductivity (on Ca-BFO) on which a FORC-IV mapping was performed. (e, f) FORC-IV responses at selected locations indicated with arrows on loop area maps. Defected structure has high electronic conductivity and non-hysteretic, almost linear IV response, while other regions of the sample have low electronic conductivity and are easily activated by local oxygen vacancy motion, producing a highly nonlinear and hysteretic response. Reprinted with permission from ref 201. Copyright 2013 The American Chemical Society.

described by the Onsager reciprocity matrix and can help determine the charged species concentration and potential profiles in a Hebb–Wagner-type polarization of the MIEC,²⁰⁵ or during formation of a p–n junction upon biasing.²⁰⁶ An important aspect of memristive MIECs is that a minuscule change in the ionic state of the system (*i.e.*, polarization) is amplified into detectable variations in the electronic transport. Materials like LiCoO_2 (Li^+ conductivity),²⁰⁷ Ca-BiFeO_3 (O^{2-} conductivity),²⁰⁸ and CuInSe_2 (Cu^+ conductivity)²⁰² are good examples of such behavior. In some cases, a simple conductive AFM mapping experiment can reveal the spatial distribution of ions. For instance, $\text{Li}_4\text{Ti}_5\text{O}_{12}$ and $\text{Li}_7\text{Ti}_5\text{O}_{12}$ phases can be reversibly cycled between each other, but the first one is electronically insulating, while the second is conductive, which links the AFM-measured electronic current maps to the local Li^+ concentration.²⁰⁹ Note that the lattice expansion upon lithiation in this system is only 0.2%, and thus cannot be detected by ESM.

Materials with a more sophisticated behavior, in which both the reactant and product are MIECs or the insulator-conductor transition proceeds gradually, can be studied with the FORC-IV technique. Figure 17b shows a schematic of the FORC-IV spectroscopy measurement.²⁰¹ A conductive AFM tip in contact with the sample serves as a moving electrode through which a slowly varying DC waveform is applied to the material. The waveform (Figure 17a) consists of a train of triangular pulses with increasing peak biases (V_p). The conductive response of the material is recorded spatially, pixel-by-pixel, by the current amplifier connected to the bottom electrode as the tip moves between the pixels, applying the voltage waveform at each of them. At low V_p values, a MIEC behaves as a semiconductor with a nonhysteretic IV curve, unless the circuit includes a large capacitance or significant Joule heating occurs

at the tip–surface junction. As V_p increases, at some point the ionic subsystem of the material will be activated, and electromigration of ions will increase the electronic conductivity, making the reverse IV curve different from the forward one and causing an IV hysteresis. Thus, hysteresis can serve as a measure of the local electrochemical activity.

As an example of this detection principle, Figure 17c presents a plot of the FORC-IV hysteresis loop area vs peak bias as measured on Ca-BiFeO₃. Below about -3 V, loops are nonhysteretic with a zero loop area. Above that threshold, the tip creates an electric field strong enough to attract the existing or create new oxygen vacancies (ions), which changes the oxide's electronic conductivity and opens a bias-dependent IV hysteresis. Increasing the temperature decreases the threshold voltage, as expected: $V_{th} \propto \frac{\Delta S_r^\circ}{nF} T$, where ΔS_r° is the change in the standard entropy of formation of the reaction of oxygen vacancy formation (it is negative), n is the number of electrons involved, and F is the Faraday constant. An example of surface mapping with FORC-IV is shown in Figure 17d–f. Here, Figure 17d is a topographic image of a surface defect with increased electronic conductivity and Figure 17e,f displays FORC-IV curves recorded at specific locations within the defect, as indicated by arrows. The insets are FORC-IV loop area maps of the defected area, where the colors from blue to red indicate the degree of hysteresis in the local IV curves, thus showing the distribution of the oxygen vacancy activity within the defect.

As mentioned, FORC-IV is subject to artifacts if a parasitic capacitance is present in the external circuit or the sample heats-up locally. Avoiding the capacitive response is possible by increasing the voltage step height-voltage sweep rate ratio above the RC constant of the circuit, by cancellation of the

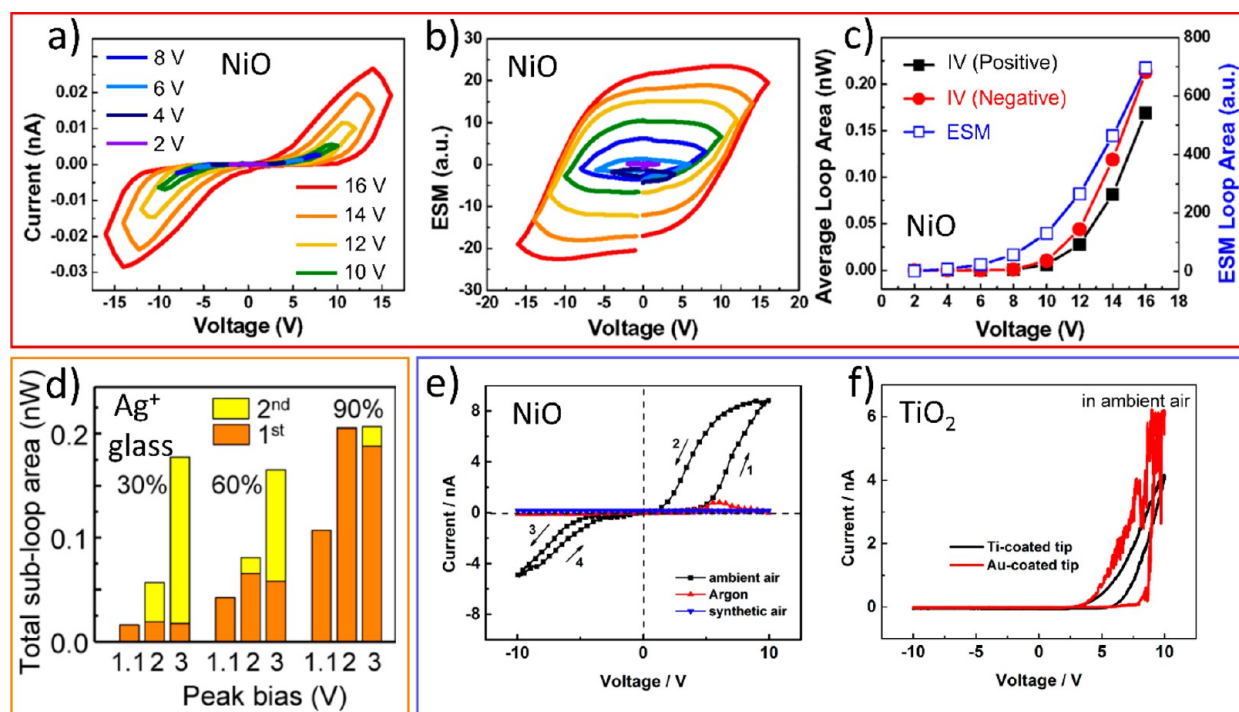


Figure 18. FORC-IV comparison with ESM and the importance of counter-reactions. (a) Bipolar FORC-IV and (b) ESM curves measured on a NiO thin film show a hysteresis appearing beyond certain V_p , which can be determined from (c) where loop areas are plotted vs V_p . Reprinted with permission from ref 212. Copyright 2013, Springer Nature. (d) Histogram of FORC-IV loop area vs V_p as measured on a silver-ion conducting glass at various air humidity values. At 0% humidity, negligible current and hysteresis are detected (not shown). Reprinted with permission from ref 90. Copyright 2015, The American Chemical Society. (e) Selected hysteretic FORC-IV responses of a NiO sample in different ambient. Reprinted with permission from ref 214. Copyright 2018 American Chemical Society. (f) FORC-IV responses of a TiO₂ sample measured with AFM tips with Ti and Au coatings. Reprinted with permission from ref 215. Copyright 2018 Elsevier.

displacement current,²¹⁰ or by using postprocessing (such as Bayesian inference).²¹¹ Joule heating can be estimated and avoided based on numerical modeling of heat generation and flow.

Ensuring artifact-free FORC-IV measurements can be done by cross-referencing with another technique. Figure 18a–c presents a direct comparison of probing electrochemical activity by FORC-IV and ESM on a nonferroelectric memristive sample, a thin NiO film.²¹² Migration of oxygen vacancies and nickel interstitials in this material alters its electronic conductivity and causes local expansion/contraction. The ESM and FORC-IV curves, recorded simultaneously, show a very similar hysteretic behavior, despite having very different shapes (Figure 18a,b). The ESM loop area dependence on the peak bias has a somewhat lower threshold voltage than the FORC-IV (Figure 18c), which can be explained by a higher sensitivity of the ESM technique and the fact that ESM probes reversible processes, whereas the FORC-IV probes both reversible and irreversible processes.

Discussions in electrochemical studies are usually focused exclusively on the half-reactions at the working electrode. For classical electrochemical techniques, this is normal, as the opposite half-reaction is enabled by the supporting electrolyte, proceeds at the counter electrode and is generally well-understood. However, counter-reactions are very important for the solid-state AFM studies as they control (*via* charge balance) the rate of the reaction at the tip–surface junction. If the counter-reaction is not established on purpose, it can be either absent (and no reaction will occur at the tip), or water, present in the ambient, will provide it. As an example, consider

FORC-IV measurements performed on a Ag-ion conductor in contact with an inert gold electrode.²¹³ A negative bias applied to the tip is expected to create a metallic silver particle under it: $\text{Ag}^+ + e^- \rightarrow \text{Ag}^0$. But since the counter electrode is inert and cannot supply any ions to neutralize the negative charge injected from the tip (negatively charged silver vacancies under the tip), this reaction will not proceed unless the sample is exposed to humid air. Water from the ambient can condense on the counter-electrode surface and decompose: $2\text{H}_2\text{O} (\text{l}) \rightleftharpoons 4\text{H}^+ + \text{O}_2 \uparrow + 4e^-$, with the H^+ ions being injected into the solid electrolyte. The FORC-IV loop area and size of the formed silver particles become proportional to the gas humidity, as shown in Figure 18d.

A similar effect was reported for NiO samples used for resistive switching memory devices.²¹⁴ Figure 18e shows FORC-IV curves recorded on a NiO film in humid ambient air, dry air, and argon atmospheres, with only the humid air environment being sufficient to induce memristive behavior in the material. This can be explained by the lower activation barrier for the water splitting reaction (with subsequent injection of H^+ or OH^- ions into the sample and modification of its electronic conductivity) than oxidation/reduction of oxygen: $\text{O}_\text{O}^\times \rightleftharpoons \text{V}_\text{O}^\bullet + \frac{1}{2}\text{O}_2 + 2e^-$ (Kröger–Vink notation used). Parasitic and uncontrolled reactions may also take place at the tip itself if the experiment is not well designed. Using a Ti-coated tip on a TiO₂ sample produces a much smoother and stable FORC-IV response than the IV curve recorded with an inert gold coating,²¹⁵ which cannot supply Ti to the sample (Figure 18f).

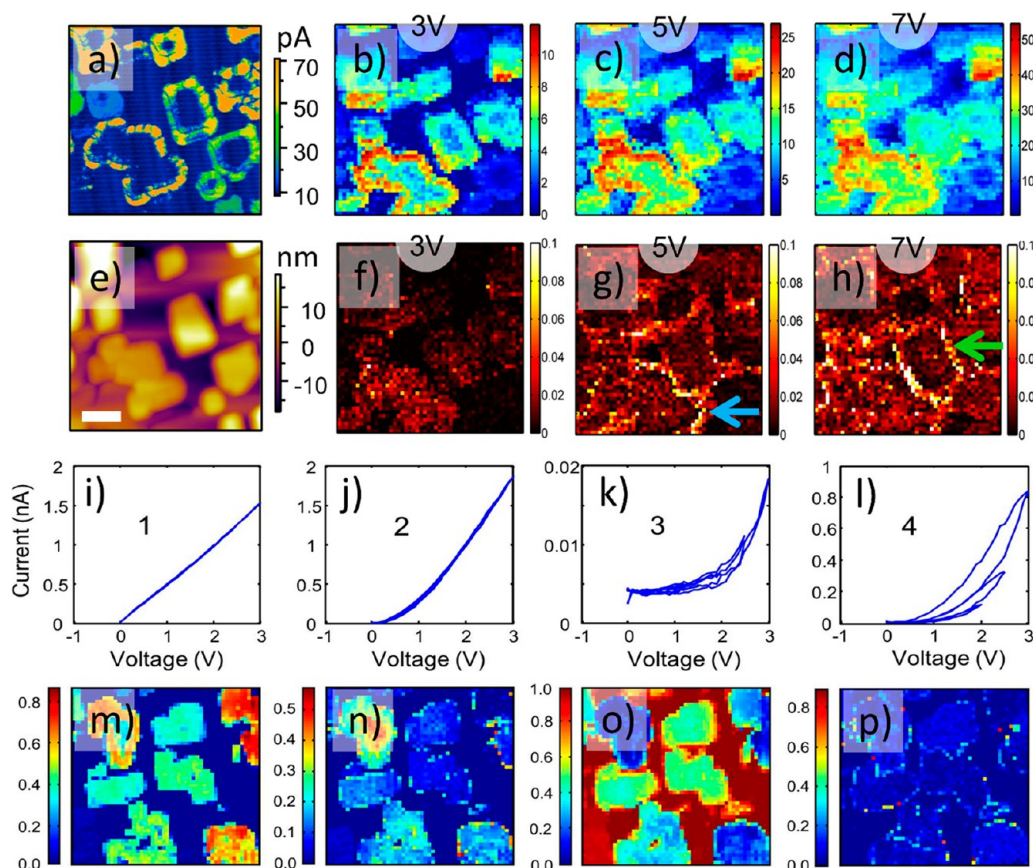


Figure 19. Deep data analysis of a BFO–CFO nanocomposite FORC-IV data. (a) Current map at 0.1 V shows higher conductivity on the BFO–CFO tubular interfaces of CFO nanopillars observed in topographic image (e). (b–d) Current maps for $V_p = 3, 5,$ and 7 V of the FORC voltage waveform used to probe sample. FORC-IV loop area maps (f–h) look very different from the current maps and convey a different type of information. Map in (f) is mostly featureless, but different interfaces (shown by arrows) become activated at higher voltages (in maps (g) and (h)) and manifest spatial difference in the onset of electrochemical process. Note that neither current nor loop area maps contain information on the shape of the local IV curves: It was present in the initial data set but was lost during data slicing/compression. 4D FORC-IV data sets ($I = f(x, y, V, V_p)$) can also be losslessly deconvoluted into a set of IV curves (components) (i–l) and corresponding loading (intensity) maps using BLU. Sets of graphs and 2D maps retain all information initially present in FORC-IV data set. Extracted IV components can be fitted to appropriate physical models to unravel local transport behaviors. Panels (a–h) are adapted with permission from ref 217. Copyright 2013 The American Chemical Society. Panels (i–p) adapted with permission from ref 218. Copyright (2013) The American Chemical Society.

Analysis of large FORC-IV data sets presents the challenge of data visualization and extraction. In the examples discussed so far, only selected IV curves or integrated FORC-IV loop area maps have been shown. But the full FORC-IV data set represents much more than this, including multiple IV curves with their unique shapes for every location on the sample and containing important information about the local charge transport properties, which can be correlated with the material's structure. Thus, by visualizing the four-dimensional (4D) FORC-IV data set ($I = f(x, y, V, V_p)$) using the loop area representation, much of this information was lost.

This problem can be solved by invoking statistical analysis tools with a properly chosen set of constraints. One such tool is Bayesian linear unmixing (BLU)²¹⁶ that presents data Y as a linear combination of position-independent endmembers, M , with respective relative abundances, A , corrupted by additive Gaussian noise, N : $Y = MA + N$. This method features several built-in constraints that enable physical interpretation of the results: non-negativity ($M_i \geq 0, A_i \geq 0$), full additivity, and sum-to-one ($\sum A_i = 1$) constraints for both the endmembers and the abundance coefficients. A $\text{BiFeO}_3\text{-Co}_2\text{FeO}_4$ (BFO-CFO) nanocomposite was used to compare a standard

visualization of FORC-IV data with the losslessly compressed BLU presentation. In this nanocomposite, the tubular interfaces between the BFO matrix and the embedded CFO nanopillars feature high electronic conductivity, presumably due to accumulation of oxygen vacancies at the interfaces.²¹⁷ This is shown in Figures 19e (topography) and 19a (current map at a low voltage of 0.1 V). The interfaces are expected to be more electrochemically active and manifest a higher FORC-IV hysteresis. Indeed, the loop area maps (Figure 19f–h) for three peak biases of 3, 5, and 7 V highlight the interfaces that are activated one-by-one as the peak bias is increased. Note that these maps look very different from the current maps recorded simultaneously at the same peak bias (Figure 19b–d), conveying a different type of information (again, FORC-IV data are not simply the total conductivity of the sample). If the same data set is unmixed using the BLU into four conductive components (on the number of components and how to choose them, see ref 218), then four IV spectra are obtained that represent the typical behaviors of the sample (Figure 19i–l) and four abundance maps are obtained (Figure 19m–p) that show the spatial distribution of these interfacial behaviors. Importantly, these eight images (Figure 19i–p) display all of

the information that the original 4D data set contained, which is presented in a simple and understandable form. Component 1 (Figure 19i) is the case of ohmic conductance; component 2 (Figure 19j) is the electronic transport through a barrier; component 3 (Figure 19k) is the low, noise-dominated, conductivity of the BFO matrix; and component 4 (Figure 19l) reveals the memristive hysteretic behavior of the interfaces. Because of the properly selected constraints of the BLU analysis, these components are scaled in amperes (rather than in abstract numbers as in case of principal component analysis) and can be fitted to appropriate physical models, allowing for the extraction of the conductivity governing parameters such as the local ion dopant concentration. The conductance is dependent on the oxygen and water vapor pressure, and the two active transport mechanisms in the nanocomposite are ohmic conductance and Schottky emission.²¹⁹ The Schottky barrier and local donor concentration are controlled by the ambient *via* electrochemical water splitting. FORC-IV imaging has also been applied to a Sm-doped CeO₂-SrTiO₃ (SDC-STO) nanocomposite to reveal the ionic conductance in the SDC columns only.²²⁰

Transition to the Atomic Scale. Of obvious interest is the transition from the mesoscale electrochemistry to probing electrochemical phenomena on the atomic level. This is of interest from several perspectives, both in terms of the new materials knowledge it offers and new concepts and descriptions it necessitates. Indeed, analysis of mesoscopic SPM data can often be performed using concepts and methods developed for macroscopic electrochemistry, including the effects of nanoscale confinement, exclusion, and field-dependent mobility. This analysis often necessitates corrections for very high fields existing in the tip–surface junction. The bias of 10 V applied to the 1–10 nm contact areas yields 10⁹–10¹⁰ V/m fields, sufficient to induce the field-activated ionic transport and allowing for highly unusual electrochemical processes. In fact, even more interesting conclusions can be derived *via* simple analysis of the electrostatic phenomena in the tip–surface junction. In this case, the electric field at the contact junction (or periphery of the tip–surface contact) is diverging in the classical model, suggesting the need for atomic scale cutoff length as a relevant parameter. Therefore, even in mesoscopic SPMs, the atomistic phenomena are essential, albeit not necessarily obvious. At the same time, transition to the observable atomic scale severely limits the number of measurement modalities (since mesoscopic concepts are no longer applicable), but at the same time enables the observation of electrochemical processes atom-by-atom.

For a global stimulus, insight into the electrochemical behaviors can be derived from electrochemical STM. Here, classical STM measurements are conducted in a liquid environment, providing atomically resolved information on the surface atomic structure at the different stages of electrochemical processes on the surface of the electrode in an electrochemical cell. However, of greater interest are new capabilities for probing molecular- and atomic-scale electrochemistry enabled by advanced imaging modes. Here, we are going to discuss the observations of molecular layering in liquids on electrified interfaces and tip-induced single atom electrochemistry.

Molecular Layering in Liquids. An approach to explore electrochemical processes on the molecular- and atomic-scale is based on direct force imaging of molecular ordering perpendicular to the surface as most generally applied to

ionic liquids. Room-temperature ionic liquids (RTILs) are liquids composed purely of charged ions. They have drawn significant attention in many fields,^{221–223} especially energy-related applications,^{224–226} due to their low volatility and significant temperature, chemical, and electrochemical stability. The strong cation–anion interactions within the RTILs and their large ion size make the conventional Gouy–Chapman–Stern model,^{227–229} which describes the electric double layer (EDL) structure of a diluted solution at the solid–liquid interface, not applicable. Many simulation and experimental efforts have been focused on developing the RTIL's EDL structure during the past 15 years.^{230–241} It has been theoretically predicted by molecular dynamics (MD) simulations that RTILs organize and form a layered structure on the top of a flat surface. This layered structure can be visualized with nm resolution by AFM force–distance measurements,^{242–246} in which the deflection of the tip (which then was converted into force acting on the cantilever due to interaction with the environment) was recorded as a function of distance to the sample surface.

Figure 20a–c shows the force–distance measurements of the model system 1-ethyl-3-methylimidazolium bis-(trifluoromethylsulfonyl)imide (Emim-TFSI) ionic liquid on mica. As the AFM tip approaches the mica surface (Figure 20a), the tip begins to experience resistance due to ionic liquid layering that creates regions of higher density. When the force is large enough for the tip to rupture the ion layer and reach

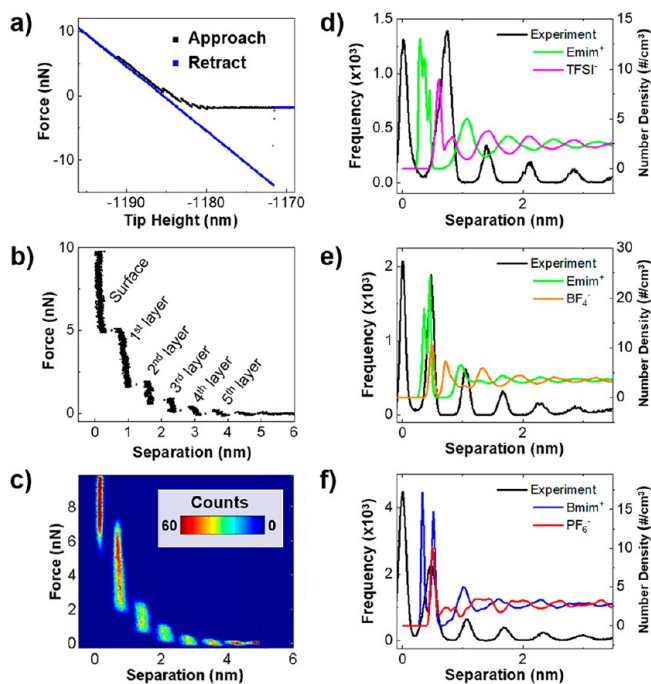


Figure 20. AFM force–distance measurement to extract ion layering information for ionic liquids on mica and its comparison with MD simulations. (a) Single force–distance approach and retraction curves showing multiple ion layers formed on mica surface. (b) Single force separation plot of curve shown in (a). (c) 2D histogram of 50 consecutively measured force–separation curves. Histograms of separation values and ion number density profiles obtained from MD simulations for (d) EmimTFSI, (e) EmimBF₄, and (f) BmimPF₆ on mica surfaces. Adapted with permission under a Creative Commons license from ref 248. Copyright 2016 Nature Publishing Group.

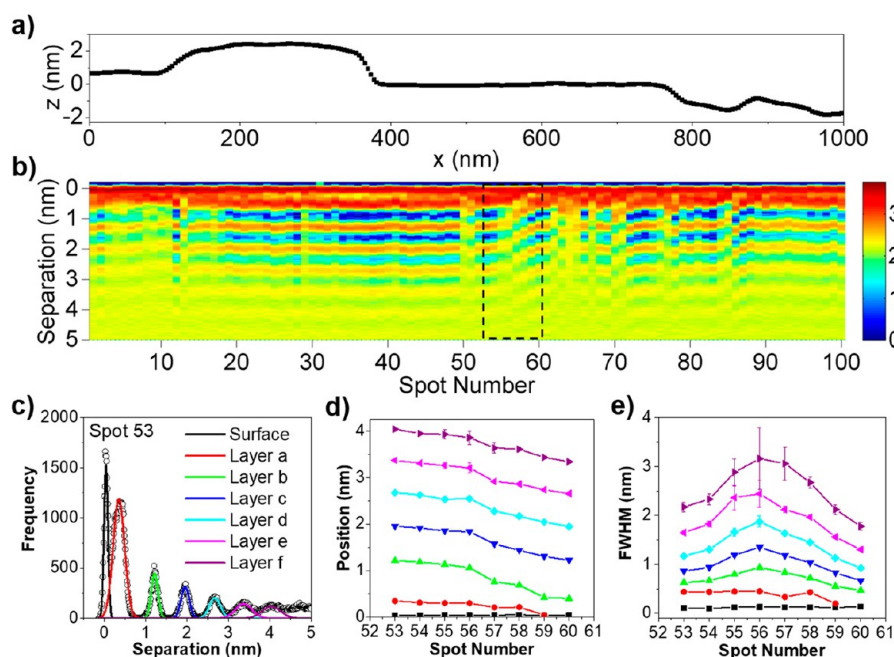


Figure 21. Multiple defects in ion layer structure across long lengths and analysis of defects. (a) Line profile of topography of HOPG surface where force–distance curves were collected for 100 positions along same line. (b) Top-down view of separation histograms for all 100 locations (black box highlights location of observed dislocation defect). (c) Separation histogram for position 53 (highlighted region in b) with Gaussian functions fit for each ion layer. (d) Position and (e) fwhm of Gaussian functions used to fit separation histograms. Adapted with permission from ref 247. Copyright 2015 Elsevier.

the next layer that is closer to the sample surface, a discontinuity (or a step) appears in the approach curve. Once the tip is in contact with the mica surface, no additional discontinuities are observed with increasing force since only tip bending is measured. During tip retraction and once the tip–sample interaction forces are overcome, the cantilever snaps out of contact. The force–separation curve (Figure 20b) is obtained by transforming the tip height into a tip–sample separation distance, offsetting the force far away from the surface as a zero force and subtracting the surface position. The ion layer positions can then be clearly identified as the vertical lines in the plot (Figure 20b). The 2D histogram of 50 force–distance curves (Figure 20c) confirms the statistical reproducibility of this method to investigate the process of ionic liquid layering. The histograms of the measured ion layer separation values only (black curves in Figure 20d–f and Figure 21c) are used to obtain quantitative information; for example, the individual ion layer position and degree of ordering within each ion layer can be extracted from the peak position and full width at half-maximum (fwhm) of each peak, respectively.^{247,248} The ion number density profiles of each ion above the substrate surface obtained from MD simulations show excellent agreement with the ion layer positions measured by AFM force measurements.^{242,247,248} Both the ion layer position and extent of ordering within each layer are independent of the tip chemistry, tip radius, and cantilever geometry.²⁴⁸ The AFM tip is only sensitive to one type of ion in the RTILs, in this case the anions, as observed by comparing the AFM results with the MD simulations (Figure 20d), which show an excellent agreement between the predicted and measured ion positions. Interestingly, the predicted positions for the cation layers do not show up in the experiment. Systematic variations of the mass and volume of the ions of the RTILs confirm that the AFM tip is more sensitive to ions with

a larger volume in the system, suggesting the imaging mechanism is based on volumetric displacement (Figure 20d–f).²⁴⁸

This approach was applied on a larger scale to include both out-of-plane and in-plane information in order to reconstruct a cross-section of the ionic liquid double layer structure.²⁴⁷ Figure 21a shows the height profile of a 1 μm -line measured on highly oriented pyrolytic graphite (HOPG), where 100 points along the same line were selected to perform force–distance measurements in the Emim-TFSI ionic liquid. The results of each point are presented as a top-down view of the separation histograms in Figure 21b, where red indicates the ion layer position and blue are the gaps in the force–distance curves. Across the measured line, several “kinks” are observed in the ion layer ordering. Knowing that only the anion positions are measured for this RTIL, the kinks represent the anion layer closest to the surface steps, and all the other ion layers react to this by bending around the created edge dislocation, which seemingly are not related to the underlying topography. On the left side of the region across the dislocation (highlighted region in Figure 21b), the first ion layer is located at 0.3 nm above the surface. Moving from left to right across the dislocation region, it is evident that the first ion layer position shifts closer to the surface and eventually disappears; the spacing between other ion layers does not vary. In this way, the second layer moves toward the substrate and eventually becomes the first adlayer on HOPG. This transition can happen on a different length scale from 50 to 80 nm. The ion layer positions and fwhm’s of each layer at each position in the selected zone shown in Figure 21b are extracted from the Gaussian fitting of each peak in the separation histograms (Figure 21c shows an example at position 53). The kink defect in the ion layering can be clearly observed from the peak positions. The fwhm of each peak (Figure 21e), which is related to the degree of ion ordering

within the layer, shows that the first adsorbed layer retains a narrow peak width during the transition, indicating strong ion–substrate interaction that preserves a high degree of ion ordering. The subsequent ion layers experience less influence from the substrate surface, resulting in less ordering and broader fwhm's compared to the first ion layer. For the same ion layer, the peak width first increases then decreases to its original value during the transition, which means that the ion layers become less ordered during the transition when they are moved out of their equilibrium position.

The AFM force–distance measurements and the measurement protocols developed for carbon-based surfaces have recently been applied to investigate the mechanism of charge carrier enhancement in ionic liquid gated thin-film oxide transistors.²⁴⁹ The double-layer structure of 1-Hexyl-3-methylimidazolium (Hmim)-TFSI ionic liquid close to the source electrode on an amorphous indium gallium zinc oxide (a-IGZO) transistor was studied by AFM and MD simulations.²⁴⁹ When increasing the gate voltage from 0 V to +2 V, the first adsorbed ion positions shift closer to the surface, but rather than moving toward the surface in a continuous way, the ion positions undergo abrupt transitions at +0.4 V and +1.0 V (Figure 22a). At the same time, the macroscopically

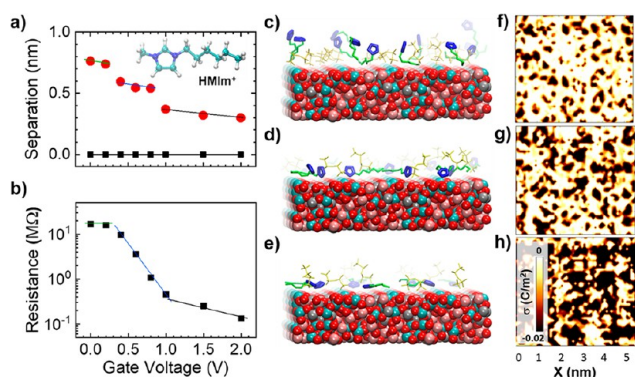


Figure 22. First adsorbed ion layer structure of Hmim-TFSI on a-IGZO and the surface charge distribution of a-IGZO under different bias. (a) Distance of first adsorbed ion layer position and (b) resistance of the oxide channel, calculated from applied source–drain voltage and measured source–drain current as a function of gate voltage. (c–e) Snapshots of innermost ion layer structure and (f–h) corresponding surface charge distribution on a-IGZO surface under different bias. Top (c, f): 0 V; middle (d, g): 0.4 V; bottom (e, h): 1.5 V. Adapted with permission from ref 249. Copyright 2017 The American Chemical Society.

measured source–drain resistance changes its dependence from the gate bias (Figure 22b), indicating a strong correlation between the ionic liquid EDL structure and the device properties. MD simulation results are in qualitative agreement with the AFM results. Upon increasing the gate bias, the first adsorbed cations rotate their alkyl chains parallel to the surface and tilt their imidazolium rings parallel to the oxide surface (Figure 22c–e). Due to the large size and asymmetric shape of the cations, the charge distribution of the first adsorbed ion layer is inhomogeneous. The a-IGZO surface charge induced by the first layer of adsorbed ions, thus, shows disconnected metallic regions, which explain the semiconductor-like conductance of the device. When the bias is increased from 0 V to +1.5 V, cation flattening takes place in response to the bias and increases the EDL density, decreases the EDL

thickness, and generates a large local charge density, which is believed to be linked to the observed changes of conductivity (Figure 22f–h). By combining AFM and MD simulations, the bias effect of the EDL structure and its correlation to macroscopic device performance is revealed, which will benefit future device design. In addition, the developed MD approach can be used to predict the gating phenomena of different ionic liquids.⁹¹

Single Atom Electrochemistry via STM. Finally, of special interest are electrochemical measurements on the atomic level. Here, the natural question is whether bias-induced phenomena on the atomic level can be even classified as electrochemical. We pose that this is indeed correct. First, based on the (somewhat loose) definition of electrochemistry as the chemical changes and ionic transport induced by electrical current or voltage, chemical changes induced by tip bias comport to this definition independent of the length scale. This, for example, will differentiate these phenomena from classical STM-based atomic manipulation, where tip motion in the vertical and lateral directions at fixed bias is used for atomic motion. Second, broad classes of phenomena, ranging from corrosion initiation, electromigration, and indeed tip-induced electrochemistry, are considered as electrochemical despite that the relevant length scale is atomic. Of course, generally these are analyzed theoretically, or on macroscopic objects, and hence atomic scale electrochemistry is sometimes considered as a contradiction in terms. Nonetheless, the lack of prior concepts and tools is not the reason not to extend the concept of electrochemical studies to nanometer and atomistic level, as done here.

Here, we discuss how the concept of local electrochemical characterization can be extended to atomic level *via* the concept of memristive detection in STM. Recently, significant progress on controlling atomic filaments in resistive switching devices with STM has been reported.^{88,250,251} The question is: Can we do electrochemistry on individual atoms? Figure 23a shows an STM topographic image of a freshly grown La_{0.63}Ca_{0.37}MnO₃ (LCMO) film with (La,Ca)O termination islands (bright region at center of topographic image as recorded at room temperature).²⁵² The STM tip was placed at the location of the red dot, the z-feedback was switched off, and a FORC-IV waveform (shown inset, Figure 23c) was applied to the sample. The recorded IV curves exhibited a jagged appearance but were clearly hysteretic (Figure 23c). Imaging the surface following the FORC-IV measurement revealed that two oxygen vacancies had been created in the vicinity of the tip's former location (Figure 23b). Formation of individual oxygen vacancies with a STM tip bias and correlating this process with the functional response can help determine vacancy ordering preferences and provide experimental data for verification of first-principle calculations. For small bias excursions, the tip bias does not induce electrochemical changes of the surface, and hence the forward and reverse tunneling characteristics remain the same. For sufficiently high bias, the tip pulls an oxygen atom from the lattice inducing an electrochemical process. The corresponding forward and reverse IV curves do not coincide and the magnitude of the hysteresis and corresponding voltage provides the information on atomic-scale electrochemical process. Subsequent imaging of the surface illustrates that indeed the process resulted in formation of two oxygen vacancies.

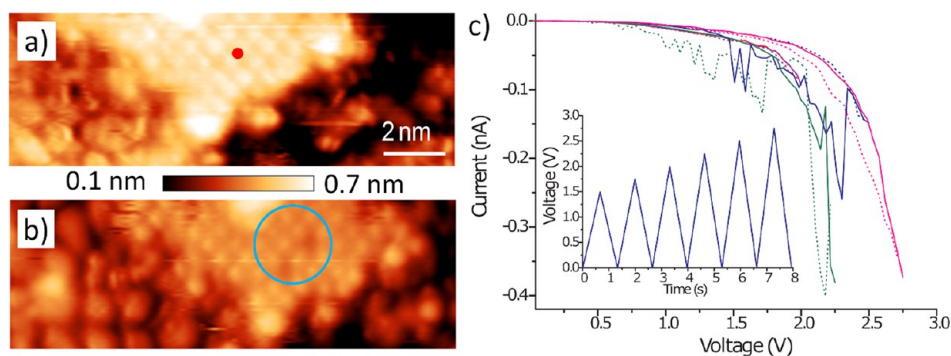


Figure 23. Atomic-scale electrochemistry. (a) STM image of a $\text{La}_{0.63}\text{Ca}_{0.37}\text{MnO}_3$ film. Red dot indicates tip location for application of FORC-IV waveform (shown as an inset in (c)). (b) STM image after FORC-IV measurement at single location shows removal of two oxygen atoms from lattice (highlighted with circle). (c) FORC-IV response corresponding to removal process. Reprinted with permission from ref 252. Copyright 2015 AIP Publishing.

This approach demonstrates the obvious challenges of reproducibility and interpretability. For the former, the tip state can change due to the reaction (e.g., an oxygen atom can bind to the tip apex). Correspondingly, automatic tip conditioning as, for example, proposed by Wolkow *et al.*²⁵³ can be a solution.

The broad adoption of tip conditioning and image interpretation will allow us to significantly extend the reproducibility and statistics of these measurements, enabling statistically significant studies of surface transformations. The corresponding mechanisms can be approached in the framework of research on STM-based surface atomic manipulation, albeit the relationship between local measurables and macroscopic electrochemical descriptors is open for exploration. For these, FORC-IV is a powerful technique for probing nanoscale electrochemistry and charge transport in solid-state MIECs without interference from the piezoelectric effect, which is responsible for ESM artifacts. Combined with the BLU deep data analysis, FORC-IV can help extract the numerical values of the physical parameters that govern electrochemically controlled electronic transport. In the future, the FORC-IV method can be used to construct *IV* libraries of conductive behaviors corresponding to specific transport mechanisms and matched to standard models using Bayesian inference methods and knowledge of the tip–surface junction geometry.

Electron Microscopy-Based Imaging of Electrochemical Processes. EM offers a complementary approach for nm-scale and atomically resolved imaging of materials. Correspondingly, of interest are the potential applications of EM methods for probing electrochemical phenomena. In this regard, several comparative comments should be made. First, EM imaging is, by its nature, based on high-energy electrons, resulting in a broad spectrum of possible equilibrium and nonequilibrium beam-induced phenomena. These effects can be immediately visible as large-scale beam damage due to knock-on effects or radiolysis,^{254,255} or they can be more subtle and manifest as increased excitations of individual atoms or atomic groups or electronic excitations. Imaging is typically optimized (e.g., low dose, low energy) to minimize beam-induced knock-on processes, while the roles of local electronic excitations and secondary effects remain largely unexplored. However, intentionally inducing electrochemistry with the beam also opens a possible pathway toward local studies of electrochemical processes, if associated mechanisms can be understood or harnessed. Therefore, in this review we separate

the EM applications for visualization of electrochemical processes induced by external stimuli (e.g., *in situ* imaging studies of electrochemical cells) from the applications associated with using the electron-beam (e-beam) to intentionally induce phenomena. In this section, we discuss EM of externally induced electrochemical processes with an (ideally) non-interacting or minimally interacting e-beam probe.

The rapid development of EM techniques from the late 1930s provides a wealth of information on the mesoscopic structures of many classes of materials, gaining further importance once visualization of extended defects such as dislocations,^{256–260} and subsequently atomic resolution imaging²⁶¹ was demonstrated and reliably established. Advances in recent years, such as aberration-correction for significantly improving spatial resolution,²⁶² detectors with higher sensitivity, and atomic-scale chemical analysis,²⁶³ have made scanning, transmission, and scanning transmission electron microscopy (SEM, TEM, and STEM, respectively; all together (S)TEM) indispensable tools in materials science research. In parallel, significant efforts have been dedicated to imaging dynamic materials processes in nonvacuum environments, which is challenging due to the high vacuum of the (S)TEM column. Variable-temperature and gas-flow environments, static and flowing liquid cells, and electrochemical cells for use within the microscope column are now critical for performing *in situ* imaging and analysis. Many of these advances are summarized in several recent reviews,^{263–267} and instrumentation for conducting (S)TEM electrochemical experiments is now commercially available from a number of manufacturers.

(S)TEM investigations of electrochemical processes in liquids has steadily progressed over the past 15 years or so.²⁶³ This technique utilizes specially fabricated silicon-based chips that are assembled into a microelectrochemical cell (Figure 24a). These cells encapsulate a thin liquid layer enconced within thin (≈ 50 nm or less) SiN_x or similar (e.g., graphene) windows to separate it from the vacuum environment for transmission of the e-beam through the chip and liquid. Metal electrodes can be patterned on the internal surface of microelectro-mechanical systems (MEMS)-based chips and connected to external electronics enabling control over voltage and current within the cell. While the optimization of electrochemical experiments in the (S)TEM environment brings challenges associated with atypical electrode geometries, μm -size regions of interest, and larger

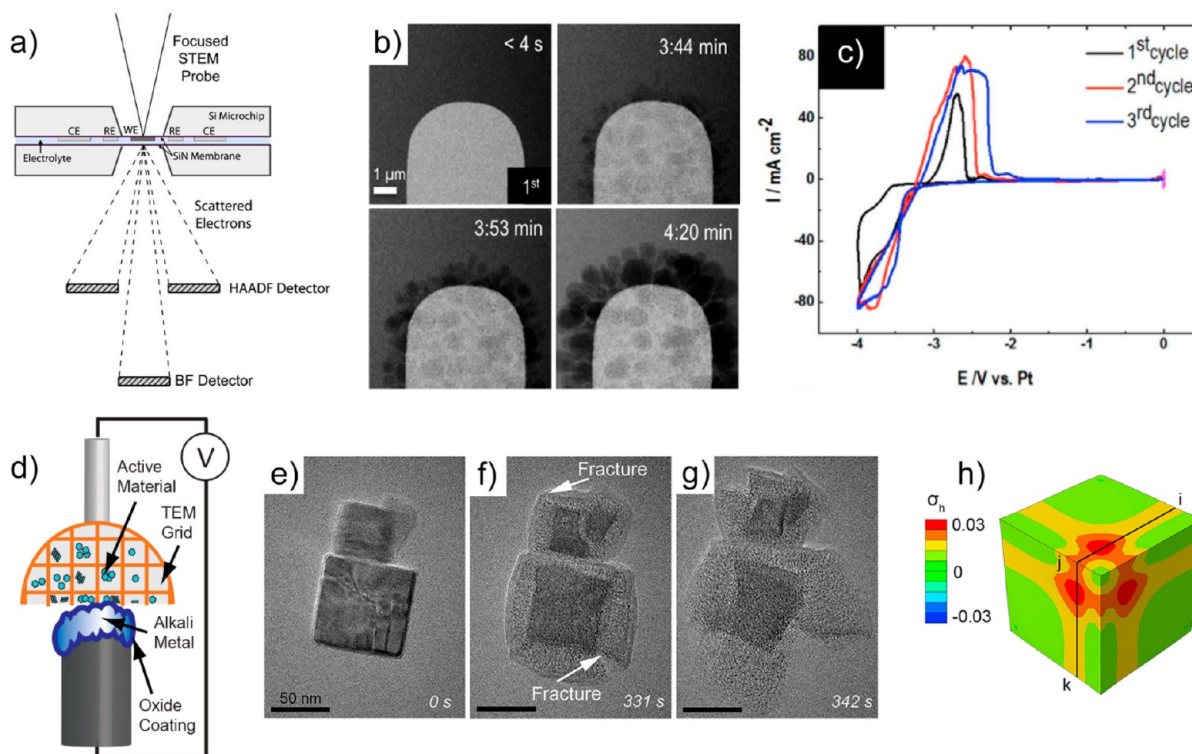


Figure 24. *In situ* (S)TEM of battery electrochemistry. (a) Chip-based liquid electrochemical cell with working electrode (WE), counter electrode (CE), and reference electrode (RE) sandwiched between two SiN_x windows. Reprinted with permission from ref 276. Copyright 2015 The American Chemical Society. (b, c) High-angle annular dark field (HAADF)-STEM images of lithium metal electrodeposition in a liquid cell and corresponding cyclic voltammograms from three cycles. Reprinted with permission from ref 280. Copyright 2015 The American Chemical Society. (d) Schematic of open-cell *in situ* TEM experiment for observing reaction of electrode materials with alkali ions. (e–g) Series of TEM images showing the reaction of two FeS_2 crystals with lithium, revealing volume expansion and fracture. (h) Hydrostatic stress evolution modeled with finite element analysis for the reaction in (e–h) where stress scale is normalized by Young's modulus of this material. Reprinted with permission from ref 301. Copyright 2018 Cell Press.

IR drops in the connections, recent advances in cell geometries have enabled electrochemical behavior to be compared to conventional electrochemical cells²⁶⁸ and general e-beam effects can be ascertained by electrochemical testing with and without beam irradiation.

The first observation of electrochemical phenomena in such liquid cells was carried out in 2003 by Williamson *et al.*, in which nucleation and growth during Cu electrodeposition was monitored.²⁶⁹ In recent years, the wave of interest in battery technologies has led to multiple observations detailing electrochemical lithiation, electroplating, dendrite formation, and growth of the solid–electrolyte interphase (SEI).^{270–279} The electrochemical deposition and stripping of lithium metal has been a particular emphasis due to the importance of understanding growth and SEI formation for the development of high-capacity lithium anodes. (S)TEM imaging revealed the evolution of the lithium metal morphology and its relationship to the structure of the SEI surface layer,^{274,276,280–282} and these types of data have been correlated to measured electrochemical signatures (Figure 24b,c). Phase transformation pathways have been investigated at the nanoscale in materials that form alloys or other compounds during lithium insertion,^{268,283,284} revealing the importance of nonuniform nucleation behavior in controlling transformation pathways. Li^+ insertion into cathode materials has been monitored *via* spatially localized valence changes using energy-filtered TEM imaging.²⁸⁵ Corrosion processes have also been similarly studied.²⁸⁶ (S)TEM techniques and electron energy loss spectroscopy

(EELS), in addition to conventional TEM imaging, are important for these studies to maximize resolution and understand chemical evolution.²⁸⁷

While these liquid-cell electrochemistry experiments performed inside the TEM have been groundbreaking, there are many challenges with their implementation and reliable analysis of results. In particular, the interaction of the e-beam with liquids (water or the organic liquids used for Li-ion battery electrolytes) can result in a complex cascade of transport and reaction phenomena.^{288,289} In water, the e-beam can produce molecular and radical products as well as highly reactive solvated electrons.²⁹⁰ In organic liquids, the e-beam can cause electrolyte breakdown or induce electrochemical reactions.²⁷³ While such effects can be useful for active utilization of the e-beam to induce electrochemistry (as discussed in section VI), they must be understood, controlled, and minimized when trying to mimic (or match) conditions within macroscale electrochemical cells. Electrochemical measurements themselves must also be carefully carried out within these cells, as offset potentials due to the e-beam or erroneous potential measurements can occur.²⁹¹ The overarching goal is to directly correlate nanoscale electrochemical dynamics to electrochemical signatures arising from a particular location, and this requires careful cell design and control over experimental conditions.

In this regard, SEM has advantages over (S)TEM for conducting *in situ* experiments, such as the ability to incorporate larger and more complex devices into the vacuum

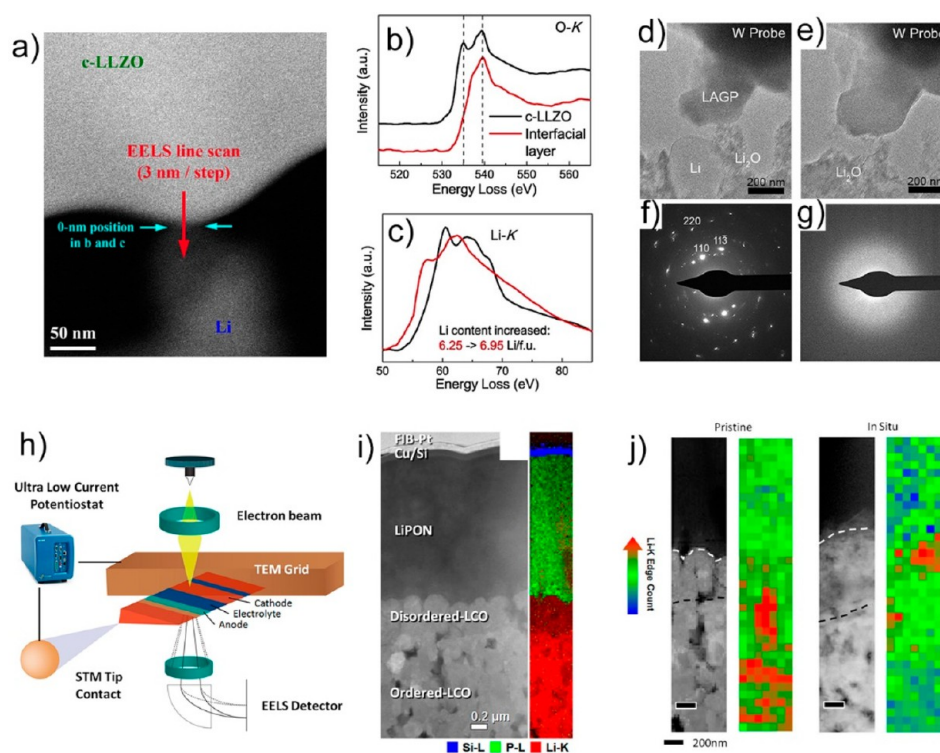


Figure 25. *In situ* (S)TEM of reactions in solid-state batteries. (a) HAADF-STEM image of the edge of a LLZO solid-electrolyte brought into contact with Li metal. (b) EEL spectra (oxygen K-edge) of LLZO in (a) collected from interphase region (red) and bulk LLZO (black). (c) EEL spectra (lithium K-edge) of LLZO in (a) collected from interphase region (red) and bulk LLZO (black). (a–c) Reprinted with permission from ref 322. Copyright 2016 The American Chemical Society. (d–g) Reaction of individual LAGP solid-state electrolyte particle with Li metal showing amorphization. The image and selected-area electron diffraction patterns in (d) and (f) are from before reaction, and those in (e) and (g) are after reaction. (d–g) Reprinted with permission from ref 323. Copyright 2019 The American Chemical Society. (h–j) *In situ* experiment of full solid-state battery cell. (h) Schematic of experimental setup. (i) HAADF-STEM image of thin-film battery stack consisting of LCO, LiPON solid electrolyte, and Si anode. Right frame shows EELS mapping of Si, P, and Li. (j) EELS mapping of Li concentration across this battery in pristine and biased conditions. (h–j) Reprinted with permission from ref 324. Copyright 2016 The American Chemical Society.

chamber and to capture all of the incoming electrons, allowing for quantitative studies of e-beam effects on the electrolyte. A few electrochemical studies report the use of SEM with MEMS/SiN_x-based liquid cells^{292–294} and graphene and graphene oxide membranes^{295–297} as well as open geometries for studying ionic liquid electrolytes²⁹⁸ or all-solid-state Li-ion batteries.^{299,300}

An alternative *in situ* TEM experimental setup that has been successfully used to investigate transformation mechanisms in battery materials down to the atomic scale is the “open-cell” configuration (Figure 24d). In such an experiment, first developed in 2010,³⁰² a TEM holder that allows for mechanical probing and electrical biasing is used. An electrode material is supported on one probe, while a counter electrode (either an alkali metal or alkali-ion-containing material) is fastened to an opposite probe. An ion-conducting phase is present on the surface of one of the materials, and this phase is usually either an ionic liquid electrolyte with very low vapor pressure or the native oxide/nitride of the alkali metal. A bias between ~0.5 and 4 V is then applied between the probes to cause reaction of the active material. While this is obviously different than a real battery (since in most cases the active material is not surrounded by liquid), this experimental setup has been quite successful in enabling direct high-resolution (S)TEM investigation of reaction processes that mimic those in real battery systems.²⁶⁵ Such information has been critical

for understanding how structure, shape, size, and composition of active battery particles affect reaction pathways and chemo-mechanical degradation.^{301,303–307} The downside of such experiments is that it is difficult to correlate electrochemical signatures to reaction processes because the reaction often takes place over a wide and uncontrolled area.

Open-cell *in situ* TEM experiments have been instrumental in uncovering reaction processes in high-capacity alloying and conversion materials, such as silicon, tin, metal sulfides, and other materials.^{301,308–311} The large volume changes in these materials during insertion/extraction of alkali ions often induce significant mechanical damage, and *in situ* TEM has revealed details of reaction front evolution, particle interactions during reaction, and fracture behavior^{301,308,312} (Figure 24e–g). Finite element and density functional theory (DFT) modeling have been important for interpreting such observations, enabling links to be established between the observed structural changes, mechanical stress evolution, and atomic-scale processes^{301,313,314} (Figure 24h). Furthermore, *in situ* TEM and STEM experiments have successfully revealed atomic-scale reaction processes at advancing phase fronts and within materials during Li⁺ insertion,^{304,315} providing unprecedented understanding of fundamental dynamics. Thus, despite some drawbacks, these types of experiments have yielded important knowledge about electrochemical systems.

In recent years, related *in situ* (S)TEM-based techniques have been developed to investigate materials for solid-state batteries as well as the operation of full nanoscale solid-state battery cells. Solid-state batteries have garnered increased attention due to the promise of higher energy density and improved safety compared to Li-ion systems.³¹⁶ However, creating stable and low-impedance interfaces between the solid-state electrolytes and electrode materials remains a significant challenge. Many such interfaces are predicted to be thermodynamically unstable^{317–319} with expected phase evolution over time.³²⁰ Even for stable interfaces, the relationships among the atomic-scale interfacial structure, charge-transfer characteristics, and the potential profile near the interface are not well understood.³²¹ Through the careful fabrication of appropriate cells, *in situ* (S)TEM has the capability to monitor the nano- and atomic-scale structure and chemistry of solid-state battery cells during operation.

Several studies have investigated structural and chemical evolution of a single interface consisting of a solid-state electrolyte in direct contact with lithium metal. EELS in a STEM was used to investigate the interface of the garnet $\text{Li}_{7-3x}\text{Al}_x\text{La}_3\text{Zr}_2\text{O}_{12}$ (LLZO) solid-state electrolyte with lithium³²² (Figure 25a–c). EELS of the oxygen and lithium *K*-edges showed that a near-surface interphase layer formed, which involved the transformation of cubic LLZO to the tetragonal phase during the uptake of Li. This five-unit-cell-thick interphase was shown to be passivating since the underlying cubic LLZO was stable.³²² Other *in situ* TEM work has shown that the reaction of the sodium super ionic conductor (NASICON)-structured $\text{Li}_{1+x}\text{Al}_x\text{Ge}_{2-x}(\text{PO}_4)_3$ (LAGP) solid-electrolyte involves amorphization and volume expansion due to the uptake of a significant amount of Li (Figure 25d–g).³²³ The amorphous phase that results differs from DFT predictions of the thermodynamically stable crystalline phases, suggesting that the interphase could exhibit different properties than expected.

In addition to studies of individual interfaces, several *in situ* investigations have been undertaken on full solid-state battery cells. Such experiments require that the cells be thinned to electron transparency either by using focused ion beam (FIB) techniques or by directly fabricating nanoscale battery cells. Yamamoto *et al.* reported *in situ* results on an operating solid-state cell with a LCO cathode and a glass-ceramic solid-state electrolyte.³²⁵ The authors used electron holography to map the electric potential distribution near the LiCoO_2 /electrolyte interface as a function of applied voltage within the cell and found that the potential profile near the interface depended strongly on the applied voltage. Other work used STEM-EELS to examine the interface between LiCoO_2 and LiPON solid-state electrolyte during charging³²⁴ (Figure 25h–j). A chemical interlayer was observed between these two materials that evolved during charging to form highly oxidized Co species. Another study examined the interface of LiPON-based solid-state cells grown on individual nanowires and showed that self-discharge was significant with LiPON thicknesses below ~ 100 nm.³²⁶ Finally, *in situ* TEM of solid-state batteries has been used to investigate transformations in cathode materials.³²⁷

In situ (S)TEM techniques for the observation of nanoscale electrochemical phenomena have significantly advanced over the past decade and have been used to further our understanding of a wide variety of important processes and reactions in electrochemical systems. Future developments hold great promise toward reliably correlating atomic-level

dynamics with electrochemical signatures. While liquid cells have been instrumental in recording electrochemical data from well-defined nanoscale electrodes,²⁶⁸ further downscaling requires exquisitely sensitive electronics and careful experimentation. Furthermore, the advent of low-dose imaging techniques is expected to be important for atomic-scale imaging of the many electrochemical materials that exhibit instabilities under high-energy electron irradiation,^{328–330} and it may be important for accurate application of potentials. Other techniques such as STEM-based differential phase-contrast imaging may prove to be useful for detecting atomic-level variations in electric fields within electrochemical materials and at interfaces during battery operation.³³¹ Finally, we note that in addition to advances in *in situ* characterization methods, new *ex situ* techniques have recently been developed for accurate atomic-scale characterization of battery materials in their native state, which is a long-standing challenge due to the chemical sensitivity of many electrode materials. In particular, the application of cryo-TEM methods borrowed from the biological sciences has successfully revealed the atomic-scale structure of lithium metal and the SEI layer at the lithium surface.^{332,333}

The Electron Beam as an Active Probe of Electrochemistry. A second opportunity emerging in the context of EM studies of electrochemical processes relates to the use of the e-beam as an active probe, inducing and detecting the electrochemical process (subsequently or in parallel). Signal detection can be based on single pixel signals, including the bright and dark field intensity, EELS signal, or full diffraction patterns (or speckle patterns for less focused beams and amorphous materials). The implementation of the measurement method in this case is similar to SPM, as illustrated in Figure 26. Naturally, of interest is the relationship between the local signal and parameters of the electrochemical process from

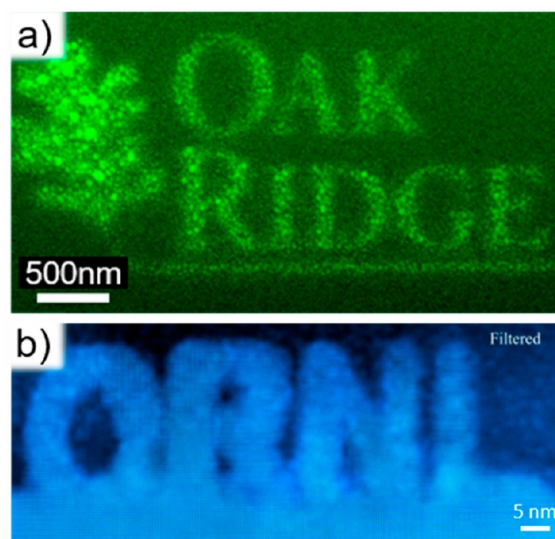


Figure 26. Examples of e-beam-induced material alterations performed in a STEM. (a) “Oak Ridge” nanolithographically patterned with palladium nanocrystals in a liquid cell. Adapted with permission from ref 340. Copyright 2016 The Royal Society of Chemistry. (b) “ORNL” letters epitaxially grown at an amorphous–crystalline SrTiO_3 interface with atomic plane precision through use of a custom e-beam control interface, which controlled scan speed and trajectory. Adapted with permission from ref 341. Copyright 2015 John Wiley and Sons.

atomic to mesoscopic range, for example, nature of local atomic changes, shifts in local electrochemical potentials, size of transformed regions, *etc.*

Alternatively, measurements can be performed in a dynamic mode, alternating high-dose exposure, inducing electrochemical processes, and low-dose imaging. This approach necessitates an increase of the dynamic range of the microscope between the two regimes and can be accomplished *via* the broad adoption of compressed sensing modes and enhanced dynamic range of pixelated detectors.^{334–337} The measurement speed can be further accelerated *via* the introduction of nonrectangular scans that minimize fly back delays of the scanning electronics,³³⁸ which can be further combined with compressive sensing.³³⁹

While the detection of the electrochemical processes induced by the e-beam represents a nontrivial but feasible task and corresponding measurement protocols can be adopted from SPM-based electrochemical studies, the mechanisms of e-beam-induced processes represent a much bigger challenge. Indeed, in SPM the voltage of the tip is well-defined, and while the extreme fields at the tip–surface junction, nanoscale confinement, transport limitations, and IR drops in the adjacent material can all result in unusual chemical processes, these generally can be explained and simulated with existing models.

In comparison, the e-beam is a high-energy probe with the electrons in the 30–300 keV energy range transmitting through the material at a significant fraction of the speed of light. On passage through the material, the electrons collide with the atomic nucleus, transferring a large part of the momentum. For electron energies above the knock-on threshold (*e.g.*, 130 keV for Si), this energy is sufficient to remove the nucleus from the lattice. Alternatively, the energy is dissipated *via* phonons, hot carrier excitation, and electronic transitions. Notably, the knock-on threshold is sensitive to the chemical environment of the atomic species,³⁴² opening a pathway for selective manipulation of atoms with dissimilar bonding.

On transmission through the material, electrons can also inelastically interact with the electronic subsystem. These interactions start at the intrinsic time scale of the electron motion on the order of \sim fs and lead to the formation of athermal electrons and holes in the conductive system and high-level excitations of the core-level electrons. The carriers thermalize, resulting in thermally distributed (but high temperature) carriers that exchange energy with the nucleus system as described by, for example, the two-temperature model.³⁴³ These processes, along with secondary electron emission, can create local nanometer-scale current flows that, in turn, can lead to extremely complex sets of local reactions. Due to the very broad range of energies and time scales from that of an electron to chemical interaction, these are difficult to analyze and predict.

However, a natural question is whether a simplified model for the action of the e-beam can be developed assuming that the nonequilibrium and high-energy processes are concentrated in a small volume and for an external observer these effects can be represented as a defined boundary condition for the current/potential and ionic fluxes.

Theoretical Models of e-Beam-Induced Electrochemical Transformations. Upon electronic excitation, energy barriers that prevent structural rearrangement under equilibrium conditions can be modulated. Indeed, isomerization

processes associated with large free energy barriers in the electronic ground state often become barrierless in certain excited states (Figure 27a).³⁴⁴ Theoretical treatments of the

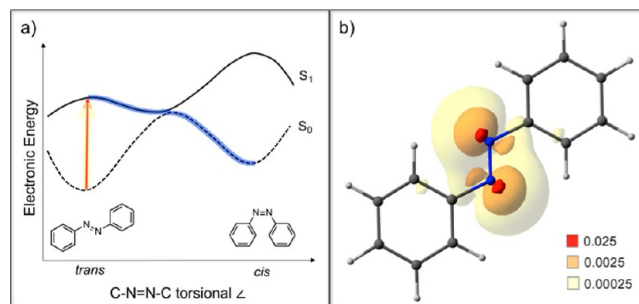


Figure 27. (a) Schematic of potential energy surfaces for ground and first excited electronic states along *cis*–*trans* isomerization coordinate of a canonical photoisomerization compound (azobenzene) with barrierless excited-state isomerization pathway highlighted in blue. (b) Isosurfaces of position-dependent, point charge-induced transition rate (per atomic time unit, indicated by color) to the S₁ ($n \rightarrow \pi^*$) state.

interactions between swift electrons and materials have historically been formulated as a scattering problem expressed in the momentum representation for the incoming electron.³⁴⁵ The resulting inelastic scattering cross sections carry explicit dependence upon the momentum transferred from the incident electron to the material-bound electrons and determine selection rules for electronic excitations of the material. However, the rate of electronic excitation to a particular state of a material can also be evaluated as a function of the e-beam electron's positions in real-space from the vantage of time-dependent electronic structure theory (Figure 27b).³⁴⁶ Transformations of materials, which preserve the number of subatomic particles of each type (isomerizations, phase changes, defect migration, but not necessarily sputtering/milling) may only be facilitated by means of electronic excitations that are themselves number-preserving. It is therefore sufficient to consider just the neutral electronic excitations of the material when investigating the mechanisms underlying this class of transformations. The application of a point-source electric field relieves materials of any periodicity they may otherwise exhibit, so it is reasonable to adopt quantum chemical methods designed for molecular systems, which express electronic states in a finite set of localized basis functions even for nanoscale materials. Along this direction, a real-time, real-space, time-dependent DFT methodology was recently demonstrated for low-energy electron diffraction calculations that include inelastic and multiple scattering effects.³⁴⁷

Clearly, first-principles modeling of the nonequilibrium electronic response of nano- to mesoscale materials to perturbation by localized charges has been enabled to some extent by the development of low-scaling, time-dependent DFT simulation methods. However, the electronic structure of many emerging materials (*e.g.*, graphene nanoribbons) is characterized by strong correlation, for which the single Slater determinant description of electronic states invoked in DFT fails qualitatively.³⁴⁸ While the time evolution of these strongly correlated systems is most tractably approached using Hubbard model Hamiltonians with parameters calculated from first-principles,³⁴⁹ a fully *ab initio* description can (however costly)

also be achieved through the application of multireference electronic structure methods in the time domain.^{350,351}

Even given an electronic structure method that satisfactorily reproduces the electronic states of a material, an accurate description of the perturbation experienced by the system from the passage of a swift electron must also be developed. The evanescent fields emanated by e-beams are ideally suited for exciting spatially localized coherent superpositions of electronic states in materials. While electric dipole selection rules generally provide an adequate description for which electronic transitions are allowed by inelastic electron scattering in the limit of zero momentum transfer from the beam to material,³⁵² the description of finite momentum transfer scattering processes in time-domain simulations requires the full scalar potential of the beam to be included directly in the interaction Hamiltonian. Furthermore, since e-beam electron velocities can be a significant fraction of the speed of light, their associated scalar potential is not necessarily well-approximated by the electrostatic (Coulomb) potential. The Lorentz-invariant retarded potential must be employed in order to capture the “flattening” of the electric field along the e-beam direction that imbues the electronic transition probabilities (like those plotted in Figure 27b) with e-beam energy dependence.

In order to probe the mechanisms of structural reorganization induced in materials by e-beams, one must eventually go beyond just determining which excited states become appreciably populated through inelastic electron scattering in the rest frame of the nuclei. Vibrational (phonon) excitations, which can either be promoted directly through elastic electron–nuclear scattering or manifest due to the disparate forces experienced by nuclei in electronically excited states, must be considered. Electronic and vibrational dynamics are coupled through the electron–nuclei attraction, meaning that high-energy vibrations excited through knock-on processes can lead to an electronic excitation and relaxation from the excited electronic states can precipitate large-amplitude vibrations and isomerization.³⁵³ The latter process, vibrational excitation through nonradiative decay of an excited state population, is implicated in the mechanisms of most optically induced isomerization processes. A proper accounting of all modes of vibrational excitation possible under e-beam irradiation would result from solving the coupled equations of motion for the electronic (both e-beam and material-bound electrons) and vibrational degrees of freedom. Simulation methodologies originally devised to treat the coupled electronic and vibrational evolution of molecular systems thrust out of equilibrium by optical pulses are being appropriated to this end.

Statistical Models for e-Beam Chemistry. The natural question in the context of EM imaging, similar to SPM, is whether it can be used to study the mechanisms of chemical processes on the atomic level, using the e-beam either for visualization or as an active electrode to induce chemical transformations.

In the former case, the answer hinges on the availability of laterally confined chemical devices and the capability of the system to maintain the geometry amenable to atomically resolved studies during imaging. For example, multiple *in situ* studies of the chemical transformations in solid-state batteries and structures have been reported.^{283,302,304,354,355} Similarly, in the last several years reports of *ex situ* studies of atomic-scale transformations during chemical processes are starting to

emerge.^{356,357} However, *in situ* observations of chemical processes can be expected to be challenging and limited to specific material systems where diffusion and reaction do not lead to deviations of the sample geometry from atomic rows being aligned with the e-beam direction. For lateral ion transport, interfacial polarization, and intercalation phenomena, this is generally possible; however, this condition is not likely to be maintained for classical interfacial reactions. Notably, these developments can be assisted by further STEM developments, including 4D STEM³⁵⁸ and depth sectioning with high numerical aperture, corresponding to finite resolution in the beam direction.^{359–363}

The potential impact of such studies is difficult to estimate at this point. Likely it will have significant impact in understanding the details of the electron and ion transfer across interfaces, corresponding to time scales well below the diffusion time constant of the system. This will be assisted by the multiple imaging modalities available in STEM ranging from structural imaging to EELS. The challenge will be to convert the atomic observations into material-specific parameters, as will be further discussed.

Equally exciting, and much easier to realize, are studies of the direct e-beam effects on solids. In the last several years, a large number of e-beam-induced phenomena including ordering of oxygen vacancies,³⁶⁴ formation of vacancies and extended defects in 2D materials,³⁶⁵ beam-induced migration of single interstitials,³⁶⁶ and the formation of individual chemical bonds have been observed. Interestingly, these effects were recently successfully harnessed to control the motion of dopant fronts in bulk Si and to enable the controllable motion and incorporation of single Si atoms in the graphene lattice,^{367–369} leading to controllable formation of di-, tri-, and tetramer Si clusters³⁷⁰ and potentially enabling new classes of atom-by-atom assembly methods.

However, of interest are the mechanisms of these processes, with particularly broad opportunities existing in the context of 2D materials such as graphene, layered chalcogenides, and transition-metal trihalides. In this case, dynamic EM studies enable direct visualization of atomic structure evolution during e-beam-induced transformations, including the formation of individual point defects, their agglomeration, and the formation of an extended defect. For these studies, of particular importance is the development of automated methods for image analysis to extract atomic coordinates, classify individual atoms, trajectories, and point defects and to build a network of chemical transformations.

Correspondingly, the primary challenges in this case can be separated into several groups. One is the fundamental mechanism for e-beam-induced interactions that describes the mechanism of energy transfer from the e-beam to the lattice and the concomitant formation of the point defects. However, it can be argued that the time- and energy-scales of these processes are very different from the subsequent chemical transformations. In this case, the e-beam effect can be represented as a (low) probability of inducing knock-on effects, effectively a local reduction. This concept is equivalent to the effective probe concept for mesoscopic imaging except the chemical volume is reduced to a single atom group, whereas for most electrons, the e-beam is assumed to be not inducing any chemistry effects (*i.e.*, stochastic electrochemical activation). The second is the development of statistical knowledge regarding e-beam-induced interactions, providing a discrete probabilistic equivalent of the radiolysis reaction

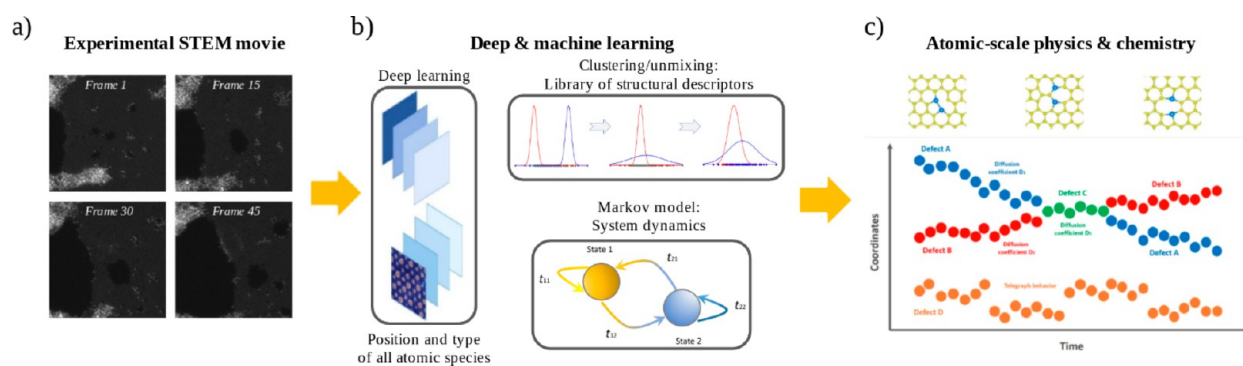


Figure 28. Schematics of workflow for extracting physical and chemical properties of atomic structures and defects from dynamic STEM data. (a) Raw experimental data in the form of a STEM movie is analyzed *via* (b) multiple machine learning techniques including deep learning (more specifically, deep convolutional neural networks) for identifying position and type of all atomic species in each movie frame, clustering/unmixing techniques for constructing libraries of structural descriptors, and Markov state modeling for analyzing system dynamics. (c) In the end, one expects to get information on behavior of individual atomic defects, including diffusion characteristics and transition probabilities. Adapted with permission from refs 382 and 383. Copyright 2019 Springer Nature Publishing.

networks. The third is active feedback, allowing the control of the e-beam-induced reactions to guide them to a desired outcome.

Probing the Mechanisms of e-Beam-Induced Reactions: Feature Extraction. While the observation of e-beam-induced transformations has become relatively common over the last several years, the analysis of the data in terms of reaction dynamics, nature of processes, and underpinning mechanisms remains an issue. Here, we discuss recent insights into the nature of these processes derived with deep learning methods.

In recent years, deep learning, particularly deep convolutional neural networks (DCNNs), has progressed from recognizing videos of cats on the Internet to radiologist-level pneumonia detection and guiding self-driving vehicles. More recently, deep learning models have been utilized in multiple domains of physics and chemistry including the analysis of phase transitions in lattice models,^{371,372} design of novel molecular structures,³⁷³ and the search for new exotic particles in the data collected at the Large Hadron Collider.³⁷⁴ It is now realized that deep learning methods can be adapted for analysis of atom- and molecule-resolved experimental data from EMs and SPMs, including the identification of molecular shapes and orientations on metallic substrates,³⁷⁵ identification of different types of atoms and atomic defects in solids,^{376,377} *in situ* conditioning of a probe,²⁵³ and analysis of solid-state reactions under e-beam irradiation.³⁷⁸

DCNNs represent one of the key examples of a successful application of neuroscientific principles to the field of machine learning.³⁷⁹ DCNN operates on data with grid-structured topology and exploits local connectivity, shared weights, pooling, and the use of many layers for learning from time series data, images (including hyperspectral images), and video data. A typical DCNN model consists of convolutional layers formed by running learnable filters (“convolutional kernels”) of the selected size over the input image (or image in the previous layer) interspersed with pooling layers to produce down-sampled versions of input maps as well as to account for translational invariance. The output of each convolutional layer is “activated” by some nonlinear function such as a rectified linear unit.

Deep learning, and more generally, machine learning, allows for the generalization from the available training examples to produce accurate predictions/classifications on data samples

that were not part of the training set. For the analysis of atomically resolved experimental data, the trained network must be able to return the type and precise location of atoms and/or atomic defects from raw experimental data. The fully convolutional neural networks,³⁸⁰ which can be trained to output pixel-wise classification maps of the same resolution as the input image showing probability of each pixel belonging to a certain type of atom/defect, are ideally suited for this task. The training examples can be produced *via* theoretical simulations of microscopic images such as Multislice³⁸¹ for STEM and DFT or tight binding modeling for STM. If it is not possible to create a training set using simulations, one may perform a manual or semi-manual labeling of the experimental data assuming that it is possible to find and properly label all the features of interest in a pixel-wise manner. A procedure known as data augmentation can be used to solve a potential issue with limited amount of labeled data as well as to account for certain image acquisition parameters such as noise or uncertainty of microscope parameters (*e.g.*, defocusing and aberrations). However, special care must be taken not to introduce any nonphysical features to the images during the augmentation procedure. The data augmentation used in recent works on deep learning for STEM^{376–378} and STM³⁷⁵ involved adding Poisson and Gaussian noise, blurring to account for convolution with a probe, scale jittering, rotations/flipping, shear distortions, and cropping.

The DCNNs have recently enabled studies of solid-state transformations and reactions under e-beam irradiation in dynamic STEM experiments (Figure 28). For this type of experiment, the data sets are usually STEM videos containing several hundred STEM images/frames. In recent work, Ziatdinov *et al.* demonstrated that a DCNN trained on theoretical STEM images can be used to perform an atomic-level “semantic segmentation” of STEM movies and illustrated it using STEM movies of a silicon impurity atom moving at the edge of a graphene nanohole and in bulk graphene.^{376,383} The output of their DCNN was a 4D tensor with dimensions defined as *number of images* × *image height* × *image width* × *number of channels*, where each channel corresponded to a different chemical element (*e.g.*, Si or C; in addition, one channel corresponded to a “background”, which was defined as everything that was not an atom) and each image in a given channel was a set of well-defined (“cleaned”) circular features whose centers corresponded to (*x*, *y*) atomic positions. The

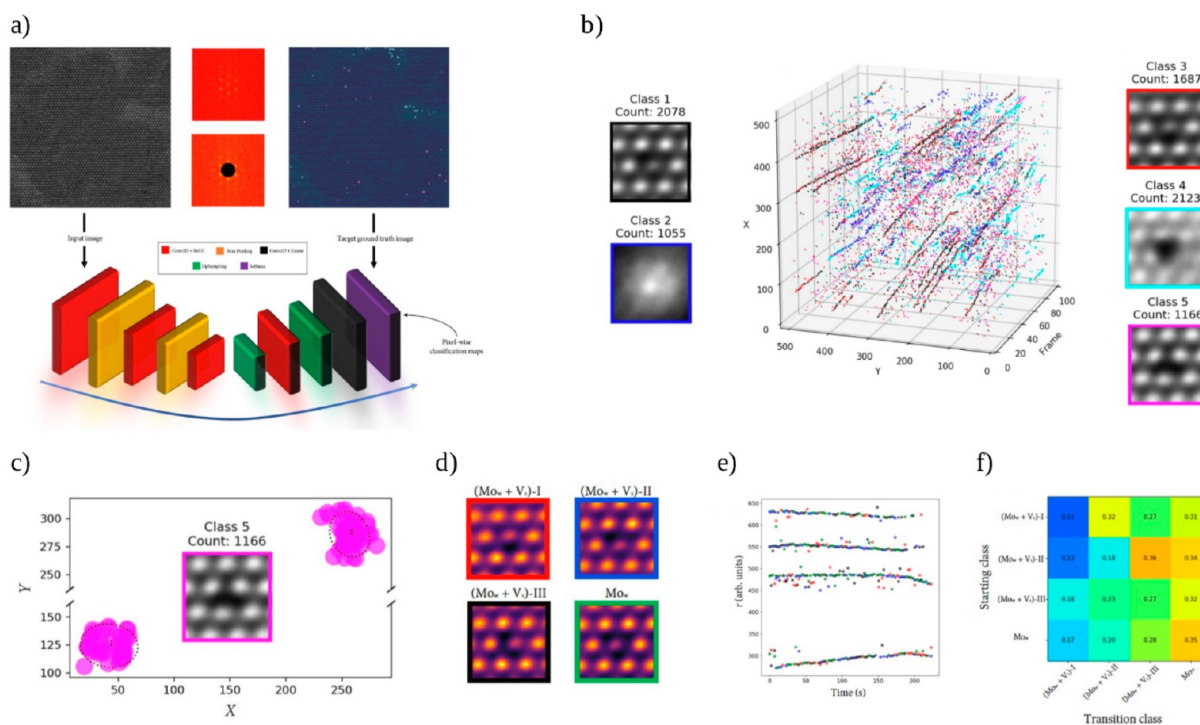


Figure 29. Analysis of defect dynamics from STEM data of WS₂. (a) Creation of a training set for convolutional neural network model using the first frame of STEM movie. (b) Spatiotemporal trajectories of different classes of atomic defects for all movie frames. (c) Selected trajectories for one defect class (S vacancy) collapsed onto x , y plane used to estimate the diffusion coefficient within a simple 2D random walk model. (d–f) Analysis of switching between isolated Mo substitutional defect and Mo coupled with S vacancy (d) along the selected trajectories (e) and associated Markov model transition probabilities (f). Adapted with permission from ref 378. Copyright 2019 Nature Publishing Group.

Gaussian mixture model (GMM) was then applied to a stack of images of individual defects cropped from the DCNN-decoded data to categorize them into different classes/configurations. The number of components in the GMM analysis can be generally estimated with hierarchical clustering, principal component analysis, or Bayesian information criteria. Furthermore, it was shown that the DCNN-GMM results can be further refined using a modified structural similarity search algorithm³⁸⁴ based on prior knowledge of the system's discrete rotational symmetry. Using this approach, the authors found a tendency for the formation of a 1D Si crystal along the zigzag direction of graphene edges as well as for the Si impurity coupling to topological defects in bulk graphene.

In related work, Maksov *et al.*³⁷⁸ used DCNN and GMM to study phase evolution and atomic defect transformations in monolayer WS₂ under 60 kV e-beam irradiation in STEM (Figure 29). To train their DCNN model, the authors exploited the fact that each atomic defect is associated with the violation of ideal periodicity of the lattice. Specifically, they created a training set using a (properly augmented) single frame from a STEM video at the early stage of the e-beam-induced transformation when macroscopic periodicity was still maintained and each defect was easily discovered *via* a standard Fourier-based defect identification approach³⁸⁵ providing the ground truth for network training (Figure 29a). Once trained, the network was able to locate atomic defects in all the movie frames, including frames obtained at the latter stages of the transformation where the global periodicity was no longer maintained. This was possible because the trained network relied solely on local edge properties for identification and was therefore stable toward

the formation of extended defects and fragmentation and rotation of the lattice. Once all the defects were identified by DCNN, they were categorized using the GMM. While the unmixing was performed on image pixels and not on features specific to the atomic structures (bonds, angles, *etc.*), the produced classes did have a very clear correspondence to actual physical defects including defects associated with vacancies in the different (W and S) sublattices and substitutional defects. This combined DCNN-GMM approach allowed us to (re)construct spatiotemporal trajectories for different classes of atomic defects from the experimental STEM movies (Figure 29b) and to analyze properties such as the diffusion coefficients of individual defects (Figure 29c). In addition, Vasudevan *et al.*³⁸⁶ demonstrated that DCNN trained to recognize crystal lattice features, such as a Bravais lattice type in reciprocal space, allows the tracking and determination of the growth rate of larger voids from STEM movies on WS₂.

Libraries of Defects. The enumerated classes of atomic defects extracted from DCNN-GMM analysis of STEM movies can be used to gain insights into the atomistic mechanisms of e-beam-induced transformations *via* the Markov model approach. In this approach, the reaction processes associated with atomic defects are described as memory-less transitions between different states of the system and the transition probabilities determined only by the initial and final states and not by the prior history or surroundings. The matrix of transition probabilities fully describes the system dynamics enabling an analysis of the long-term behavior and presence of dynamic basins. This type of Markov modeling was successfully used to derive transition matrices for coupling between Mo substitutions and S vacancies in WS₂ (Figure

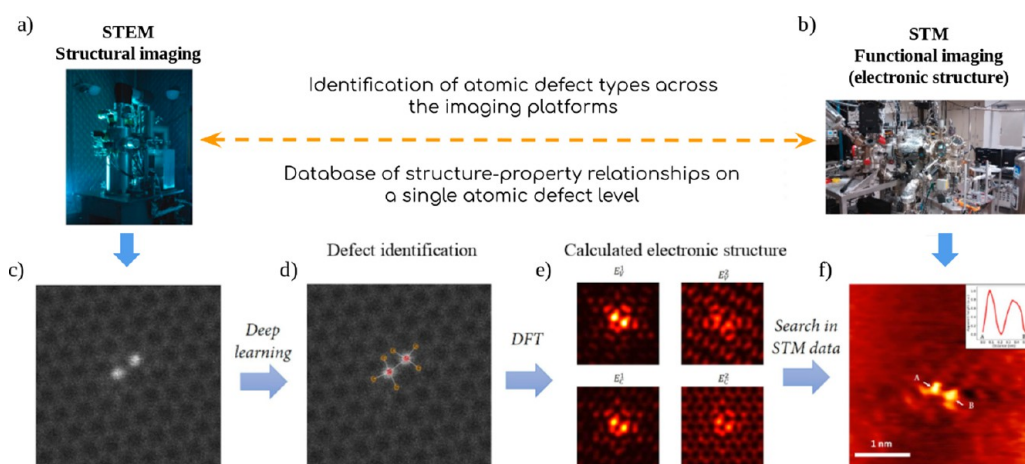


Figure 30. Schematic of workflow for the identification of atomic defects across different imaging platforms. (a) Structural and (b) functional imaging performed with STEM and STM, respectively. (c) Representative STEM image of a Si dimer in graphene. (d) Structure of a Si dimer including its first coordination sphere detected in automated fashion using deep learning and a graphical representation. (e) First-principles calculation of electronic structure of defect identified in (d). (f) STM images proportional to local electronic density of states of defect identified as Si dimer observed in (c, d). Adapted with permission from ref 387. Copyright 2019.

29d–f) and between different Si–C configurations at the edge and in the bulk of graphene. Alternatively, the Markov model can be guided by the first-principles calculations of interaction potentials on the atomic level, enforcing physical constraints to chemical stability and transition probabilities of various atomic and defect configurations, operating both in time (hidden Markov model) and space (hidden Markov random field) domains. In this case, the output of a neural network may be used to populate a state of space with probabilities needed to decode a Markov model and recover results corresponding to a theoretical model. Such a combination of DCNN, Markov model, and first-principles calculations will result in what one can call a ‘physics-guided artificial intelligence (AI)’ for classifying states of solid-state matter from the experimental data.

Structure–Property Relationship on a Single Atomic Defect Level. Learning the structural properties of atomic defects in materials at the atomic-scale from both static and dynamic STEM data provides important insights into the fundamental science behind the solid-state phase transformations and reactions. However, from the application point of view, it is also critical to understand how the observed structural peculiarities affect electronic and magnetic nanoscale functionalities in the systems of interest. One solution is to perform both structural and functional imaging on the same sample. We recall that the well-known method for measuring materials (surface) electronic properties with pm-resolution is STM. For 2D materials, the goal is to identify the same atomic structures and defects from STEM and STM experiments (see Figure 30) and to correlate the observed structural properties to the measured electronic properties, namely, the local density of electronic states at/around the structure of interest. Yet, due to the differences in imaging mechanisms and limitations of the experimental platforms, correlative atomically resolved STEM–STM studies are extremely complex. Recently, Ziatdinov *et al.*³⁸⁷ demonstrated a combined experimental–AI–theoretical approach for extracting and classifying atomic defects from STEM images of graphene with deep neural networks (Figure 30c,d) and performing first-principles calculations to reconstruct the full 3D structure of the extracted defects and explore their electronic structure (Figure 30e). The latter was used to

simulate the STM images, which were then compared to actual STM experimental data (Figure 30f) from the same sample allowing the identification of a three-fold Si impurity in the STM data and a specific Si dimer structure observed by STEM.

Overall, deep learning models trained on theoretically simulated STEM images or on a limited number of labeled experimental data are extremely efficient in extracting atomic/defect coordinates and trajectories and in combination with the standard clustering/unmixing techniques, converting massive volumes of static and dynamic STEM data into structural descriptors. The latter can be mapped on the Markov model, giving rise to the transition probabilities on the single atomic defect level. We expect that in the future there will be more emphasis on incorporating specific physical priors directly into a neural network architecture and/or training procedure. This will include an expansion of the developed deep neural network models, making them “deep and wide” to account for thermodynamic stability of different classes of point and extended structural defects when performing classification of microscopy images and movies obtained under the known experimental conditions (temperature, pressure).

Generative Models with Predictive Power. The computer vision-based tools described above facilitate extraction of the necessary information regarding the atomic-scale structures within images and to compute their statistics. The key is to harness this information and facilitate generative models that can predict properties. This is eminently doable because having access to the statistics of the atomic configurations provides access to the microstates of the system. From this perspective, statistical mechanical models can be formulated to provide an adequate description of the system, which can then be used for predictions of unseen thermodynamic conditions. In other words, just as fluctuation spectroscopy can be used to understand time-dependent correlations in the motion of biomolecules to reproduce the potential landscape,³⁸⁸ in the same way, imaging data can provide access to the states in solid matter. Recently a framework to accomplish this task was put forth by Vlcek *et al.*³⁸⁹ and applied to two distinct experimental systems.^{390,391} The most important questions for this work are (a) the choice

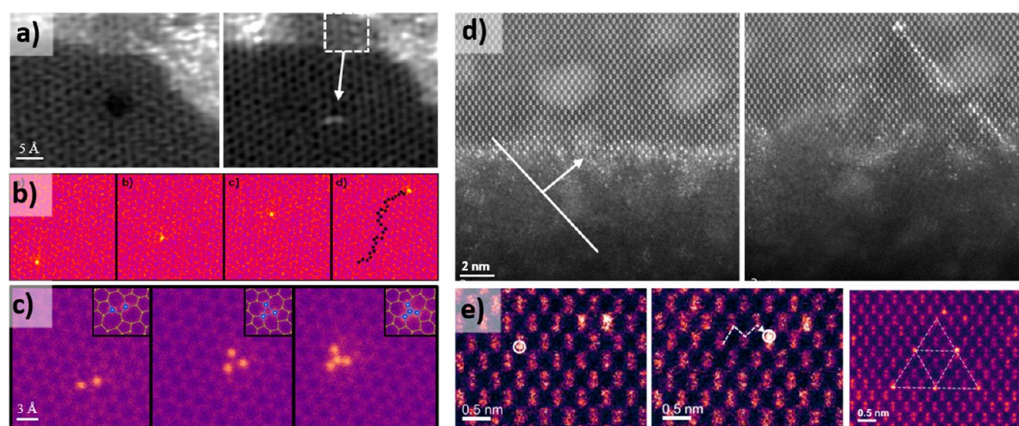


Figure 31. Examples of STEM-based atomic manipulation. (a) Electron beam insertion of Si dopants into a graphene lattice. Here, a 100 kV beam was used to generate a small defect in pristine graphene. Si atoms are sputtered from nearby source material and incorporated into defect as it heals. Reprinted with permission from ref 367. Copyright 2017 AIP Publishing. (b) Si dopants can be moved through the graphene lattice and (c) assembled into primitive structures. Reprinted with permission from ref 370. Copyright 2018 John Wiley & Sons. (d) Feedback-controlled Si crystallization and aggregate movement of Bi dopants within crystal. Reprinted with permission from ref 395. Copyright 2018 IOP Publishing. All rights reserved. (e) Bi dopant movement in a Si crystal revealing mechanism and showing atomic column positioning. Adapted with permission from ref 396. Copyright 2018 The American Chemical Society.

of descriptors and (b) the metric chosen to compare the generative model to the experimental image(s). For the former, the atomic configurations (*i.e.*, nearest-neighbor and possible higher order neighborhood, and potential information on local distortions) provide a reasonable starting point for static data. For the latter, one can think of information theoretic-based metrics such as the Kullback–Liebler divergence, but the appropriate metric of choice is one that respects Boltzmann-type statistics for equilibrium thermodynamic systems. The statistical distance³⁹² is a metric that, when used, can provide a measure of the distance between two thermodynamic systems, effectively computing the distinguishability of samples originating from the generating model and the experiment. When this distance is minimized, the distinguishability is ideally lost and the model can reproduce the features found in the experiment. In addition to providing knowledge on the interaction parameters that directly describe the physics of the system, the model can also be sampled for different thermodynamic conditions, for example, temperature or composition, and thereby facilitate predictive modeling directly from imaging data.

For dynamic data, one can easily extend this framework to incorporate kinetic Monte Carlo modeling and use the experimental data to determine the governing rate constants. In this case, appropriate features would need to be developed, but could include statistics of both simple and more complex events such as adatom diffusion along certain directions or repeated formation/dissociation events. Potentially, the use of a generative adversarial³⁹³ approach could be useful in determining these features automatically, although this must be explored in more detail. Finally, optimized kinetic models enable the scope for training of agents in the simulated environment *via* reinforcement learning³⁹⁴ frameworks, wherein policies can be learned to satisfy a particular goal or target objective in, for example, atomic fabrication.

Atom-by-Atom Fabrication. Numerous experiments in recent years^{397–403} have highlighted the role of e-beam-induced processes for altering materials at the nano- and atomic-scale. Examples range from the creation of monolayer Mo membranes from MoSe₂⁴⁰⁴ to the directed move-

ment^{367,369,405} and assembly^{370,395,396} of single atom structures and from the formation of nanowires⁴⁰⁶ to controlled crystallization.³⁴¹ In each of these cases, the localized e-beam produces environmental conditions sufficiently different from the surrounding area such that energetically unfavorable (in the sense that they would not occur without energy imparted from the beam) chemical transformations can be induced at the atomic scale. Given the many *in situ* sample holders designed to alter environmental parameters (*e.g.*, temperature, electric field, gas, or liquid environment), a STEM chamber has become a chemical reaction chamber with dimensions defined by the e-beam itself. Sample alterations, for example, e-beam damage, have historically been carefully avoided; however, from the electrochemical perspective, the exquisite precision of the STEM offers many untapped opportunities for atomically precise tailoring of materials. This is a clear boon for enhanced understanding of material interactions at the atomic scale where material modifications can be performed and monitored in real time, higher energetic processes are accessible, and specialized holders increase the range of environmental parameters that can be tuned.

Figure 31 highlights a few recent examples of e-beam-induced atomic motion with graphene and Si forming the host lattices. In Figure 31a, Dyck *et al.*³⁶⁷ establish a method for inserting Si dopant atoms into a graphene lattice *in situ* with near lattice site precision. A 100 kV e-beam is positioned over the lattice site of interest until, ideally, a single carbon atom is ejected from the lattice. Subsequent sputtering from adjacent source material, comprised of mostly amorphous carbon and discrete Si atoms, results in Si atoms being scattered across the surface of the graphene lattice. These atoms do not bond strongly to the surface of pristine graphene and are readily moved by the e-beam so that they quickly reattach to the amorphous contaminant material. However, when moving over the defect site, the Si atoms can bond more strongly and become incorporated into the lattice. Figure 31a shows the insertion of a Si dimer into a graphene lattice using this method. Once Si dopants are introduced, they can also be moved with the e-beam. In Figure 31b, Dyck *et al.*³⁷⁰ illustrate the movement of a Si dopant several nanometers with a 60 kV

e-beam and then primitive Si structures embedded in graphene are assembled atom-by-atom (Figure 31c). These experiments indicate there is promise for the fabrication of atomically tailored graphene devices in the STEM. A second set of examples illustrate similar e-beam control of Bi dopants within a Si crystal. Jesse *et al.*³⁹⁵ first show feedback-controlled growth of the crystalline Si phase into an amorphous Si capping layer. They note that the Bi atoms readily move during this crystallization process and show that a dopant front can be created by scanning the beam in a line and advancing it into the Si crystal, depicted schematically by the arrow overlay in Figure 31d. Hudak *et al.*³⁹⁶ performed a more detailed investigation of this phenomenon uncovering the beam-induced mechanisms that govern the Bi movement. Figure 31e illustrates the precise control gained over the Bi atom positioning where the Bi atoms may be directed from one atomic column to the next to create a predefined pattern.

SUMMARY

Functionality of a broad range of materials, devices, and industrial processes, from batteries and fuel cells to information technology devices, electrocatalysts, corrosion, electroactive polymers, molecular machines, and biological systems, is underpinned by an intricate network of spatially separated electrochemical processes. Correspondingly, local probing of electrochemical behaviors on the scale of individual structural elements and inhomogeneities, from grains to defects and even atomic and molecular species, is required to achieve progress in this field.

The classical electrochemical community has generated a wealth of methods and techniques for the macroscopic characterization of electrochemical processes. However, these techniques are generally limited to macroscopically averaged materials responses, where the contributions of individual elements are averaged out, and the crucial elements of reaction mechanisms such as local reaction and nucleation rates and lateral transport of ionic species between reaction sites remain unexplored and undetected. At the same time, extension of these classical electrochemical methods to the nanoscale is generally unrealistic due to both the limitations on detection and sensitivity and confinement effects on reaction mechanisms.

Both SPM and EM techniques can be used for observation of electrochemical reactions, utilizing topographic or functional imaging modalities. In SPM, additional opportunities are opened by the presence of multiple (non-invasive) modes sensitive to electrochemically relevant parameters such as the electrochemical potential. However, nanoscale confinement also enables new imaging modes when the probe becomes an active part of the electrochemical process, both inducing and detecting reactions locally. While the associated mechanisms are often significantly different from the macroscopic analogs since the breaking of local electroneutrality, surface reactions, polarizability, *etc.* become significant, these methods can provide an insight into the local electrochemical functionalities on the nanometer and in special cases the atomic scales.

Similar to SPM, the e-beam in EM techniques can induce local transformations and simultaneously detect the associated changes in imaging and spectroscopic modes. While traditionally these transformations are considered to be undesired beam damage, here we illustrate that these approaches can be harnessed for controllable processes on the nanometer and atomic scale, and furthermore, beam-induced reactions can be

visualized and associated mechanisms can be quantitatively described. On the mesoscale, this typically involves effective concentration and radiolysis models, which are well-developed in the context of radiation chemistry. On the atomic scale, the combination of machine learning and stochastic model matching allows building defect libraries and the quantification of electron-induced transition probabilities, providing discrete analogs to mesoscale descriptions.

We pose that understanding the tip- and e-beam-induced transformations will allow for both the fundamental insights into the reaction mechanisms *via* the statistical descriptions with development of generative models. Observations of atomic scale dynamics will allow for the interference of the nature of the interactions between atomic species. Furthermore, when combined with a real-time feedback, this will enable direct fabrication of matter atom-by-atom, the long-held dream in nanoscience and nanotechnology.

AUTHOR INFORMATION

Corresponding Author

*E-mail: sergei2@ornl.gov.

ORCID

Sergei V. Kalinin: 0000-0001-5354-6152

Ondrej Dyck: 0000-0001-8200-9874

Nina Balke: 0000-0001-5865-5892

Sabine Neumayer: 0000-0002-8167-1230

David Lingerfelt: 0000-0002-5630-0534

Mahshid Ahmadi: 0000-0002-3268-7957

Maxim Ziatdinov: 0000-0003-2570-4592

Matthew T. McDowell: 0000-0001-5552-3456

Evgheni Strelcov: 0000-0002-8561-3847

Notes

The authors declare no competing financial interest.

ACKNOWLEDGMENTS

The writing of this review was supported (S.V.K., O.D., N.B., S.N., W.Y.T., R.V., D.L., M.Z.) by the US Department of Energy Basic Energy Sciences and was performed at the Center for Nanophase Materials Sciences, a U.S. Department of Energy Office of Science User Facility. M.T.M. acknowledges partial support from the National Science Foundation under award no. DMR-1652471 and from an Early Career Faculty grant from NASA's Space Technology Research Grants Program. E.S. acknowledges support under the Cooperative Research Agreement between the University of Maryland and the National Institute of Standards and Technology Center for Nanoscale Science and Technology, award no. 70NANB14H209, through the University of Maryland. M.A. acknowledges support from the University of Tennessee, Knoxville. S.V.K. gratefully acknowledges invitation from H. Tuller and J. Rupp (MIT) to deliver a lecture at the MIT workshop on Frontiers in Electrochemistry (November 2017) which served as an inspiration for this review. The authors express their deep gratitude to Dr. Karren More for careful reading and extensive commenting on this manuscript.

VOCABULARY

Electrochemical, involving the conversion between electrical energy and chemical alterations; **electrochemical strain**, change in molar volume due to electrochemical processes; **electrochemical strain microscopy (ESM)**, an atomic force

microscopy technique where an atomic force microscope is used to detect local expansion/displacement, force and local electrostatic potential, or local current associated with an electrochemical process taking place at the tip–surface junction; **electric double layer (EDL)**, the array of charges and dipoles between two immiscible media when one is a salt solution; (**scanning**) **transmission electron microscopy ((S)TEM)**, used for high-resolution imaging and structural/chemical investigation of materials; **Kelvin probe force microscopy (KPFM)**, a variant of atomic force microscopy where a potential is applied between the probe and sample. This technique can produce work function mapping at the atomic scale; **first-order reversal curve current–voltage spectroscopy (FORC-IV spectroscopy)**, an SPM technique for probing hysteretic electronic conductivity and electrochemical activity by measuring local current–voltage curves in response to a voltage sweep from 0 V to maximum and back to 0 V; **ultramicroelectrode (UME)**, voltammetric working electrode with dimensions of the exposed tip in the micron range and smaller; used for electrochemical in-liquid studies as the scanning probe; **deep convolutional neural network (DCNN)**, an image classification strategy where a trained network is used to output feature classifications without prior knowledge of the image; **Gaussian mixture model (GMM)**, a model description of a data set which represents the data as a sum of gaussians; **Nonadiabatic molecular dynamics**, a class of materials simulations methods designed to predict the coupled electronic and vibrational evolution of materials in response to external perturbations

REFERENCES

- (1) Bagotsky, V. S. *Fuel Cells: Problems and Solutions*. Wiley: Somerset, NJ, 2009.
- (2) Winter, M.; Besenhard, J. O.; Spahr, M. E.; Novak, P. Insertion Electrode Materials for Rechargeable Lithium Batteries. *Adv. Mater.* **1998**, *10*, 725–763.
- (3) Knust, K. N.; Hlushkou, D.; Tallarek, U.; Crooks, R. M. Electrochemical Desalination for a Sustainable Water Future. *ChemElectroChem* **2014**, *1*, 850–857.
- (4) Holade, Y.; Servat, K.; Tingry, S.; Napporn, T. W.; Remita, H.; Cornu, D.; Kokoh, K. B. Advances in Electrocatalysis for Energy Conversion and Synthesis of Organic Molecules. *ChemPhysChem* **2017**, *18*, 2573–2605.
- (5) Waser, R. *Nanoelectronics and Information Technology*, 3rd ed.; Wiley-VCH: Weinheim, Germany, 2012.
- (6) Kalinin, S. V.; Spaldin, N. A. Functional Ion Defects in Transition Metal Oxides. *Science* **2013**, *341*, 858–859.
- (7) Kalinin, S. V.; Borisevich, A.; Fong, D. Beyond Condensed Matter Physics on the Nanoscale: The Role of Ionic and Electrochemical Phenomena in the Physical Functionalities of Oxide Materials. *ACS Nano* **2012**, *6*, 10423–10437.
- (8) Cai, G.; Wang, J.; Lee, P. S. Next-Generation Multifunctional Electrochromic Devices. *Acc. Chem. Res.* **2016**, *49*, 1469–1476.
- (9) Liu, Y.; Flood, A. H.; Bonvallet, P. A.; Vignon, S. A.; Northrop, B. H.; Tseng, H. R.; Jeppesen, J. O.; Huang, T. J.; Brough, B.; Baller, M.; Magonov, S.; Solares, S. D.; Goddard, W. A.; Ho, C. M.; Stoddart, J. F. Linear Artificial Molecular Muscles. *J. Am. Chem. Soc.* **2005**, *127*, 9745–9759.
- (10) Coskun, A.; Banaszak, M.; Astumian, R. D.; Stoddart, J. F.; Grzybowski, B. A. Great Expectations: Can Artificial Molecular Machines Deliver on Their Promise? *Chem. Soc. Rev.* **2012**, *41*, 19–30.
- (11) Mirfakhrai, T.; Madden, J. D. W.; Baughman, R. H. Polymer Artificial Muscles. *Mater. Today* **2007**, *10*, 30–38.
- (12) Kay, E. R.; Leigh, D. A.; Zerbetto, F. Synthetic Molecular Motors and Mechanical Machines. *Angew. Chem., Int. Ed.* **2007**, *46*, 72–191.
- (13) Saha, S.; Stoddart, J. F. Photo-Driven Molecular Devices. *Chem. Soc. Rev.* **2007**, *36*, 77–92.
- (14) Browne, W. R.; Feringa, B. L. Making Molecular Machines Work. *Nat. Nanotechnol.* **2006**, *1*, 25–35.
- (15) Fletcher, S. P.; Dumur, F.; Pollard, M. M.; Feringa, B. L. A Reversible, Unidirectional Molecular Rotary Motor Driven by Chemical Energy. *Science* **2005**, *310*, 80–82.
- (16) Adler, S. B. Factors Governing Oxygen Reduction in Solid Oxide Fuel Cell Cathodes. *Chem. Rev.* **2004**, *104*, 4791–4843.
- (17) Glinchuk, M. D.; Stephanovich, V. A. Theory of the Nonlinear Susceptibility of Relaxor Ferroelectrics. *J. Phys.: Condens. Matter* **1998**, *10*, 11081–11094.
- (18) Westphal, V.; Kleemann, W.; Glinchuk, M. D. Diffuse Phase Transitions and Random-Field-Induced Domain States of the Relaxor Ferroelectric $\text{PbMg}_{1/3}\text{Nb}_{2/3}\text{O}_3$. *Phys. Rev. Lett.* **1992**, *68*, 847–850.
- (19) Dai, X. H.; Xu, Z.; Viehland, D. Long-Time Relaxation from Relaxor to Normal Ferroelectric States in $\text{Pb}_{0.91}\text{La}_{0.06}(\text{Zr}_{0.65}\text{Ti}_{0.35})\text{O}_3$. *J. Am. Ceram. Soc.* **1996**, *79*, 1957–1960.
- (20) Glazounov, A. E.; Tagantsev, A. K.; Bell, A. J. Evidence for Domain-Type Dynamics in the Ergodic Phase of the $\text{PbMg}_{1/3}\text{Nb}_{2/3}\text{O}_3$ Relaxor Ferroelectric. *Phys. Rev. B: Condens. Matter Mater. Phys.* **1996**, *53*, 11281–11284.
- (21) Dagotto, E.; Hotta, T.; Moreo, A. Colossal Magnetoresistant Materials: The Key Role of Phase Separation. *Phys. Rep.* **2001**, *344*, 1–153.
- (22) Tokura, Y. Critical Features of Colossal Magnetoresistive Manganites. *Rep. Prog. Phys.* **2006**, *69*, 797–851.
- (23) Xu, Z.; Kim, M. C.; Li, J. F.; Viehland, D. Observation of a Sequence of Domain-Like States with Increasing Disorder in Ferroelectrics. *Philos. Mag. A* **1996**, *74*, 395–406.
- (24) Dai, X. H.; Xu, Z.; Viehland, D. Normal to Relaxor Ferroelectric Transformations in Lanthanum-Modified Tetragonal-Structured Lead Zirconate Titanate Ceramics. *J. Appl. Phys.* **1996**, *79*, 1021–1026.
- (25) Kholkin, A.; Morozovska, A.; Kiselev, D.; Bdkin, I.; Rodriguez, B.; Wu, P. P.; Bokov, A.; Ye, Z. G.; Dkhil, B.; Chen, L. Q.; Kosec, M.; Kalinin, S. V. Surface Domain Structures and Mesoscopic Phase Transition in Relaxor Ferroelectrics. *Adv. Funct. Mater.* **2011**, *21*, 1977–1987.
- (26) Morozovska, A. N.; Eliseev, E. A.; Kurchak, A. I.; Morozovsky, N. V.; Vasudevan, R. K.; Strikha, M. V.; Kalinin, S. V. Effect of Surface Ion Screening on the Polarization Reversal Scenario in Ferroelectric Thin Films: Crossover From Ferroionic to Antiferroionic States. *Phys. Rev. B: Condens. Matter Mater. Phys.* **2017**, *96*, 245405.
- (27) Morozovska, A. N.; Eliseev, E. A.; Morozovsky, N. V.; Kalinin, S. V. Piezoresponse of Ferroelectric Films in Ferroionic States: Time and Voltage Dynamics. *Appl. Phys. Lett.* **2017**, *110*, 182907.
- (28) Morozovska, A. N.; Eliseev, E. A.; Morozovsky, N. V.; Kalinin, S. V. Ferroionic States in Ferroelectric Thin Films. *Phys. Rev. B: Condens. Matter Mater. Phys.* **2017**, *95*, 195413.
- (29) Ahmadi, M.; Collins, L.; Puzos, A.; Zhang, J.; Keum, J. K.; Lu, W.; Ivanov, I.; Kalinin, S. V.; Hu, B. Exploring Anomalous Polarization Dynamics in Organometallic Halide Perovskites. *Adv. Mater.* **2018**, *30*, 1705298.
- (30) Strelcov, E.; Yang, S. M.; Jesse, S.; Balke, N.; Vasudevan, R. K.; Kalinin, S. V. Solid-State Electrochemistry on the Nanometer and Atomic Scales: the Scanning Probe Microscopy Approach. *Nanoscale* **2016**, *8*, 13838–13858.
- (31) Oja, S. M.; Wood, M.; Zhang, B. Nanoscale Electrochemistry. *Anal. Chem.* **2013**, *85*, 473–486.
- (32) Maier, J. Pushing Nanoionics to the Limits: Charge Carrier Chemistry in Extremely Small Systems. *Chem. Mater.* **2014**, *26*, 348–360.
- (33) Machta, B. B.; Chachra, R.; Transtrum, M. K.; Sethna, J. P. Parameter Space Compression Underlies Emergent Theories and Predictive Models. *Science* **2013**, *342*, 604–607.

- (34) Aurbach, D. Review of Selected Electrode-Solution Interactions Which Determine the Performance of Li and Li Ion Batteries. *J. Power Sources* **2000**, *89*, 206–218.
- (35) Mayergoyz, I. D.; Friedman, G. Generalized Preisach Model of Hysteresis. *IEEE Trans. Magn.* **1988**, *24*, 212–217.
- (36) Mayergoyz, I. D. Mathematical-Models of Hysteresis. *Phys. Rev. Lett.* **1986**, *56*, 1518–1521.
- (37) Mitchler, P. D.; Roshko, R. M.; Dahlberg, E. D. A Preisach Model With a Temperature and Time-Dependent Remanance Maximum. *J. Appl. Phys.* **1997**, *81*, 5221–5223.
- (38) Hall, D. A. Review Nonlinearity in Piezoelectric Ceramics. *J. Mater. Sci.* **2001**, *36*, 4575–4601.
- (39) Robert, G.; Damjanovic, D.; Setter, N.; Turik, A. V. Preisach Modeling of Piezoelectric Nonlinearity in Ferroelectric Ceramics. *J. Appl. Phys.* **2001**, *89*, 5067–5074.
- (40) Song, T.; Roshko, R. M.; Dahlberg, E. D. Modelling the Irreversible Response of Magnetically Ordered Materials: a Preisach-Based Approach. *J. Phys.: Condens. Matter* **2001**, *13*, 3443–3460.
- (41) Roberts, A. P.; Pike, C. R.; Verosub, K. L. First-Order Reversal Curve Diagrams: a New Tool for Characterizing the Magnetic Properties of Natural Samples. *J. Geophys. Res.* **2000**, *105*, 28461–28475.
- (42) Pierce, M. S.; Buechler, C. R.; Sorensen, L. B.; Kevan, S. D.; Jagla, E. A.; Deutsch, J. M.; Mai, T.; Narayan, O.; Davies, J. E.; Liu, K.; Zimanyi, G. T.; Katzgraber, H. G.; Hellwig, O.; Fullerton, E. E.; Fischer, P.; Kortright, J. B. Disorder-Induced Magnetic Memory: Experiments and Theories. *Phys. Rev. B: Condens. Matter Mater. Phys.* **2007**, *75*, 144406.
- (43) Katzgraber, H. G.; Friedman, G.; Zimanyi, G. T. Fingerprinting Hysteresis. *Phys. B* **2004**, *343*, 10–14.
- (44) Young, R.; Ward, J.; Scire, F. The Topografiner: An Instrument for Measuring Surface Microtopography. *Rev. Sci. Instrum.* **1972**, *43*, 999–1011.
- (45) Binnig, G.; Rohrer, H.; Gerber, C.; Weibel, E. 7×7 Reconstruction on Si(111) Resolved in Real Space. *Phys. Rev. Lett.* **1983**, *50*, 120–123.
- (46) Binnig, G.; Rohrer, H. Scanning Tunneling Microscopy. *Helv. Phys. Acta* **1982**, *55*, 726–735.
- (47) Aurbach, D.; Cohen, Y. The Application of Atomic Force Microscopy for the Study of Li Deposition Processes. *J. Electrochem. Soc.* **1996**, *143*, 3525–3532.
- (48) Aurbach, D.; Cohen, Y. Morphological Studies of Li Deposition Processes in LiAsF₆/PC Solutions by *in Situ* Atomic Force Microscopy. *J. Electrochem. Soc.* **1997**, *144*, 3355–3360.
- (49) Swiatowska-Mrowlecka, J.; Maurice, V.; Klein, L.; Marcus, P. Nanostructural Modifications of V₂O₅ Thin Films During Li Intercalation Studied *in Situ* by AFM. *Electrochem. Commun.* **2007**, *9*, 2448–2455.
- (50) Shen, C.; Wang, S.; Jin, Y.; Han, W.-Q. *In Situ* AFM Imaging of Solid Electrolyte Interfaces on HOPG with Ethylene Carbonate and Fluoroethylene Carbonate-Based Electrolytes. *ACS Appl. Mater. Interfaces* **2015**, *7*, 25441–25447.
- (51) Binnig, G.; Quate, C. F.; Gerber, C. Atomic Force Microscope. *Phys. Rev. Lett.* **1986**, *56*, 930–933.
- (52) Hirsekorn, S.; Rabe, U.; Arnold, W. Theoretical Description of the Transfer of Vibrations from a Sample to the Cantilever of an Atomic Force Microscope. *Nanotechnology* **1997**, *8*, 57–66.
- (53) Rabe, U.; Janser, K.; Arnold, W. Vibrations of Free And Surface-Coupled Atomic Force Microscope Cantilevers: Theory and Experiment. *Rev. Sci. Instrum.* **1996**, *67*, 3281–3293.
- (54) Rabe, U.; Arnold, W. Acoustic Microscopy by Atomic-Force Microscopy. *Appl. Phys. Lett.* **1994**, *64*, 1493–1495.
- (55) Gruverman, A. L.; Hatano, J.; Tokumoto, H. Scanning Force Microscopy Studies of Domain Structure in BaTiO₃ Single Crystals. *Japanese Journal of Applied Physics Part 1-Regular Papers Short Notes & Review Papers* **1997**, *36*, 2207–2211.
- (56) Kalinin, S. V.; Setter, N.; Kholkin, A. L. Electromechanics on the Nanometer Scale: Emerging Phenomena, Devices, and Applications. *MRS Bull.* **2009**, *34*, 634–642.
- (57) Balke, N.; Bdikin, I.; Kalinin, S. V.; Kholkin, A. L. Electromechanical Imaging and Spectroscopy of Ferroelectric and Piezoelectric Materials: State of the Art and Prospects for the Future. *J. Am. Ceram. Soc.* **2009**, *92*, 1629–1647.
- (58) Jones, A. C.; Berweiger, S.; Wei, J.; Cobden, D.; Raschke, M. B. Nano-Optical Investigations of the Metal-Insulator Phase Behavior of Individual VO₂ Microcrystals. *Nano Lett.* **2010**, *10*, 1574–1581.
- (59) Tanimoto, M.; Vatel, O. Kelvin Probe Force Microscopy for Characterization of Semiconductor Devices and Processes. *J. Vac. Sci. Technol., B: Microelectron. Process. Phenom.* **1996**, *14*, 1547–1551.
- (60) Vatel, O.; Tanimoto, M. Kelvin Probe Force Microscopy for Potential Distribution Measurement of Semiconductor-Device. *J. Appl. Phys.* **1995**, *77*, 2358–2362.
- (61) Grutter, P.; Liu, Y.; LeBlanc, P.; Durig, U. Magnetic Dissipation Force Microscopy. *Appl. Phys. Lett.* **1997**, *71*, 279–281.
- (62) Albrecht, T. R.; Grutter, P.; Horne, D.; Rugar, D. Frequency-Modulation Detection Using High-Q Cantilevers for Enhanced Force Microscope Sensitivity. *J. Appl. Phys.* **1991**, *69*, 668–673.
- (63) Martin, Y.; Wickramasinghe, H. K. Magnetic Imaging by Force Microscopy With 1000-Å Resolution. *Appl. Phys. Lett.* **1987**, *50*, 1455–1457.
- (64) Jesse, S.; Guo, S.; Kumar, A.; Rodriguez, B. J.; Proksch, R.; Kalinin, S. V. Resolution Theory, and Static and Frequency-Dependent Cross-Talk in Piezoresponse Force Microscopy. *Nanotechnology* **2010**, *21*, 405703.
- (65) Vasudevan, R. K.; Balke, N.; Maksymovych, P.; Jesse, S.; Kalinin, S. V. Ferroelectric or Non-Ferroelectric: Why so Many Materials Exhibit "Ferroelectricity" on the Nanoscale. *Appl. Phys. Rev.* **2017**, *4*, 021302.
- (66) Adler, S. B. Chemical Expansivity of Electrochemical Ceramics. *J. Am. Ceram. Soc.* **2001**, *84*, 2117–2119.
- (67) Bishop, S. R.; Duncan, K. L.; Wachsmann, E. D. Surface and Bulk Defect Equilibria in Strontium-Doped Lanthanum Cobalt Iron Oxide. *J. Electrochem. Soc.* **2009**, *156*, B1242–B1248.
- (68) Morozovska, A. N.; Eliseev, E. A.; Kalinin, S. V. Electro-mechanical Probing of Ionic Currents in Energy Storage Materials. *Appl. Phys. Lett.* **2010**, *96*, 222906.
- (69) Stoklosa, A.; Laskowska, B. Molar Volume and Composition of Oxides of the Same Metal. *J. Chem. Crystallogr.* **2008**, *38*, 279–284.
- (70) Amatucci, G. G.; Tarascon, J. M.; Klein, L. C. CoO₂, the End Member of the Li_xCoO₂ Solid Solution. *J. Electrochem. Soc.* **1996**, *143*, 1114–1123.
- (71) Kalinin, S.; Kumar, A.; Balke, N.; McCorkle, M.; Guo, S. L.; Arruda, T.; Jesse, S. ESM of Ionic and Electrochemical Phenomena on the Nanoscale. *Adv. Mater. Processes* **2011**, *169*, 30–34.
- (72) Jesse, S.; Kalinin, S. V.; Proksch, R.; Baddorf, A. P.; Rodriguez, B. J. The Band Excitation Method in Scanning Probe Microscopy for Rapid Mapping of Energy Dissipation on the Nanoscale. *Nanotechnology* **2007**, *18*, 435503.
- (73) Jesse, S.; Vasudevan, R. K.; Collins, L.; Strelcov, E.; Okatan, M. B.; Belianinov, A.; Baddorf, A. P.; Proksch, R.; Kalinin, S. V. Band Excitation in Scanning Probe Microscopy: Recognition and Functional Imaging. *Annu. Rev. Phys. Chem.* **2014**, *65*, 519–536.
- (74) Jesse, S.; Kalinin, S. V. Band Excitation in Scanning Probe Microscopy: Sines of Change. *J. Phys. D: Appl. Phys.* **2011**, *44*, 464006.
- (75) Rodriguez, B. J.; Callahan, C.; Kalinin, S. V.; Proksch, R. Dual-Frequency Resonance-Tracking Atomic Force Microscopy. *Nanotechnology* **2007**, *18*, 475504.
- (76) Balke, N.; Jesse, S.; Morozovska, A. N.; Eliseev, E.; Chung, D. W.; Kim, Y.; Adamczyk, L.; Garcia, R. E.; Dudney, N.; Kalinin, S. V. Nanoscale Mapping of ion Diffusion in a Lithium-Ion Battery Cathode. *Nat. Nanotechnol.* **2010**, *5*, 749–754.
- (77) Bates, J. B.; Dudney, N. J.; Neudecker, B. J.; Hart, F. X.; Jun, H. P.; Hackney, S. A. Preferred Orientation of Polycrystalline LiCoO₂ Films. *J. Electrochem. Soc.* **2000**, *147*, 59–70.
- (78) Balke, N.; Kalnaus, S.; Dudney, N. J.; Daniel, C.; Jesse, S.; Kalinin, S. V. Local Detection of Activation Energy for Ionic Transport in Lithium Cobalt Oxide. *Nano Lett.* **2012**, *12*, 3399–403.

- (79) Okubo, M.; Tanaka, Y.; Zhou, H.; Kudo, T.; Honma, I. Determination of Activation Energy for Li Ion Diffusion in Electrodes. *J. Phys. Chem. B* **2009**, *113*, 2840–2847.
- (80) Van der Ven, A.; Ceder, G. Lithium Diffusion Mechanisms in Layered Intercalation Compounds. *J. Power Sources* **2001**, *97*–98, 529–531.
- (81) Arruda, T. M.; Kumar, A.; Kalinin, S. V.; Jesse, S. Mapping Irreversible Electrochemical Processes on the Nanoscale: Ionic Phenomena in Li Ion Conductive Glass Ceramics. *Nano Lett.* **2011**, *11*, 4161–4167.
- (82) Arruda, T. M.; Kumar, A.; Kalinin, S. V.; Jesse, S. The Partially Reversible Formation of Li-Metal Particles on a Solid Li Electrolyte: Applications Toward Nanobatteries. *Nanotechnology* **2012**, *23*, 325402.
- (83) Morozovska, A. N.; Eliseev, E. A.; Balke, N.; Kalinin, S. V. Local Probing of Ionic Diffusion by Electrochemical Strain Microscopy: Spatial Resolution and Signal Formation Mechanisms. *J. Appl. Phys.* **2010**, *108*, 053712.
- (84) Kumar, A.; Ciucci, F.; Morozovska, A. N.; Kalinin, S. V.; Jesse, S. Measuring Oxygen Reduction/Evolution Reactions on the Nanoscale. *Nat. Chem.* **2011**, *3*, 707–713.
- (85) Balke, N.; Maksymovych, P.; Jesse, S.; Herklotz, A.; Tselev, A.; Eom, C.-B.; Kravchenko, I. I.; Yu, P.; Kalinin, S. V. Differentiating Ferroelectric and Nonferroelectric Electromechanical Effects with Scanning Probe Microscopy. *ACS Nano* **2015**, *9*, 6484–6492.
- (86) Balke, N.; Maksymovych, P.; Jesse, S.; Kravchenko, I. I.; Li, Q.; Kalinin, S. V. Exploring Local Electrostatic Effects with Scanning Probe Microscopy: Implications for Piezoresponse Force Microscopy and Triboelectricity. *ACS Nano* **2014**, *8*, 10229–10236.
- (87) Kumar, A.; Arruda, T. M.; Kim, Y.; Ivanov, I. N.; Jesse, S.; Bark, C. W.; Bristowe, N. C.; Artacho, E.; Littlewood, P. B.; Eom, C. B.; Kalinin, S. V. Probing Surface and Bulk Electrochemical Processes on the LaAlO₃-SrTiO₃ Interface. *ACS Nano* **2012**, *6*, 3841–3852.
- (88) Valov, I.; Sapezanskaia, I.; Nayak, A.; Tsuruoka, T.; Bredow, T.; Hasegawa, T.; Staikov, G.; Aono, M.; Waser, R. Atomically Controlled Electrochemical Nucleation at Superionic Solid Electrolyte Surfaces. *Nat. Mater.* **2012**, *11*, 530–535.
- (89) Lushta, V.; Dietzel, D.; Roling, B.; Schirmeisen, A. Nanoscale Characterization of Ion Mobility by Temperature-Controlled Li-Nanoparticle Growth. *ACS Appl. Mater. Interfaces* **2019**, *11*, 5476–5483.
- (90) Yang, S. M.; Strelcov, E.; Paranthaman, M. P.; Tselev, A.; Noh, T. W.; Kalinin, S. V. Humidity Effect on Nanoscale Electrochemistry in Solid Silver Ion Conductors and the Dual Nature of Its Locality. *Nano Lett.* **2015**, *15*, 1062–1069.
- (91) Zhao, W.; Bi, S.; Balke, N.; Rack, P. D.; Ward, T. Z.; Kalinin, S. V.; Dai, S.; Feng, G. Understanding Electric Double-Layer Gating Based on Ionic Liquids: from Nanoscale to Macroscale. *ACS Appl. Mater. Interfaces* **2018**, *10*, 43211–43218.
- (92) Barna, S. F.; Jacobs, K. E.; Mensing, G. A.; Ferreira, P. M. Electrochemical Direct Writing and Erasing of Silver Nanostructures on Phosphate Glass Using Atomic Force Microscopy. *Nanotechnology* **2017**, *28*, 065301–8.
- (93) Sader, J. E.; Chon, J. W. M.; Mulvaney, P. Calibration of Rectangular Atomic Force Microscope Cantilevers. *Rev. Sci. Instrum.* **1999**, *70*, 3967–3969.
- (94) Sader, J. E.; Larson, I.; Mulvaney, P.; White, L. R. Method for the Calibration of Atomic Force Microscope Cantilevers. *Rev. Sci. Instrum.* **1995**, *66*, 3789–3798.
- (95) Lübke, J.; Temmen, M.; Rahe, P.; Kühnle, A.; Reichling, M. Determining Cantilever Stiffness From Thermal Noise. *Beilstein J. Nanotechnol.* **2013**, *4*, 227–233.
- (96) Hutter, J. L.; Bechhoefer, J. Calibration of Atomic-Force Microscope Tips. *Rev. Sci. Instrum.* **1993**, *64*, 1868–1873.
- (97) Balke, N.; Jesse, S.; Yu, P.; Ben, C.; Kalinin, S. V.; Tselev, A. Quantification of Surface Displacements and Electromechanical Phenomena via Dynamic Atomic Force Microscopy. *Nanotechnology* **2016**, *27*, 425707.
- (98) Labuda, A.; Proksch, R. Quantitative Measurements of Electrochemical Response With a Combined Optical Beam and Interferometric Atomic Force Microscope. *Appl. Phys. Lett.* **2015**, *106*, 253103–5.
- (99) Morozovska, A. N.; Eliseev, E. A.; Kalinin, S. V. Domain Nucleation and Hysteresis Loop Shape in Piezoresponse Force Spectroscopy. *Appl. Phys. Lett.* **2006**, *89*, 192901.
- (100) Eliseev, E. A.; Morozovska, A. N.; Ievlev, A. V.; Balke, N.; Maksymovych, P.; Tselev, A.; Kalinin, S. V. Electrostrictive and Electrostatic Responses in Contact Mode Voltage Modulated Scanning Probe Microscopies. *Appl. Phys. Lett.* **2014**, *104*, 232901.
- (101) Morozovska, A. N.; Eliseev, E. A.; Bravina, S. L.; Ciucci, F.; Svechnikov, G. S.; Chen, L. Q.; Kalinin, S. V. Frequency Dependent Dynamical Electromechanical Response of Mixed Ionic-Electronic Conductors. *J. Appl. Phys.* **2012**, *111*, 014107.
- (102) Morozovska, A. N.; Eliseev, E. A.; Kalinin, S. V. Electrochemical Strain Microscopy with Blocking Electrodes: The Role of Electromigration and Diffusion. *J. Appl. Phys.* **2012**, *111*, 014114.
- (103) Lim, J.; Li, Y.; Alsem, D. H.; So, H.; Lee, S. C.; Bai, P.; Cogswell, D. A.; Liu, X.; Jin, N.; Yu, Y.-s.; Salmon, N. J.; Shapiro, D. A.; Bazant, M. Z.; Tyliczszak, T.; Chueh, W. C. Origin and Hysteresis of Lithium Compositional Spatiodynamics within Battery Primary Particles. *Science* **2016**, *353*, 566–571.
- (104) Kuppan, S.; Xu, Y.; Liu, Y.; Chen, G. Phase Transformation Mechanism in Lithium Manganese Nickel Oxide Revealed by Single-Crystal Hard X-Ray Microscopy. *Nat. Commun.* **2017**, *8*, 14309.
- (105) Wolf, M.; May, B. M.; Cabana, J. Visualization of Electrochemical Reactions in Battery Materials with X-ray Microscopy and Mapping. *Chem. Mater.* **2017**, *29*, 3347–3362.
- (106) Bak, S.-M.; Shadike, Z.; Lin, R.; Yu, X.; Yang, X.-Q. *In Situ/Operando* Synchrotron-Based X-Ray Techniques for Lithium-Ion Battery Research. *NPG Asia Mater.* **2018**, *10*, 563–580.
- (107) Dong, C.-L.; Vayssieres, L. *In Situ/Operando* X-ray Spectroscopies for Advanced Investigation of Energy Materials. *Chem. - Eur. J.* **2018**, *24*, 18356–18373.
- (108) Tripathi, A. M.; Su, W.-N.; Hwang, B. J. *In Situ* Analytical Techniques for Battery Interface Analysis. *Chem. Soc. Rev.* **2018**, *47*, 736–851.
- (109) Maurin, G.; Bousquet, C.; Henn, F.; Bernier, P.; Almairac, R.; Simon, B. Electrochemical Lithium Intercalation into Multiwall Carbon Nanotubes: A micro-Raman Study. *Solid State Ionics* **2000**, *136–137*, 1295–1299.
- (110) Baddour-Hadjean, R.; Pereira-Ramos, J.-P. Raman Microspectrometry Applied to the Study of Electrode Materials for Lithium Batteries. *Chem. Rev.* **2010**, *110*, 1278–1319.
- (111) Sole, C.; Drewett, N. E.; Hardwick, L. J. *In Situ* Raman Study of Lithium-Ion Intercalation into Microcrystalline Graphite. *Faraday Discuss.* **2014**, *172*, 223–237.
- (112) Ievlev, A. V.; Brown, C.; Burch, M. J.; Agar, J. C.; Velarde, G. A.; Martin, L. W.; Maksymovych, P.; Kalinin, S. V.; Ovchinnikova, O. S. Chemical Phenomena of Atomic Force Microscopy Scanning. *Anal. Chem.* **2018**, *90*, 3475–3481.
- (113) Lindgren, G.; Ievlev, A.; Jesse, S.; Ovchinnikova, O. S.; Kalinin, S. V.; Vasudevan, R. K.; Canalias, C. Elasticity Modulation Due to Polarization Reversal and Ionic Motion in the Ferroelectric Superionic Conductor KTiOPO₄. *ACS Appl. Mater. Interfaces* **2018**, *10*, 32298–32303.
- (114) Neumayer, S. M.; Ievlev, A. V.; Collins, L.; Vasudevan, R.; Baghban, M. A.; Ovchinnikova, O.; Jesse, S.; Gallo, K.; Rodriguez, B. J.; Kalinin, S. V. Surface Chemistry Controls Anomalous Ferroelectric Behavior in Lithium Niobate. *ACS Appl. Mater. Interfaces* **2018**, *10*, 29153–29160.
- (115) Liu, Y. T.; Collins, L.; Proksch, R.; Kim, S.; Watson, B. R.; Doughty, B.; Calhoun, T. R.; Ahmadi, M.; Ievlev, A. V.; Jesse, S.; Retterer, S. T.; Belianinov, A.; Xiao, K.; Huang, J. S.; Sumpter, B. G.; Kalinin, S. V.; Hu, B.; Ovchinnikova, O. S. Chemical Nature of Ferroelastic Twin Domains in CH₃NH₃PbI₃ Perovskite. *Nat. Mater.* **2018**, *17*, 1013–1020.

- (116) Ievlev, A. V.; Brown, C. C.; Agar, J. C.; Velarde, G. A.; Martin, L. W.; Belianinov, A.; Maksymovych, P.; Kalinin, S. V.; Ovchinnikova, O. S. Nanoscale Electrochemical Phenomena of Polarization Switching in Ferroelectrics. *ACS Appl. Mater. Interfaces* **2018**, *10*, 38217–38222.
- (117) Bagotsky, V. S. *Fundamentals of Electrochemistry*; John Wiley & Sons, Inc.: Hoboken, NJ, 2005.
- (118) Bard, A. J.; Fan, F. R. F.; Kwak, J.; Lev, O. Scanning Electrochemical Microscopy. Introduction and Principles. *Anal. Chem.* **1989**, *61*, 132–138.
- (119) Cunningham, S.; Larkin, I. A.; Davis, J. H. Noncontact Scanning Probe Microscope Potentiometry of Surface Charge Patches: Origin and Interpretation of Time-Dependent Signals. *Appl. Phys. Lett.* **1998**, *73*, 123–125.
- (120) Bluhm, H.; Schwarz, U. D.; Wiesendanger, R. Origin of the Ferroelectric Domain Contrast Observed in Lateral Force Microscopy. *Phys. Rev. B: Condens. Matter Mater. Phys.* **1998**, *57*, 161–169.
- (121) Belaidi, S.; Girard, P.; Leveque, G. Electrostatic Forces Acting on the Tip in Atomic Force Microscopy: Modelization and Comparison with Analytic Expressions. *J. Appl. Phys.* **1997**, *81*, 1023–1030.
- (122) Bluhm, H.; Wadas, A.; Wiesendanger, R.; Meyer, K. P.; Szczesniak, L. Electrostatic Force Microscopy on Ferroelectric Crystals in Inert Gas Atmosphere. *Phys. Rev. B: Condens. Matter Mater. Phys.* **1997**, *55*, 4–7.
- (123) Nonnenmacher, M.; O'Boyle, M. P.; Wickramasinghe, H. K. Kelvin Probe Force Microscopy. *Appl. Phys. Lett.* **1991**, *58*, 2921–2923.
- (124) Guo, S.; Kalinin, S. V.; Jesse, S. Open-Loop Band Excitation Kelvin Probe Force Microscopy. *Nanotechnology* **2012**, *23*, 125704–10.
- (125) Borgani, R.; Forchheimer, D.; Bergqvist, J.; Thorén, P.-A.; Inganäs, O.; Haviland, D. B. Intermodulation Electrostatic Force Microscopy for Imaging Surface Photo-Voltage. *Appl. Phys. Lett.* **2014**, *105*, 143113.
- (126) Wandelt, K. The Local Work Function: Concept and Implications. *Appl. Surf. Sci.* **1997**, *111*, 1–10.
- (127) Brenes, R.; Eames, C.; Bulović, V.; Islam, M. S.; Stranks, S. D. The Impact of Atmosphere on the Local Luminescence Properties of Metal Halide Perovskite Grains. *Adv. Mater.* **2018**, *30*, 1706208.
- (128) Melitz, W.; Shen, J.; Kummel, A. C.; Lee, S. Kelvin Probe Force Microscopy and its Application. *Surf. Sci. Rep.* **2011**, *66*, 1–27.
- (129) Bocquet, F.; Nony, L.; Loppacher, C.; Glatzel, T. Analytical Approach to the Local Contact Potential Difference on (001) Ionic Surfaces: Implications for Kelvin Probe Force Microscopy. *Phys. Rev. B: Condens. Matter Mater. Phys.* **2008**, *78*, 035410.
- (130) Schuler, B.; Liu, S.-X.; Geng, Y.; Decurtins, S.; Meyer, G.; Gross, L. Contrast Formation in Kelvin Probe Force Microscopy of Single π -Conjugated Molecules. *Nano Lett.* **2014**, *14*, 3342–3346.
- (131) Zerweck, U.; Loppacher, C.; Otto, T.; Grafström, S.; Eng, L. M. Accuracy and Resolution Limits of Kelvin Probe Force Microscopy. *Phys. Rev. B: Condens. Matter Mater. Phys.* **2005**, *71*, 125424.
- (132) Charrier, D. S. H.; Kemerink, M.; Smalbrugge, B. E.; de Vries, T.; Janssen, R. A. J. Real Versus Measured Surface Potentials in Scanning Kelvin Probe Microscopy. *ACS Nano* **2008**, *2*, 622–626.
- (133) Barbet, S.; Popoff, M.; Diesinger, H.; Deresmes, D.; Théron, D.; Mélin, T. Cross-Talk Artefacts in Kelvin Probe Force Microscopy Imaging: A Comprehensive Study. *J. Appl. Phys.* **2014**, *115*, 144313.
- (134) Axt, A.; Hermes, I. M.; Bergmann, V. W.; Tausendpfund, N.; Weber, S. A. L. Know Your Full Potential: Quantitative Kelvin Probe Force Microscopy on Nanoscale Electrical Devices. *Beilstein J. Nanotechnol.* **2018**, *9*, 1809–1819.
- (135) Ottinger, O. M.; Melzer, C.; von Seggern, H. Pitfalls in Kelvin Probe Measurements. *J. Appl. Phys.* **2009**, *106*, 023704.
- (136) Yamamoto, S.; Susa, K.; Kawabe, U. Work Functions of Binary Compounds. *J. Chem. Phys.* **1974**, *60*, 4076–4080.
- (137) Wu, Q.-H. Electrochemical Potential of Intercalation Phase: $\text{Li}/\text{V}_2\text{O}_5$ System. *Appl. Surf. Sci.* **2006**, *253*, 1713–1716.
- (138) Tonti, D.; Pettenkofer, C.; Jaegermann, W. Origin of the Electrochemical Potential in Intercalation Electrodes: Experimental Estimation of the Electronic and Ionic Contributions for Na Intercalated into TiS_2 . *J. Phys. Chem. B* **2004**, *108*, 16093–16099.
- (139) Greiner, M. T.; Chai, L.; Helander, M. G.; Tang, W.-M.; Lu, Z.-H. Transition Metal Oxide Work Functions: The Influence of Cation Oxidation State and Oxygen Vacancies. *Adv. Funct. Mater.* **2012**, *22*, 4557–4568.
- (140) Zhu, J.; Zeng, K.; Lu, L. *In Situ* Nanoscale Mapping of Surface Potential in All-Solid-State Thin Film Li-Ion Battery Using Kelvin Probe Force Microscopy. *J. Appl. Phys.* **2012**, *111*, 063723.
- (141) Nagpure, S. C.; Bhushan, B.; Babu, S. S. Surface Potential Measurement of Aged Li-Ion Batteries Using Kelvin Probe Microscopy. *J. Power Sources* **2011**, *196*, 1508–1512.
- (142) Luchkin, S. Y.; Amanieu, H.-Y.; Rosato, D.; Kholkin, A. L. Li Distribution in Graphite Anodes: A Kelvin Probe Force Microscopy Approach. *J. Power Sources* **2014**, *268*, 887–894.
- (143) Masuda, H.; Ishida, N.; Ogata, Y.; Ito, D.; Fujita, D. Internal Potential Mapping of Charged Solid-State-Lithium Ion Batteries Using *in Situ* Kelvin Probe Force Microscopy. *Nanoscale* **2017**, *9*, 893–898.
- (144) Luntz, A. C.; Voss, J.; Reuter, K. Interfacial Challenges in Solid-State Li Ion Batteries. *J. Phys. Chem. Lett.* **2015**, *6*, 4599–4604.
- (145) Nonnenmann, S. S.; Bonnell, D. A. Miniature Environmental Chamber Enabling *in Situ* Scanning Probe Microscopy Within Reactive Environments. *Rev. Sci. Instrum.* **2013**, *84*, 073707.
- (146) Kalinin, S. V.; Bonnell, D. A. Scanning Impedance Microscopy of Electroactive Interfaces. *Appl. Phys. Lett.* **2001**, *78*, 1306–1308.
- (147) Kalinin, S. V.; Suchomel, M. R.; Davies, P. K.; Bonnell, D. A. Potential and Impedance Imaging of Polycrystalline BiFeO_3 Ceramics. *J. Am. Ceram. Soc.* **2002**, *85*, 3011–3017.
- (148) Zhu, J.; Pérez, C. R.; Oh, T.-S.; Küngas, R.; Vohs, J. M.; Bonnell, D. A.; Nonnenmann, S. S. Probing Local Electrochemical Activity Within Yttria-Stabilized-Zirconia *via in Situ* High-Temperature Atomic Force Microscopy. *J. Mater. Res.* **2015**, *30*, 357–363.
- (149) Nonnenmann, S. S.; Kungas, R.; Vohs, J.; Bonnell, D. A. Direct *in Situ* Probe of Electrochemical Processes in Operating Fuel Cells. *ACS Nano* **2013**, *7*, 6330–6336.
- (150) Nonnenmann, S. S. A Hot Tip: Imaging Phenomena Using *in Situ* Multi-Stimulus Probes at High Temperatures. *Nanoscale* **2016**, *8*, 3164–3180.
- (151) Zhu, J.; Wang, J.; Mebane, D. S.; Nonnenmann, S. S. *In Situ* Surface Potential Evolution Along Au/Gd:CeO₂ Electrode Interfaces. *APL Mater.* **2017**, *5*, 042503.
- (152) Strelcov, E.; Jesse, S.; Huang, Y. L.; Teng, Y. C.; Kravchenko, I. I.; Chu, Y. H.; Kalinin, S. V. Space- and Time-Resolved Mapping of Ionic Dynamic and Electroresistive Phenomena in Lateral Devices. *ACS Nano* **2013**, *7*, 6806–6815.
- (153) Strelcov, E.; Ievlev, A. V.; Jesse, S.; Kravchenko, I. I.; Shur, V. Y.; Kalinin, S. V. Direct Probing of Charge Injection and Polarization-Controlled Ionic Mobility on Ferroelectric LiNbO_3 Surfaces. *Adv. Mater.* **2014**, *26*, 958–963.
- (154) Shockley, W.; Hooper, W. W.; Queisser, H. J.; Schroen, W. Mobile Electric Charges on Insulating Oxides with Application to Covered Silicon *p-n* Junctions. *Surf. Sci.* **1964**, *2*, 277–287.
- (155) Kiselev, I.; Sommer, M.; Sysoev, V. V. Electric Field-Induced Rearrangement of Charged Species in Metal Oxide Devices with Resistive Change: Thermodynamic Limitations. *Eur. Phys. J. B* **2011**, *82*, 7–12.
- (156) Kalinin, S. V.; Bonnell, D. A. Local Potential and Polarization Screening on Ferroelectric Surfaces. *Phys. Rev. B: Condens. Matter Mater. Phys.* **2001**, *63*, 125411.
- (157) Ding, J.; Strelcov, E.; Kalinin, S. V.; Bassiri-Gharb, N. Spatially Resolved Probing of Electrochemical Reactions *via* Energy Discovery Platforms. *Nano Lett.* **2015**, *15*, 3669–3676.
- (158) Bürgi, L.; Sirringhaus, H.; Friend, R. H. Noncontact Potentiometry of Polymer Field-Effect Transistors. *Appl. Phys. Lett.* **2002**, *80*, 2913–2915.

- (159) Silveira, W. R.; Marohn, J. A. Microscopic View of Charge Injection in an Organic Semiconductor. *Phys. Rev. Lett.* **2004**, *93*, 116104.
- (160) Muller, E. M.; Marohn, J. A. Microscopic Evidence for Spatially Inhomogeneous Charge Trapping in Pentacene. *Adv. Mater.* **2005**, *17*, 1410–1414.
- (161) Ding, J.; Strelcov, E.; Kalinin, V. S.; Bassiri-Gharb, N. Electrochemical Reactivity and Proton Transport Mechanisms in Nanostructured Ceria. *Nanotechnology* **2016**, *27*, 345401.
- (162) Ding, J.; Strelcov, E.; Bassiri-Gharb, N. Effects of Microstructure on Electrochemical Reactivity and Conductivity in Nanostructured Ceria Thin Films. *J. Am. Ceram. Soc.* **2018**, *101*, 283–292.
- (163) Schirmeisen, A.; Taskiran, A.; Fuchs, H.; Røling, B.; Murugavel, S.; Bracht, H.; Natrup, F. Probing Ion Transport at the Nanoscale: Time-Domain Electrostatic Force Spectroscopy on Glassy Electrolytes. *Appl. Phys. Lett.* **2004**, *85*, 2053–2055.
- (164) Mascaro, A.; Wang, Z.; Hovington, P.; Miyahara, Y.; Paoletta, A.; Garipey, V.; Feng, Z.; Enright, T.; Aiken, C.; Zaghbi, K.; Bevan, K. H.; Grutter, P. Measuring Spatially Resolved Collective Ionic Transport on Lithium Battery Cathodes Using Atomic Force Microscopy. *Nano Lett.* **2017**, *17*, 4489–4496.
- (165) Lee, W.; Lee, M.; Kim, Y.-B.; Prinz, F. B. Reduction and Oxidation of Oxide Ion Conductors With Conductive Atomic Force Microscopy. *Nanotechnology* **2009**, *20*, 445706.
- (166) Collins, L.; Ahmadi, M.; Wu, T.; Hu, B.; Kalinin, S. V.; Jesse, S. Breaking the Time Barrier in Kelvin Probe Force Microscopy: Fast Free Force Reconstruction Using the G-Mode Platform. *ACS Nano* **2017**, *11*, 8717–8729.
- (167) Belianinov, A.; Kalinin, S. V.; Jesse, S. Complete Information Acquisition in Dynamic Force Microscopy. *Nat. Commun.* **2015**, *6*, 6550–6558.
- (168) Collins, L.; Belianinov, A.; Somnath, S.; Balke, N.; Kalinin, S. V.; Jesse, S. Full data acquisition in Kelvin Probe Force Microscopy: Mapping dynamic electric phenomena in real space. *Sci. Rep.* **2016**, *6*, 30557.
- (169) Li, Z.; Klein, T. R.; Kim, D. H.; Yang, M.; Berry, J. J.; van Hest, M. F. A. M.; Zhu, K. Scalable Fabrication of Perovskite Solar Cells. *Nat. Rev. Mater.* **2018**, *3*, 18017.
- (170) Ahmadi, M.; Wu, T.; Hu, B. A Review on Organic–Inorganic Halide Perovskite Photodetectors: Device Engineering and Fundamental Physics. *Adv. Mater.* **2017**, *29*, 1605242.
- (171) Cho, H.; Jeong, S.-H.; Park, M.-H.; Kim, Y.-H.; Wolf, C.; Lee, C.-L.; Heo, J. H.; Sadhanala, A.; Myoung, N.; Yoo, S.; Im, S. H.; Friend, R. H.; Lee, T.-W. Overcoming the Electroluminescence Efficiency Limitations of Perovskite Light-Emitting Diodes. *Science* **2015**, *350*, 1222–1225.
- (172) Yakunin, S.; Dirin, D. N.; Shynkarenko, Y.; Morad, V.; Cherniukh, I.; Nazarenko, O.; Kreil, D.; Nauser, T.; Kovalenko, M. V. Detection of Gamma Photons Using Solution-Grown Single Crystals of Hybrid Lead Halide Perovskites. *Nat. Photonics* **2016**, *10*, 585–589.
- (173) Hansma, P.; Drake, B.; Marti, O.; Gould, S.; Prater, C. The Scanning Ion-Conductance Microscope. *Science* **1989**, *243*, 641–643.
- (174) Ebejer, N.; Schnippering, M.; Colburn, A. W.; Edwards, M. A.; Unwin, P. R. Localized High Resolution Electrochemistry and Multifunctional Imaging: Scanning Electrochemical Cell Microscopy. *Anal. Chem.* **2010**, *82*, 9141–9145.
- (175) Ritzert, N. L.; Szalai, V. A.; Moffat, T. P. Mapping Electron Transfer at MoS₂ Using Scanning Electrochemical Microscopy. *Langmuir* **2018**, *34*, 13864–13870.
- (176) Bentley, C. L.; Edmondson, J.; Meloni, G. N.; Perry, D.; Shkirskiy, V.; Unwin, P. R. Nanoscale Electrochemical Mapping. *Anal. Chem.* **2019**, *91*, 84–108.
- (177) Kai, T.; Zoski, C. G.; Bard, A. J. Scanning Electrochemical Microscopy at the Nanometer Level. *Chem. Commun.* **2018**, *54*, 1934–1947.
- (178) Yamada, H.; Haraguchi, D.; Yasunaga, K. Fabrication and Characterization of a K⁺-Selective Nanoelectrode and Simultaneous Imaging of Topography and Local K⁺ Flux Using Scanning Electrochemical Microscopy. *Anal. Chem.* **2014**, *86*, 8547–8552.
- (179) Snook, G. A.; Huynh, T. D.; Hollenkamp, A. F.; Best, A. S. Rapid SECM Probing of Dissolution of LiCoO₂ Battery Materials in an Ionic Liquid. *J. Electroanal. Chem.* **2012**, *687*, 30–34.
- (180) Lipson, A. L.; Puntambekar, K.; Comstock, D. J.; Meng, X.; Geier, M. L.; Elam, J. W.; Hersam, M. C. Nanoscale Investigation of Solid Electrolyte Interphase Inhibition on Li-Ion Battery MnO Electrodes via Atomic Layer Deposition of Al₂O₃. *Chem. Mater.* **2014**, *26*, 935–940.
- (181) Lipson, A. L.; Ginder, R. S.; Hersam, M. C. Nanoscale *In Situ* Characterization of Li-ion Battery Electrochemistry via Scanning Ion Conductance Microscopy. *Adv. Mater.* **2011**, *23*, 5613–5617.
- (182) Zampardi, G.; Ventosa, E.; La Mantia, F.; Schuhmann, W. *In Situ* Visualization of Li-Ion Intercalation and Formation of the Solid Electrolyte Interphase on TiO₂ Based Paste Electrodes Using Scanning Electrochemical Microscopy. *Chem. Commun.* **2013**, *49*, 9347–9349.
- (183) Zampardi, G.; La Mantia, F.; Schuhmann, W. Determination of The Formation and Range of Stability of the SEI on Glassy Carbon by Local Electrochemistry. *RSC Adv.* **2015**, *5*, 31166–31171.
- (184) Bültner, H.; Schwager, P.; Fenske, D.; Wittstock, G. Observation of Dynamic Interfacial Layers in Li-Ion and Li-O₂ Batteries by Scanning Electrochemical Microscopy. *Electrochim. Acta* **2016**, *199*, 366–379.
- (185) Takahashi, Y.; Kumatani, A.; Munakata, H.; Inomata, H.; Ito, K.; Ino, K.; Shiku, H.; Unwin, P. R.; Korchev, Y. E.; Kanamura, K.; Matsue, T. Nanoscale Visualization of Redox Activity at Lithium-Ion Battery Cathodes. *Nat. Commun.* **2014**, *5*, 5450–5457.
- (186) Catarelli, S. R.; Lonsdale, D.; Cheng, L.; Syzdek, J.; Doeff, M. Intermittent Contact Alternating Current Scanning Electrochemical Microscopy: A Method for Mapping Conductivities in Solid Li Ion Conducting Electrolyte Samples. *Front. Energy Res.* **2016**, *4*, 1–8.
- (187) Kim, J.; Renault, C.; Nioradze, N.; Arroyo-Currás, N.; Leonard, K. C.; Bard, A. J. Electrocatalytic Activity of Individual Pt Nanoparticles Studied by Nanoscale Scanning Electrochemical Microscopy. *J. Am. Chem. Soc.* **2016**, *138*, 8560–8568.
- (188) Kang, M.; Perry, D.; Bentley, C. L.; West, G.; Page, A.; Unwin, P. R. Simultaneous Topography and Reaction Flux Mapping at and around Electrocatalytic Nanoparticles. *ACS Nano* **2017**, *11*, 9525–9535.
- (189) Bentley, C. L.; Unwin, P. R. Nanoscale Electrochemical Movies and Synchronous Topographical Mapping of Electrocatalytic Materials. *Faraday Discuss.* **2018**, *210*, 365–379.
- (190) Cao, F.; Kim, J.; Bard, A. J. Detection of the Short-Lived Cation Radical Intermediate in the Electrochemical Oxidation of *N,N*-Dimethylaniline by Scanning Electrochemical Microscopy. *J. Am. Chem. Soc.* **2014**, *136*, 18163–18169.
- (191) Chang, J.; Bard, A. J. Detection of the Sn(III) Intermediate and the Mechanism of the Sn(IV)/Sn(II) Electroreduction Reaction in Bromide Media by Cyclic Voltammetry and Scanning Electrochemical Microscopy. *J. Am. Chem. Soc.* **2014**, *136*, 311–320.
- (192) Kai, T.; Zhou, M.; Duan, Z.; Henkelman, G. A.; Bard, A. J. Detection of CO₂^{•-} in the Electrochemical Reduction of Carbon Dioxide in *N,N*-Dimethylformamide by Scanning Electrochemical Microscopy. *J. Am. Chem. Soc.* **2017**, *139*, 18552–18557.
- (193) Zhou, M.; Yu, Y.; Hu, K.; Mirklin, M. V. Nanoelectrochemical Approach To Detecting Short-Lived Intermediates of Electrocatalytic Oxygen Reduction. *J. Am. Chem. Soc.* **2015**, *137*, 6517–6523.
- (194) Fan, F.-R. F.; Bard, A. J. Imaging of Biological Macromolecules on Mica in Humid Air by Scanning Electrochemical Microscopy. *Proc. Natl. Acad. Sci. U. S. A.* **1999**, *96*, 14222–14227.
- (195) Barton, Z. J.; Rodríguez-López, J. Emerging Scanning Probe Approaches to the Measurement of Ionic Reactivity at Energy Storage Materials. *Anal. Bioanal. Chem.* **2016**, *408*, 2707–2715.
- (196) Hui, J.; Gossage, Z. T.; Sarbapalli, D.; Hernández-Burgos, K.; Rodríguez-López, J. Advanced Electrochemical Analysis for Energy Storage Interfaces. *Anal. Chem.* **2019**, *91*, 60–83.
- (197) Hernández-Burgos, K.; Barton, Z. J.; Rodríguez-López, J. Finding Harmony between Ions and Electrons: New Tools and

- Concepts for Emerging Energy Storage Materials. *Chem. Mater.* **2017**, *29*, 8918–8931.
- (198) Danis, L.; Gateman, S. M.; Kuss, C.; Schougaard, S. B.; Mauzeroll, J. Nanoscale Measurements of Lithium-Ion-Battery Materials using Scanning Probe Techniques. *ChemElectroChem* **2017**, *4*, 6–19.
- (199) O'Hayre, R.; Lee, M.; Prinz, F. B. Ionic and Electronic Impedance Imaging Using Atomic Force Microscopy. *J. Appl. Phys.* **2004**, *95*, 8382–8392.
- (200) Tselev, A.; Velmurugan, J.; Ievlev, A. V.; Kalinin, S. V.; Kolmakov, A. Seeing through Walls at the Nanoscale: Microwave Microscopy of Enclosed Objects and Processes in Liquids. *ACS Nano* **2016**, *10*, 3562–3570.
- (201) Strelcov, E.; Kim, Y.; Jesse, S.; Cao, Y.; Ivanov, I. N.; Kravchenko, I. I.; Wang, C. H.; Teng, Y. C.; Chen, L. Q.; Chu, Y. H.; Kalinin, S. V. Probing Local Ionic Dynamics in Functional Oxides at the Nanoscale. *Nano Lett.* **2013**, *13*, 3455–3462.
- (202) Cahen, D.; Chernyak, L.; Dagan, G.; Jakubowicz, A. Ion Mobility in Chalcogenide Semiconductors - Room Temperature Creation of Bipolar Junction Transistor. In *Fast Ion Transport in Solids*; Scrosati, B., Magistris, A., Mari, C. M., Mariotto, G., Eds.; Kluwer Academic Publ: Dordrecht, 1993; Vol. 250, pp 121–141.
- (203) Cahen, D.; Gilet, J. M.; Schmitz, C.; Chernyak, L.; Gartsman, K.; Jakubowicz, A. Room-Temperature, Electric-Field Induced Creation of Stable Devices in CuInSe_2 Crystals. *Science* **1992**, *258*, 271–274.
- (204) Yang, R.; Terabe, K.; Liu, G.; Tsuruoka, T.; Hasegawa, T.; Gimzewski, J. K.; Aono, M. On-Demand Nanodevice with Electrical and Neuromorphic Multifunction Realized by Local Ion Migration. *ACS Nano* **2012**, *6*, 9515–9521.
- (205) Lee, K. C.; Yoo, H. I. Hebb-Wagner-Type Polarization Relaxation in The Presence of the Cross Effect Between Electronic and Ionic Flows in a Mixed Conductor. *J. Phys. Chem. Solids* **1999**, *60*, 911–927.
- (206) Cahen, D.; Chernyak, L. Dopant Electromigration in Semiconductors. *Adv. Mater.* **1997**, *9*, 861–870.
- (207) Milewska, A.; Świerczek, K.; Tobola, J.; Boudoire, F.; Hu, Y.; Bora, D. K.; Mun, B. S.; Braun, A.; Molenda, J. The Nature of the Nonmetal–Metal Transition in Li_xCoO_2 Oxide. *Solid State Ionics* **2014**, *263*, 110–118.
- (208) Yang, C. H.; Seidel, J.; Kim, S. Y.; Rossen, P. B.; Yu, P.; Gajek, M.; Chu, Y. H.; Martin, L. W.; Holcomb, M. B.; He, Q.; Maksymovych, P.; Balke, N.; Kalinin, S. V.; Baddorf, A. P.; Basu, S. R.; Scullin, M. L.; Ramesh, R. Electric Modulation of Conduction in Multiferroic Ca-Doped BiFeO_3 Films. *Nat. Mater.* **2009**, *8*, 485–490.
- (209) Verde, M. G.; Baggetto, L.; Balke, N.; Veith, G. M.; Seo, J. K.; Wang, Z.; Meng, Y. S. Elucidating the Phase Transformation of $\text{Li}_4\text{Ti}_5\text{O}_{12}$ Lithiation at the Nanoscale. *ACS Nano* **2016**, *10*, 4312–4321.
- (210) Borgani, R.; Kohan, M. G.; Vomiero, A.; Haviland, D. B. Fast Multifrequency Measurement of Nonlinear Conductance. *Phys. Rev. Appl.* **2019**, *11*, 044062.
- (211) Somnath, S.; Law, K. J. H.; Morozovska, A. N.; Maksymovych, P.; Kim, Y.; Lu, X.; Alexe, M.; Archibald, R.; Kalinin, S. V.; Jesse, S.; Vasudevan, R. K. Ultrafast Current Imaging by Bayesian Inversion. *Nat. Commun.* **2018**, *9*, 513–520.
- (212) Kim, Y.; Strelcov, E.; Hwang, I. R.; Choi, T.; Park, B. H.; Jesse, S.; Kalinin, S. V. Correlative Multimodal Probing of Ionically-Mediated Electromechanical Phenomena in Simple Oxides. *Sci. Rep.* **2013**, *3*, 2924.
- (213) Belianinov, A.; Vasudevan, R.; Strelcov, E.; Steed, C.; Yang, S.; Tselev, A.; Jesse, S.; Biegalski, M.; Shipman, G.; Symons, C.; Borisevich, A.; Archibald, R.; Kalinin, S. Big Data and Deep Data in Scanning and Electron Microscopies: Deriving Functionality from Multidimensional Data Sets. *Adv. Struct. Chem. Imaging* **2015**, *1*, 1–25.
- (214) Lu, W.; Xiao, J.; Wong, L.-M.; Wang, S.; Zeng, K. Probing the Ionic and Electrochemical Phenomena during Resistive Switching of NiO Thin Films. *ACS Appl. Mater. Interfaces* **2018**, *10*, 8092–8101.
- (215) Lu, W.; Wong, L.-M.; Wang, S.; Zeng, K. Effects of Oxygen and Moisture on the I-V Characteristics of TiO_2 Thin Films. *J. Mater. Inform.* **2018**, *4*, 228–237.
- (216) Dobigeon, N.; Moussaoui, S.; Coulon, M.; Tourneret, J. Y.; Hero, A. O. Joint Bayesian Endmember Extraction and Linear Unmixing for Hyperspectral Imagery. *IEEE Trans. Signal Process.* **2009**, *57*, 4355–4368.
- (217) Hsieh, Y.-H.; Strelcov, E.; Liou, J.-M.; Shen, C.-Y.; Chen, Y.-C.; Kalinin, S. V.; Chu, Y.-H. Electrical Modulation of the Local Conduction at Oxide Tubular Interfaces. *ACS Nano* **2013**, *7*, 8627–8633.
- (218) Strelcov, E.; Belianinov, A.; Hsieh, Y.-H.; Jesse, S.; Baddorf, A. P.; Chu, Y.-H.; Kalinin, S. V. Deep Data Analysis of Conductive Phenomena on Complex Oxide Interfaces: Physics from Data Mining. *ACS Nano* **2014**, *8*, 6449–6457.
- (219) Strelcov, E.; Belianinov, A.; Hsieh, Y.-H.; Chu, Y.-H.; Kalinin, S. V. Constraining Data Mining with Physical Models: Voltage- and Oxygen Pressure-Dependent Transport in Multiferroic Nanostructures. *Nano Lett.* **2015**, *15*, 6650–6657.
- (220) Yang, S. M.; Lee, S.; Jian, J.; Zhang, W.; Lu, P.; Jia, Q.; Wang, H.; Won Noh, T.; Kalinin, S. V.; MacManusDriscoll, J. L. Strongly Enhanced Oxygen Ion Transport Through Samarium-Doped CeO_2 Nanopillars in Nanocomposite Films. *Nat. Commun.* **2015**, *6*, 8588–8594.
- (221) Armand, M.; Endres, F.; MacFarlane, D. R.; Ohno, H.; Scrosati, B. Ionic-Liquid Materials for the Electrochemical Challenges of the Future. *Nat. Mater.* **2009**, *8*, 621–629.
- (222) Hallett, J. P.; Welton, T. Room-Temperature Ionic Liquids: Solvents for Synthesis and Catalysis. 2. *Chem. Rev.* **2011**, *111*, 3508–3576.
- (223) Marr, P. C.; Marr, A. C. Ionic Liquid Gel Materials: Applications in Green and Sustainable Chemistry. *Green Chem.* **2016**, *18*, 105–128.
- (224) MacFarlane, D. R.; Tachikawa, N.; Forsyth, M.; Pringle, J. M.; Howlett, P. C.; Elliott, G. D.; Davis, J. H.; Watanabe, M.; Simon, P.; Angell, C. A. Energy Applications of Ionic Liquids. *Energy Environ. Sci.* **2014**, *7*, 232–250.
- (225) Yang, Q.; Zhang, Z.; Sun, X.-G.; Hu, Y.-S.; Xing, H.; Dai, S. Ionic Liquids and Derived Materials for Lithium and Sodium Batteries. *Chem. Soc. Rev.* **2018**, *47*, 2020–2064.
- (226) Zeng, S.; Zhang, X.; Bai, L.; Zhang, X.; Wang, H.; Wang, J.; Bao, D.; Li, M.; Liu, X.; Zhang, S. Ionic-Liquid-Based CO_2 Capture Systems: Structure, Interaction and Process. *Chem. Rev.* **2017**, *117*, 9625–9673.
- (227) Chapman, D. L. Contribution to the Theory of Electrocapillarity. *Philosophical Magazine Series 6* **1913**, *25*, 475–481.
- (228) Gouy, L. G. On the Constitution of the Electric Charge at the Surface of an Electrolyte. *C. R. Hebd. Seances Acad. Sci.* **1909**, *149*, 654–657.
- (229) Stern, O. The Theory of the Electrolytic Double Shift. *Z. Elektrochem. Angew. P.* **1924**, *30*, 508–516.
- (230) Atkin, R.; Borisenko, N.; Drüscler, M.; El Abedin, S. Z.; Endres, F.; Hayes, R.; Huber, B.; Røling, B. An *in Situ* STM/AFM and Impedance Spectroscopy Study of the Extremely Pure 1-Butyl-1-Methylpyrrolidinium Tris(Pentafluoroethyl)Trifluorophosphate/Au(111) Interface: Potential Dependent Solvation Layers and the Herringbone Reconstruction. *Phys. Chem. Chem. Phys.* **2011**, *13*, 6849–6855.
- (231) Baldelli, S. Surface Structure at the Ionic Liquid–Electrified Metal Interface. *Acc. Chem. Res.* **2008**, *41*, 421–431.
- (232) Bazant, M. Z.; Storey, B. D.; Kornyshev, A. A. Double Layer in Ionic Liquids: Overscreening Versus Crowding. *Phys. Rev. Lett.* **2011**, *106*, 046102.
- (233) Cremer, T.; Stark, M.; Deyko, A.; Steinrück, H. P.; Maier, F. Liquid/Solid Interface of Ultrathin Ionic Liquid Films: $[\text{C}_1\text{C}_1\text{Im}][\text{Tf}_2\text{N}]$ and $[\text{C}_8\text{C}_1\text{Im}][\text{Tf}_2\text{N}]$ on Au(111). *Langmuir* **2011**, *27*, 3662–3671.

- (234) Fedorov, M. V.; Kornyshev, A. A. Towards Understanding the Structure and Capacitance of Electrical Double Layer in Ionic Liquids. *Electrochim. Acta* **2008**, *53*, 6835–6840.
- (235) Feng, G.; Zhang, J. S.; Qiao, R. Microstructure and Capacitance of the Electrical Double Layers at the Interface of Ionic Liquids and Planar Electrodes. *J. Phys. Chem. C* **2009**, *113*, 4549–4559.
- (236) Islam, M. M.; Alam, M. T.; Ohsaka, T. Electrical Double-Layer Structure in Ionic Liquids: A Corroboration of the Theoretical Model by Experimental Results. *J. Phys. Chem. C* **2008**, *112*, 16568–16574.
- (237) Kornyshev, A. A. Double-Layer in Ionic Liquids: Paradigm Change? *J. Phys. Chem. B* **2007**, *111*, 5545–5557.
- (238) Merlet, C.; Limmer, D. T.; Salanne, M.; van Roij, R.; Madden, P. A.; Chandler, D.; Rotenberg, B. The Electric Double Layer Has a Life of Its Own. *J. Phys. Chem. C* **2014**, *118*, 18291–18298.
- (239) Perkin, S. Ionic liquids in Confined Geometries. *Phys. Chem. Chem. Phys.* **2012**, *14*, 5052–5059.
- (240) Zhan, C.; Lian, C.; Zhang, Y.; Thompson, M. W.; Xie, Y.; Wu, J.; Kent, P. R. C.; Cummings, P. T.; Jiang, D.-e.; Wesolowski, D. J. Computational Insights into Materials and Interfaces for Capacitive Energy Storage. *Adv. Sci.* **2017**, *4*, 1700059.
- (241) Zhou, H.; Rouha, M.; Feng, G.; Lee, S. S.; Docherty, H.; Fenter, P.; Cummings, P. T.; Fulvio, P. F.; Dai, S.; McDonough, J.; Presser, V.; Gogotsi, Y. Nanoscale Perturbations of Room Temperature Ionic Liquid Structure at Charged and Uncharged Interfaces. *ACS Nano* **2012**, *6*, 9818–9827.
- (242) Black, J. M.; Walters, D.; Labuda, A.; Feng, G.; Hillesheim, P. C.; Dai, S.; Cummings, P. T.; Kalinin, S. V.; Proksch, R.; Balke, N. Bias-Dependent Molecular-Level Structure of Electrical Double Layer in Ionic Liquid on Graphite. *Nano Lett.* **2013**, *13*, 5954–5960.
- (243) Hoffmann, V.; Pulletkurthi, G.; Carstens, T.; Lahiri, A.; Borodin, A.; Schammer, M.; Horstmann, B.; Latz, A.; Endres, F. Influence of a Silver Salt on the Nanostructure of a Au(111)/Ionic Liquid Interface: An Atomic Force Microscopy Study and Theoretical Concepts. *Phys. Chem. Chem. Phys.* **2018**, *20*, 4760–4771.
- (244) Jurado, L. A.; Espinosa-Marzal, R. M. Insight into the Electrical Double Layer of an Ionic Liquid on Graphene. *Sci. Rep.* **2017**, *7*, 4225.
- (245) Li, M.-G.; Chen, L.; Zhong, Y.-X.; Chen, Z.-B.; Yan, J.-W.; Mao, B.-W. The Electrochemical Interface of Ag(111) in 1-Ethyl-3-Methylimidazolium Bis(Trifluoromethylsulfonyl)Imide Ionic Liquid—A Combined *In Situ* Scanning Probe Microscopy and Impedance Study. *Electrochim. Acta* **2016**, *197*, 282–289.
- (246) Wakeham, D.; Hayes, R.; Warr, G. G.; Atkin, R. Influence of Temperature and Molecular Structure on Ionic Liquid Solvation Layers. *J. Phys. Chem. B* **2009**, *113*, 5961–5966.
- (247) Black, J. M.; Baris Okatan, M.; Feng, G.; Cummings, P. T.; Kalinin, S. V.; Balke, N. Topological Defects in Electric Double Layers of Ionic Liquids at Carbon Interfaces. *Nano Energy* **2015**, *15*, 737–745.
- (248) Black, J. M.; Zhu, M.; Zhang, P.; Unocic, R. R.; Guo, D.; Okatan, M. B.; Dai, S.; Cummings, P. T.; Kalinin, S. V.; Feng, G.; Balke, N. Fundamental Aspects of Electric Double Layer Force-Distance Measurements at Liquid-Solid Interfaces Using Atomic Force Microscopy. *Sci. Rep.* **2016**, *6*, 32389.
- (249) Black, J. M.; Come, J.; Bi, S.; Zhu, M.; Zhao, W.; Wong, A. T.; Noh, J. H.; Pudasaini, P. R.; Zhang, P.; Okatan, M. B.; Dai, S.; Kalinin, S. V.; Rack, P. D.; Ward, T. Z.; Feng, G.; Balke, N. Role of Electrical Double Layer Structure in Ionic Liquid Gated Devices. *ACS Appl. Mater. Interfaces* **2017**, *9*, 40949–40958.
- (250) Wedig, A.; Luebben, M.; Cho, D.-Y.; Moors, M.; Skaja, K.; Rana, V.; Hasegawa, T.; Adepalli, K. K.; Yildiz, B.; Waser, R.; Valov, I. Nanoscale Cation Motion in TaO_x, HfO_x and TiO_x Memristive Systems. *Nat. Nanotechnol.* **2016**, *11*, 67–73.
- (251) Tsuruoka, T.; Terabe, K.; Hasegawa, T.; Valov, I.; Waser, R.; Aono, M. Effects of Moisture on the Switching Characteristics of Oxide-Based, Gapless-Type Atomic Switches. *Adv. Funct. Mater.* **2012**, *22*, 70–77.
- (252) Vasudevan, R. K.; Tselev, A.; Gianfrancesco, A. G.; Baddorf, A. P.; Kalinin, S. V. Atomic-Scale Electrochemistry on the Surface of a Manganite by Scanning Tunneling Microscopy. *Appl. Phys. Lett.* **2015**, *106*, 143107.
- (253) Rashidi, M.; Wolkow, R. A. Autonomous Scanning Probe Microscopy *In Situ* Tip Conditioning through Machine Learning. *ACS Nano* **2018**, *12*, 5185–5189.
- (254) Egerton, R. F.; Li, P.; Malac, M. Radiation Damage in the TEM and SEM. *Micron* **2004**, *35*, 399–409.
- (255) Egerton, R. F.; Wang, F.; Crozier, P. A. Beam-Induced Damage to Thin Specimens in an Intense Electron Probe. *Microsc. Microanal.* **2006**, *12*, 65–71.
- (256) Menter, J. W.; Bowden, F. P. The Direct Study by Electron Microscopy of Crystal Lattices and Their Imperfections. *Proc. R. Soc. London, Ser. A* **1956**, *236*, 1–13.
- (257) Pashley, D. W.; Menter, J. W.; Bassett, G. A. Observation of Dislocations in Metals by Means of Moiré Patterns on Electron Micrographs. *Nature* **1957**, *179*, 752–757.
- (258) Hirsch, P.; Cockayne, D.; Spence, J.; Whelan, M. 50 Years of TEM of Dislocations: Past, Present and Future. *Philos. Mag.* **2006**, *86*, 4519–4528.
- (259) Hirsch, P. B.; Horne, R. W.; Whelan, M. J. LXVIII. Direct Observations of the Arrangement and Motion of Dislocations in Aluminium. *Philos. Mag.* **1956**, *1*, 677–684.
- (260) Whelan, M. J.; Hirsch, P. B. Electron Diffraction From Crystals Containing Stacking Faults: II. *Philos. Mag.* **1957**, *2*, 1303–1324.
- (261) Crewe, A. V.; Wall, J.; Langmore, J. Visibility of Single Atoms. *Science* **1970**, *168*, 1338–1340.
- (262) Bleloch, A.; Lupini, A. Imaging at the Picoscale. *Mater. Today* **2004**, *7*, 42–48.
- (263) Ross, F. M. Opportunities and Challenges in Liquid Cell Electron Microscopy. *Science* **2015**, *350*, aaa9886.
- (264) Song, Z. W.; Xie, Z. H. A Literature Review of *In Situ* Transmission Electron Microscopy Technique in Corrosion Studies. *Micron* **2018**, *112*, 69–83.
- (265) Yuan, Y. F.; Amine, K.; Lu, J.; Shahbazian-Yassar, R. Understanding Materials Challenges for Rechargeable Ion Batteries With *In Situ* Transmission Electron Microscopy. *Nat. Commun.* **2017**, *8*, 15806.
- (266) Ievlev, A. V.; Jesse, S.; Cochell, T. J.; Unocic, R. R.; Protopopescu, V. A.; Kalinin, S. V. Quantitative Description of Crystal Nucleation and Growth from *In Situ* Scanning Transmission Electron Microscopy. *ACS Nano* **2015**, *9*, 11784–11791.
- (267) Wu, F.; Yao, N. Advances in Sealed Liquid Cells for *In Situ* TEM Electrochemical Investigation of Lithium-Ion Battery. *Nano Energy* **2015**, *11*, 196–210.
- (268) Leenheer, A. J.; Jungjohann, K. L.; Zavadil, K. R.; Harris, C. T. Phase Boundary Propagation in Li-Alloying Battery Electrodes Revealed by Liquid-Cell Transmission Electron Microscopy. *ACS Nano* **2016**, *10*, 5670–5678.
- (269) Williamson, M. J.; Tromp, R. M.; Vereecken, P. M.; Hull, R.; Ross, F. M. Dynamic Microscopy of Nanoscale Cluster Growth at the Solid–Liquid Interface. *Nat. Mater.* **2003**, *2*, 532–537.
- (270) Taheri, M. L.; Stach, E. A.; Arslan, I.; Crozier, P. A.; Kabius, B. C.; LaGrange, T.; Minor, A. M.; Takeda, S.; Tanase, M.; Wagner, J. B.; Sharma, R. Current Status and Future Directions for *In Situ* Transmission Electron Microscopy. *Ultramicroscopy* **2016**, *170*, 86–95.
- (271) Abellan, P.; Parent, L. R.; Al Hasan, N.; Park, C.; Arslan, I.; Karim, A. M.; Evans, J. E.; Browning, N. D. Gaining Control over Radiolytic Synthesis of Uniform Sub-3-nanometer Palladium Nanoparticles: Use of Aromatic Liquids in the Electron Microscope. *Langmuir* **2016**, *32*, 1468–1477.
- (272) Mehdi, B. L.; Gu, M.; Parent, L. R.; Xu, W.; Nasybulin, E. N.; Chen, X. L.; Unocic, R. R.; Xu, P. H.; Welch, D. A.; Abellan, P.; Zhang, J. G.; Liu, J.; Wang, C. M.; Arslan, I.; Evans, J.; Browning, N. D. *In Situ* Electrochemical Transmission Electron Microscopy for Battery Research. *Microsc. Microanal.* **2014**, *20*, 484–492.

- (273) Abellan, P.; Mehdi, B. L.; Parent, L. R.; Gu, M.; Park, C.; Xu, W.; Zhang, Y. H.; Arslan, I.; Zhang, J. G.; Wang, C. M.; Evans, J. E.; Browning, N. D. Probing the Degradation Mechanisms in Electrolyte Solutions for Li-Ion Batteries by *in Situ* Transmission Electron Microscopy. *Nano Lett.* **2014**, *14*, 1293–1299.
- (274) Sacci, R. L.; Dudney, N. J.; More, K. L.; Parent, L. R.; Arslan, I.; Browning, N. D.; Unocic, R. R. Direct Visualization of Initial SEI Morphology and Growth Kinetics During Lithium Deposition by *in Situ* Electrochemical Transmission Electron Microscopy. *Chem. Commun.* **2014**, *50*, 2104–2107.
- (275) Unocic, R. R.; Baggetto, L.; Veith, G. M.; Aguiar, J. A.; Unocic, K. A.; Sacci, R. L.; Dudney, N. J.; More, K. L. Probing Battery Chemistry With Liquid Cell Electron Energy Loss Spectroscopy. *Chem. Commun.* **2015**, *51*, 16377–16380.
- (276) Sacci, R. L.; Black, J. M.; Balke, N.; Dudney, N. J.; More, K. L.; Unocic, R. R. Nanoscale Imaging of Fundamental Li Battery Chemistry: Solid-Electrolyte Interphase Formation and Preferential Growth of Lithium Metal Nanoclusters. *Nano Lett.* **2015**, *15*, 2011–2018.
- (277) Unocic, R. R.; Sun, X. G.; Sacci, R. L.; Adamczyk, L. A.; Alsem, D. H.; Dai, S.; Dudney, N. J.; More, K. L. Direct Visualization of Solid Electrolyte Interphase Formation in Lithium-Ion Batteries with *in Situ* Electrochemical Transmission Electron Microscopy. *Microsc. Microanal.* **2014**, *20*, 1029–1037.
- (278) Unocic, R. R.; Sun, X. G.; Alsem, D. H.; Salmon, N. J.; Dai, S.; Dudney, N. J.; More, K. L. Application of *in Situ* Electrochemical Liquid Cells for Electrical Energy Storage Research. In *Advances in Imaging and Electron Physics*; Hawkes, P. W., Ed.; Elsevier Academic Press, Inc: San Diego, CA, 2013; Vol. 179, pp 176–178.
- (279) Hauwiller, M. R.; Zhang, X. W.; Liang, W. I.; Chiu, C. H.; Zhang, Q.; Zheng, W. J.; Ophus, C.; Chan, E. M.; Czarnik, C.; Pan, M.; Ross, F. M.; Wu, W. W.; Chu, Y. H.; Asta, M.; Voorhees, P. W.; Alivisatos, A. P.; Zheng, H. M. Dynamics of Nanoscale Dendrite Formation in Solution Growth Revealed Through *in Situ* Liquid Cell Electron Microscopy. *Nano Lett.* **2018**, *18*, 6427–6433.
- (280) Mehdi, B. L.; Qian, J.; Nasybulin, E.; Park, C.; Welch, D. A.; Faller, R.; Mehta, H.; Henderson, W. A.; Xu, W.; Wang, C. M.; Evans, J. E.; Liu, J.; Zhang, J. G.; Mueller, K. T.; Browning, N. D. Observation and Quantification of Nanoscale Processes in Lithium Batteries by *Operando* Electrochemical (S)TEM. *Nano Lett.* **2015**, *15*, 2168–2173.
- (281) Mehdi, B. L.; Stevens, A.; Qian, J.; Park, C.; Xu, W.; Henderson, W. A.; Zhang, J.-G.; Mueller, K. T.; Browning, N. D. The Impact of Li Grain Size on Coulombic Efficiency in Li Batteries. *Sci. Rep.* **2016**, *6*, 34267.
- (282) Leenheer, A. J.; Jungjohann, K. L.; Zavadil, K. R.; Sullivan, J. P.; Harris, C. T. Lithium Electrodeposition Dynamics in Aprotic Electrolyte Observed *in Situ* via Transmission Electron Microscopy. *ACS Nano* **2015**, *9*, 4379–4389.
- (283) Gu, M.; Parent, L. R.; Mehdi, B. L.; Unocic, R. R.; McDowell, M. T.; Sacci, R. L.; Xu, W.; Connell, J. G.; Xu, P.; Abellan, P.; Chen, X.; Zhang, Y.; Perea, D. E.; Evans, J. E.; Lauhon, L. J.; Zhang, J.-G.; Liu, J.; Browning, N. D.; Cui, Y.; Arslan, I.; et al. Demonstration of an Electrochemical Liquid Cell for *Operando* Transmission Electron Microscopy Observation of the Lithiation/Delithiation Behavior of Si Nanowire Battery Anodes. *Nano Lett.* **2013**, *13*, 6106–6112.
- (284) He, K.; Bi, X.; Yuan, Y.; Foroozan, T.; Song, B.; Amine, K.; Lu, J.; Shahbazian-Yassar, R. *Operando* Liquid Cell Electron Microscopy of Discharge and Charge Kinetics in Lithium-Oxygen Batteries. *Nano Energy* **2018**, *49*, 338–345.
- (285) Holtz, M. E.; Yu, Y.; Gunceler, D.; Gao, J.; Sundararaman, R.; Schwarz, K. A.; Arias, T. A.; Abruña, H. D.; Muller, D. A. Nanoscale Imaging of Lithium Ion Distribution During *in Situ* Operation of Battery Electrode and Electrolyte. *Nano Lett.* **2014**, *14*, 1453–1459.
- (286) Chee, S. W.; Pratt, S. H.; Hattar, K.; Duquette, D.; Ross, F. M.; Hull, R. Studying Localized Corrosion Using Liquid Cell Transmission Electron Microscopy. *Chem. Commun.* **2015**, *51*, 168–171.
- (287) Jungjohann, K. L.; Evans, J. E.; Aguiar, J. A.; Arslan, I.; Browning, N. D. Atomic-Scale Imaging and Spectroscopy for *in Situ* Liquid Scanning Transmission Electron Microscopy. *Microsc. Microanal.* **2012**, *18*, 621–627.
- (288) Abellan, P.; Woehl, T. J.; Parent, L. R.; Browning, N. D.; Evans, J. E.; Arslan, I. Factors Influencing Quantitative Liquid (Scanning) Transmission Electron Microscopy. *Chem. Commun.* **2014**, *50*, 4873–4880.
- (289) Woehl, T. J.; Jungjohann, K. L.; Evans, J. E.; Arslan, I.; Ristenpart, W. D.; Browning, N. D. Experimental Procedures to Mitigate Electron Beam Induced Artifacts During *in Situ* Fluid Imaging of Nanomaterials. *Ultramicroscopy* **2013**, *127*, 53–63.
- (290) Schneider, N. M.; Norton, M. M.; Mendel, B. J.; Grogan, J. M.; Ross, F. M.; Bau, H. H. Electron–Water Interactions and Implications for Liquid Cell Electron Microscopy. *J. Phys. Chem. C* **2014**, *118*, 22373–22382.
- (291) Fahrenkrug, E.; Alsem, D. H.; Salmon, N.; Maldonado, S. Electrochemical Measurements in *in Situ* TEM Experiments. *J. Electrochem. Soc.* **2017**, *164*, 358–364.
- (292) Kolmakova, N.; Kolmakov, A. Scanning Electron Microscopy for *in Situ* Monitoring of Semiconductor–Liquid Interfacial Processes: Electron Assisted Reduction of Ag⁺ Ions from Aqueous Solution on the Surface of TiO₂ Rutile Nanowire. *J. Phys. Chem. C* **2010**, *114*, 17233–17237.
- (293) Jensen, E.; K obler, C.; Jensen, P. S.; M olhave, K. *in Situ* SEM Microchip Setup for Electrochemical Experiments with Water Based Solutions. *Ultramicroscopy* **2013**, *129*, 63–69.
- (294) Ross, F. M. *Liquid Cell Electron Microscopy*; Cambridge University Press: New York, 2016.
- (295) Krueger, M.; Berg, S.; Stone, D. A.; Strelcov, E.; Dikin, D. A.; Kim, J.; Cote, L. J.; Huang, J.; Kolmakov, A. Drop-Casted Self-Assembling Graphene Oxide Membranes for Scanning Electron Microscopy on Wet and Dense Gaseous Samples. *ACS Nano* **2011**, *5*, 10047–10054.
- (296) Stoll, J. D.; Kolmakov, A. Electron Transparent Graphene Windows for Environmental Scanning Electron Microscopy in Liquids and Dense Gases. *Nanotechnology* **2012**, *23*, S05704.
- (297) Yulaev, A.; Guo, H.; Strelcov, E.; Chen, L.; Vlasiouk, I.; Kolmakov, A. Graphene Microcapsule Arrays for Combinatorial Electron Microscopy and Spectroscopy in Liquids. *ACS Appl. Mater. Interfaces* **2017**, *9*, 26492–26502.
- (298) Strelcov, E.; Cothren, J.; Leonard, D.; Borisevich, A. Y.; Kolmakov, A. *In Situ* SEM Study of Lithium Intercalation in Individual V₂O₅ Nanowires. *Nanoscale* **2015**, *7*, 3022–3027.
- (299) Leite, M. S.; Ruzmetov, D.; Li, Z.; Bendersky, L. A.; Bartelt, N. C.; Kolmakov, A.; Talin, A. A. Insights Into Capacity Loss Mechanisms of All-Solid-State Li-Ion Batteries with Al Anodes. *J. Mater. Chem. A* **2014**, *2*, 20552–20559.
- (300) Yulaev, A.; Oleshko, V.; Haney, P.; Liu, J.; Qi, Y.; Talin, A. A.; Leite, M. S.; Kolmakov, A. From Microparticles to Nanowires and Back: Radical Transformations in Plated Li Metal Morphology Revealed *via in Situ* Scanning Electron Microscopy. *Nano Lett.* **2018**, *18*, 1644–1650.
- (301) Boebinger, M. G.; Yeh, D.; Xu, M.; Miles, B. C.; Wang, B.; Papakyriakou, M.; Lewis, J. A.; Kondekar, N. P.; Cortes, F. J. Q.; Hwang, S.; Sang, X.; Su, D.; Unocic, R. R.; Xia, S.; Zhu, T.; McDowell, M. T. Avoiding Fracture in a Conversion Battery Material through Reaction with Larger Ions. *Joule* **2018**, *2*, 1783–1799.
- (302) Huang, J. Y.; Zhong, L.; Wang, C. M.; Sullivan, J. P.; Xu, W.; Zhang, L. Q.; Mao, S. X.; Hudak, N. S.; Liu, X. H.; Subramanian, A.; Fan, H.; Qi, L.; Kushima, A.; Li, J. *In Situ* Observation of the Electrochemical Lithiation of a Single SnO₂ Nanowire Electrode. *Science* **2010**, *330*, 1515–1520.
- (303) Liu, X. H.; Liu, Y.; Kushima, A.; Zhang, S.; Zhu, T.; Li, J.; Huang, J. Y. *In Situ* TEM Experiments of Electrochemical Lithiation and Delithiation of Individual Nanostructures. *Adv. Energy Mater.* **2012**, *2*, 722–741.
- (304) Liu, X. H.; Wang, J. W.; Huang, S.; Fan, F.; Huang, X.; Liu, Y.; Krylyuk, S.; Yoo, J.; Dayeh, S. A.; Davydov, A. V.; Mao, S. X.; Picraux,

- S. T.; Zhang, S.; Li, J.; Zhu, T.; Huang, J. Y. *In Situ* Atomic-Scale Imaging of Electrochemical Lithiation in Silicon. *Nat. Nanotechnol.* **2012**, *7*, 749–756.
- (305) McDowell, M. T.; Lee, S. W.; Harris, J. T.; Korgel, B. A.; Wang, C.; Nix, W. D.; Cui, Y. *In Situ* TEM of Two-Phase Lithiation of Amorphous Silicon Nanospheres. *Nano Lett.* **2013**, *13*, 758–764.
- (306) He, K.; Zhang, S.; Li, J.; Yu, X.; Meng, Q.; Zhu, Y.; Hu, E.; Sun, K.; Yun, H.; Yang, X.-Q.; Zhu, Y.; Gan, H.; Mo, Y.; Stach, E. A.; Murray, C. B.; Su, D. Visualizing Non-Equilibrium Lithiation of Spinel Oxide *via in Situ* Transmission Electron Microscopy. *Nat. Commun.* **2016**, *7*, 11441–11448.
- (307) Boebinger, M. G.; Xu, M.; Ma, X.; Chen, H.; Unocic, R. R.; McDowell, M. T. Distinct Nanoscale Reaction Pathways in a Sulfide Material for Sodium and Lithium Batteries. *J. Mater. Chem. A* **2017**, *5*, 11701–11709.
- (308) McDowell, M. T.; Lee, S. W.; Nix, W. D.; Cui, Y. 25th Anniversary Article: Understanding the Lithiation of Silicon and Other Alloying Anodes for Lithium-Ion Batteries. *Adv. Mater.* **2013**, *25*, 4966–4985.
- (309) Liu, X. H.; Zhong, L.; Huang, S.; Mao, S. X.; Zhu, T.; Huang, J. Y. Size-Dependent Fracture of Silicon Nanoparticles During Lithiation. *ACS Nano* **2012**, *6*, 1522–1531.
- (310) McDowell, M. T.; Lu, Z.; Koski, K. J.; Yu, J. H.; Zheng, G.; Cui, Y. *In Situ* Observation of Divergent Phase Transformations in Individual Sulfide Nanocrystals. *Nano Lett.* **2015**, *15*, 1264–1271.
- (311) He, K.; Xin, H. L.; Zhao, K.; Yu, X.; Nordlund, D.; Weng, T.-C.; Li, J.; Jiang, Y.; Cadigan, C. A.; Richards, R. M.; Doeff, M. M.; Yang, X.-Q.; Stach, E. A.; Li, J.; Lin, F.; Su, D. Transitions from Near-Surface to Interior Redox upon Lithiation in Conversion Electrode Materials. *Nano Lett.* **2015**, *15*, 1437–1444.
- (312) Lee, S. W.; Lee, H.-W.; Ryu, I.; Nix, W. D.; Gao, H.; Cui, Y. Kinetics and Fracture Resistance of Lithiated Silicon Nanostructure Pairs Controlled by Their Mechanical Interaction. *Nat. Commun.* **2015**, *6*, 7533–7539.
- (313) Yang, H.; Fan, F.; Liang, W.; Guo, X.; Zhu, T.; Zhang, S. A Chemo-Mechanical Model of Lithiation in Silicon. *J. Mech. Phys. Solids* **2014**, *70*, 349–361.
- (314) Yang, H.; Huang, S.; Huang, X.; Fan, F.; Liang, W.; Liu, X. H.; Chen, L.-Q.; Huang, J. Y.; Li, J.; Zhu, T.; Zhang, S. Orientation-Dependent Interfacial Mobility Governs the Anisotropic Swelling in Lithiated Silicon Nanowires. *Nano Lett.* **2012**, *12*, 1953–1958.
- (315) Zhu, Y.; Wang, J. W.; Liu, Y.; Liu, X.; Kushima, A.; Liu, Y.; Xu, Y.; Mao, S. X.; Li, J.; Wang, C.; Huang, J. Y. *In Situ* Atomic-Scale Imaging of Phase Boundary Migration in FePO₄ Microparticles During Electrochemical Lithiation. *Adv. Mater.* **2013**, *25*, 5461–5466.
- (316) Manthiram, A.; Yu, X.; Wang, S. Lithium Battery Chemistries Enabled by Solid-State Electrolytes. *Nat. Rev. Mater.* **2017**, *2*, 16103.
- (317) Zhu, Y.; He, X.; Mo, Y. First Principles Study on Electrochemical and Chemical Stability of Solid Electrolyte–Electrode Interfaces in All-Solid-State Li-Ion Batteries. *J. Mater. Chem. A* **2016**, *4*, 3253–3266.
- (318) Zhu, Y.; He, X.; Mo, Y. Origin of Outstanding Stability in the Lithium Solid Electrolyte Materials: Insights from Thermodynamic Analyses Based on First-Principles Calculations. *ACS Appl. Mater. Interfaces* **2015**, *7*, 23685–23693.
- (319) Richards, W. D.; Miara, L. J.; Wang, Y.; Kim, J. C.; Ceder, G. Interface Stability in Solid-State Batteries. *Chem. Mater.* **2016**, *28*, 266–273.
- (320) Sakuda, A.; Hayashi, A.; Tatsumisago, M. Interfacial Observation between LiCoO₂ Electrode and Li₂S–P₂S₅ Solid Electrolytes of All-Solid-State Lithium Secondary Batteries Using Transmission Electron Microscopy. *Chem. Mater.* **2010**, *22*, 949–956.
- (321) Augustyn, V.; McDowell, M. T.; Vojvodic, A. Toward an Atomistic Understanding of Solid-State Electrochemical Interfaces for Energy Storage. *Joule* **2018**, *2*, 2189–2193.
- (322) Ma, C.; Cheng, Y.; Yin, K.; Luo, J.; Sharafi, A.; Sakamoto, J.; Li, J.; More, K. L.; Dudney, N. J.; Chi, M. Interfacial Stability of Li Metal–Solid Electrolyte Elucidated *via in Situ* Electron Microscopy. *Nano Lett.* **2016**, *16*, 7030–7036.
- (323) Lewis, J. A.; Cortes, F. J. Q.; Boebinger, M. G.; Tippens, J.; Marchese, T. S.; Kondekar, N.; Liu, X.; Chi, M.; McDowell, M. T. Interphase Morphology between a Solid-State Electrolyte and Lithium Controls Cell Failure. *ACS Energy Lett.* **2019**, *4*, 591–599.
- (324) Wang, Z.; Santhanagopalan, D.; Zhang, W.; Wang, F.; Xin, H. L.; He, K.; Li, J.; Dudney, N.; Meng, Y. S. *In Situ* STEM-EELS Observation of Nanoscale Interfacial Phenomena in All-Solid-State Batteries. *Nano Lett.* **2016**, *16*, 3760–3767.
- (325) Yamamoto, K.; Iriyama, Y.; Asaka, J.; Hirayama, T.; Fujita, H.; Fisher, C. A. J.; Nonaka, K.; Sugita, Y.; Ogumi, Z. Dynamic Visualization of the Electric Potential in an All-Solid-State Rechargeable Lithium Battery. *Angew. Chem., Int. Ed.* **2010**, *49*, 4414–4417.
- (326) Ruzmetov, D.; Oleshko, V. P.; Haney, P. M.; Lezec, H. J.; Karki, K.; Baloch, K. H.; Agrawal, A. K.; Davydov, A. V.; Krylyuk, S.; Liu, Y.; Huang, J.; Tanase, M.; Cumings, J.; Talin, A. A. Electrolyte Stability Determines Scaling Limits for Solid-State 3D Li Ion Batteries. *Nano Lett.* **2012**, *12*, 505–511.
- (327) Gong, Y.; Chen, Y.; Zhang, Q.; Meng, F.; Shi, J.-A.; Liu, X.; Liu, X.; Zhang, J.; Wang, H.; Wang, J.; Yu, Q.; Zhang, Z.; Xu, Q.; Xiao, R.; Hu, Y.-S.; Gu, L.; Li, H.; Huang, X.; Chen, L. Three-Dimensional Atomic-Scale Observation of Structural Evolution of Cathode Material in a Working All-Solid-State Battery. *Nat. Commun.* **2018**, *9*, 3341–3348.
- (328) Lin, F.; Markus, I. M.; Doeff, M. M.; Xin, H. L. Chemical and Structural Stability of Lithium-Ion Battery Electrode Materials under Electron Beam. *Sci. Rep.* **2015**, *4*, 5694–5700.
- (329) Stevens, A.; Luzzi, L.; Yang, H.; Kovarik, L.; Mehdi, B. L.; Liyu, A.; Gehm, M. E.; Browning, N. D. A Sub-Sampled Approach to Extremely Low-Dose STEM. *Appl. Phys. Lett.* **2018**, *112*, 043104.
- (330) Kisielowski, C. Observing Atoms at Work by Controlling Beam–Sample Interactions. *Adv. Mater.* **2015**, *27*, 5838–5844.
- (331) Hachtel, J. A.; Idrobo, J. C.; Chi, M. Sub-Ångstrom Electric Field Measurements on a Universal Detector in a Scanning Transmission Electron Microscope. *Adv. Struct. Chem. Imaging* **2018**, *4*, 10–16.
- (332) Li, Y.; Li, Y.; Pei, A.; Yan, K.; Sun, Y.; Wu, C.-L.; Joubert, L.-M.; Chin, R.; Koh, A. L.; Yu, Y.; Perrino, J.; Butz, B.; Chu, S.; Cui, Y. Atomic Structure of Sensitive Battery Materials and Interfaces Revealed by Cryo–Electron Microscopy. *Science* **2017**, *358*, 506–510.
- (333) Wang, X.; Zhang, M.; Alvarado, J.; Wang, S.; Sina, M.; Lu, B.; Bouwer, J.; Xu, W.; Xiao, J.; Zhang, J.-G.; Liu, J.; Meng, Y. S. New Insights on the Structure of Electrochemically Deposited Lithium Metal and Its Solid Electrolyte Interphases *via* Cryogenic TEM. *Nano Lett.* **2017**, *17*, 7606–7612.
- (334) Hwang, S.; Han, C. W.; Venkatakrisnan, S. V.; Bouman, C. A.; Ortalan, V. Towards the Low-Dose Characterization of Beam Sensitive Nanostructures *via* Implementation of Sparse Image Acquisition in Scanning Transmission Electron Microscopy. *Meas. Sci. Technol.* **2017**, *28*, 045402.
- (335) Kovarik, L.; Stevens, A.; Liyu, A.; Browning, N. D. Implementing an Accurate and Rapid Sparse Sampling Approach for Low-Dose Atomic Resolution STEM Imaging. *Appl. Phys. Lett.* **2016**, *109*, 164102.
- (336) Stevens, A.; Kovarik, L.; Abellan, P.; Yuan, X.; Carin, L.; Browning, N. D. Applying Compressive Sensing to TEM Video: A Substantial Frame Rate Increase on any Camera. *Adv. Struct. Chem. Imaging* **2015**, *1*, 10.
- (337) Stevens, A.; Yang, H.; Carin, L.; Arslan, I.; Browning, N. D. The Potential for Bayesian Compressive Sensing to Significantly Reduce Electron Dose in High-Resolution STEM Images. *Microscopy* **2014**, *63*, 41–51.
- (338) Sang, X.; Lupini, A. R.; Unocic, R. R.; Chi, M.; Borisevich, A. Y.; Kalinin, S. V.; Endeve, E.; Archibald, R. K.; Jesse, S. Dynamic Scan Control in STEM: Spiral Scans. *Adv. Struct. Chem. Imaging* **2016**, *2*, 6–14.
- (339) Li, X.; Dyck, O.; Kalinin, S. V.; Jesse, S. Compressed Sensing of Scanning Transmission Electron Microscopy (STEM) with Nonrectangular Scans. *Microsc. Microanal.* **2018**, *24*, 623–633.

- (340) Unocic, R. R.; Lupini, A. R.; Borisevich, A. Y.; Cullen, D. A.; Kalinin, S. V.; Jesse, S. Direct-Write Liquid Phase Transformations with a Scanning Transmission Electron Microscope. *Nanoscale* **2016**, *8*, 15581–15588.
- (341) Jesse, S.; He, Q.; Lupini, A. R.; Leonard, D. N.; Oxley, M. P.; Ovchinnikov, O.; Unocic, R. R.; Tselev, A.; Fuentes-Cabrera, M.; Sumpter, B. G.; Pennycook, S. J.; Kalinin, S. V.; Borisevich, A. Y. Atomic-Level Sculpting of Crystalline Oxides: Toward Bulk Nanofabrication with Single Atomic Plane Precision. *Small* **2015**, *11*, 5895–5900.
- (342) Egerton, R. F. Radiation Damage to Organic and Inorganic Specimens in the TEM. *Micron* **2019**, *119*, 72–87.
- (343) Chen, J. K.; Tzou, D. Y.; Beraun, J. E. A Semiclassical Two-Temperature Model for Ultrafast Laser Heating. *Int. J. Heat Mass Transfer* **2006**, *49*, 307–316.
- (344) Rau, H. *Photochemistry and Photophysics*; Rabek, J. F., Ed.; CRC Press: Boca Raton, FL, 1990; Vol., pp 119–141.
- (345) Inokuti, M. Inelastic Collisions of Fast Charged Particles with Atoms and Molecules—The Bethe Theory Revisited. *Rev. Mod. Phys.* **1971**, *43*, 297–347.
- (346) Lingerfelt, D.; Ganesh, P.; Jakowski, J.; Sumpter, B. G. First Principles Determination of Electronic Excitations Induced by Charged Particles. 2019, https://chemrxiv.org/articles/First_Principles_Determination_of_Electronic_Excitations_Induced_by_Charged_Particles/7726139 (Accessed September 3, 2019).
- (347) Tsubonoya, K.; Hu, C.; Watanabe, K. Time-Dependent Density-Functional Theory Simulation of Electron Wave-Packet Scattering With Nanoflakes. *Phys. Rev. B: Condens. Matter Mater. Phys.* **2014**, *90*, 035416.
- (348) Cohen, A. J.; Mori-Sánchez, P.; Yang, W. Insights into Current Limitations of Density Functional Theory. *Science* **2008**, *321*, 792–794.
- (349) Schlünzen, N.; Hermanns, S.; Bonitz, M.; Verdozzi, C. Dynamics of Strongly Correlated Fermions: *Ab Initio* Results for Two and Three Dimensions. *Phys. Rev. B: Condens. Matter Mater. Phys.* **2016**, *93*, 035107.
- (350) Peng, W.-T.; Fales, B. S.; Levine, B. G. Simulating Electron Dynamics of Complex Molecules with Time-Dependent Complete Active Space Configuration Interaction. *J. Chem. Theory Comput.* **2018**, *14*, 4129–4138.
- (351) Sato, T.; Ishikawa, K. L. Time-Dependent Complete-Active-Space Self-Consistent-Field Method for Multielectron Dynamics in Intense Laser Fields. *Phys. Rev. A: At., Mol., Opt. Phys.* **2013**, *88*, 023402.
- (352) Saldin, D. K.; Ueda, Y. Dipole Approximation in Electron-Energy-Loss Spectroscopy: L-Shell Excitations. *Phys. Rev. B: Condens. Matter Mater. Phys.* **1992**, *46*, 5100–5109.
- (353) Izmaylov, A. F.; Mendive-Tapia, D.; Bearpark, M. J.; Robb, M. A.; Tully, J. C.; Frisch, M. J. Nonequilibrium Fermi Golden Rule for Electronic Transitions Through Conical Intersections. *J. Chem. Phys.* **2011**, *135*, 234106.
- (354) Lee, S.; Oshima, Y.; Hosono, E.; Zhou, H.; Kim, K.; Chang, H. M.; Kanno, R.; Takayanagi, K. *In Situ* TEM Observation of Local Phase Transformation in a Rechargeable LiMn₂O₄ Nanowire Battery. *J. Phys. Chem. C* **2013**, *117*, 24236–24241.
- (355) Gong, Y.; Zhang, J.; Jiang, L.; Shi, J.-A.; Zhang, Q.; Yang, Z.; Zou, D.; Wang, J.; Yu, X.; Xiao, R.; Hu, Y.-S.; Gu, L.; Li, H.; Chen, L. *In Situ* Atomic-Scale Observation of Electrochemical Delithiation Induced Structure Evolution of LiCoO₂ Cathode in a Working All-Solid-State Battery. *J. Am. Chem. Soc.* **2017**, *139*, 4274–4277.
- (356) Kim, S.-W.; Lee, H.-W.; Muralidharan, P.; Seo, D.-H.; Yoon, W.-S.; Kim, D. K.; Kang, K. Electrochemical Performance and *Ex Situ* Analysis of ZnMn₂O₄ Nanowires as Anode Materials for Lithium Rechargeable Batteries. *Nano Res.* **2011**, *4*, 505–510.
- (357) Santhanagopalan, D.; Qian, D.; McGilvray, T.; Wang, Z.; Wang, F.; Camino, F.; Graetz, J.; Dudney, N.; Meng, Y. S. Interface Limited Lithium Transport in Solid-State Batteries. *J. Phys. Chem. Lett.* **2014**, *5*, 298–303.
- (358) Stevens, A.; Yang, H.; Hao, W.; Jones, L.; Ophus, C.; Nellist, P. D.; Browning, N. D. Subsampled STEM-Ptychography. *Appl. Phys. Lett.* **2018**, *113*, 033104.
- (359) Borisevich, A. Y.; Lupini, A. R.; Pennycook, S. J. Depth Sectioning with the Aberration-Corrected Scanning Transmission Electron Microscope. *Proc. Natl. Acad. Sci. U. S. A.* **2006**, *103*, 3044–3048.
- (360) Borisevich, A. Y.; Lupini, A. R.; Travaglini, S.; Pennycook, S. J. Depth Sectioning of Aligned Crystals with the Aberration-Corrected Scanning Transmission Electron Microscope. *J. Electron Microsc.* **2006**, *55*, 7–12.
- (361) Ishikawa, R.; Lupini, A. R.; Hinuma, Y.; Pennycook, S. J. Large-Angle Illumination STEM: Toward Three-Dimensional Atom-By-Atom Imaging. *Ultramicroscopy* **2015**, *151*, 122–129.
- (362) van Benthem, K.; Lupini, A. R.; Kim, M.; Baik, H. S.; Doh, S.; Lee, J.-H.; Oxley, M. P.; Findlay, S. D.; Allen, L. J.; Luck, J. T.; Pennycook, S. J. Three-Dimensional Imaging of Individual Hafnium Atoms Inside a Semiconductor Device. *Appl. Phys. Lett.* **2005**, *87*, 034104.
- (363) van Benthem, K.; Lupini, A. R.; Oxley, M. P.; Findlay, S. D.; Allen, L. J.; Pennycook, S. J. Three-Dimensional ADF Imaging of Individual Atoms by Through-Focal Series Scanning Transmission Electron Microscopy. *Ultramicroscopy* **2006**, *106*, 1062–1068.
- (364) Jang, J. H.; Kim, Y.-M.; He, Q.; Mishra, R.; Qiao, L.; Biegalski, M. D.; Lupini, A. R.; Pantelides, S. T.; Pennycook, S. J.; Kalinin, S. V.; Borisevich, A. Y. *In Situ* Observation of Oxygen Vacancy Dynamics and Ordering in the Epitaxial LaCoO₃ System. *ACS Nano* **2017**, *11*, 6942–6949.
- (365) Kotakoski, J.; Mangler, C.; Meyer, J. C. Imaging Atomic-Level Random Walk of a Point Defect in Graphene. *Nat. Commun.* **2014**, *5*, 3991–3999.
- (366) Ishikawa, R.; Mishra, R.; Lupini, A. R.; Findlay, S. D.; Taniguchi, T.; Pantelides, S. T.; Pennycook, S. J. Direct Observation of Dopant Atom Diffusion in a Bulk Semiconductor Crystal Enhanced by a Large Size Mismatch. *Phys. Rev. Lett.* **2014**, *113*, 155501.
- (367) Dyck, O.; Kim, S.; Kalinin, S. V.; Jesse, S. Placing Single Atoms in Graphene with a Scanning Transmission Electron Microscope. *Appl. Phys. Lett.* **2017**, *111*, 113104.
- (368) Susi, T.; Kepaptsoglou, D.; Lin, Y.-C.; Ramasse, Q. M.; Meyer, J. C.; Suenaga, K.; Kotakoski, J. Towards Atomically Precise Manipulation of 2D Nanostructures in the Electron Microscope. *2D Mater.* **2017**, *4*, 042004.
- (369) Tripathi, M.; Mittelberger, A.; Pike, N. A.; Mangler, C.; Meyer, J. C.; Verstraete, M. J.; Kotakoski, J.; Susi, T. Electron-Beam Manipulation of Silicon Dopants in Graphene. *Nano Lett.* **2018**, *18*, 5319–5323.
- (370) Dyck, O.; Kim, S.; Jimenez-Izal, E.; Alexandrova, A. N.; Kalinin, S. V.; Jesse, S. Building Structures Atom by Atom via Electron Beam Manipulation. *Small* **2018**, *14*, 1801771.
- (371) Carrasquilla, J.; Melko, R. G. Machine Learning Phases of Matter. *Nat. Phys.* **2017**, *13*, 431–38.
- (372) van Nieuwenburg, E. P. L.; Liu, Y.-H.; Huber, S. D. Learning Phase Transitions by Confusion. *Nat. Phys.* **2017**, *13*, 435–439.
- (373) Gómez-Bombarelli, R.; Wei, J. N.; Duvenaud, D.; Hernández-Lobato, J. M.; Sánchez-Lengeling, B.; Sheberla, D.; Aguilera-Iparraguirre, J.; Hirzel, T. D.; Adams, R. P.; Aspuru-Guzik, A. Automatic Chemical Design Using a Data-Driven Continuous Representation of Molecules. *ACS Cent. Sci.* **2018**, *4*, 268–276.
- (374) Baldi, P.; Sadowski, P.; Whiteson, D. Searching for Exotic Particles in High-Energy Physics with Deep Learning. *Nat. Commun.* **2014**, *5*, 4308–4314.
- (375) Ziatdinov, M.; Maksov, A.; Kalinin, S. V. Learning Surface Molecular Structures via Machine Vision. *NPJ. Comput. Mater.* **2017**, *3*, 31–43.
- (376) Ziatdinov, M.; Dyck, O.; Maksov, A.; Li, X.; Sang, X.; Xiao, K.; Unocic, R. R.; Vasudevan, R.; Jesse, S.; Kalinin, S. V. Deep Learning of Atomically Resolved Scanning Transmission Electron Microscopy Images: Chemical Identification and Tracking Local Transformations. *ACS Nano* **2017**, *11*, 12742–12752.

- (377) Madsen, J.; Liu, P.; Kling, J.; Wagner, J. B.; Hansen, T. W.; Winther, O.; Schiøtz, J. A Deep Learning Approach to Identify Local Structures in Atomic-Resolution Transmission Electron Microscopy Images. *Adv. Theory Simul.* **2018**, *1*, 1800037.
- (378) Maksov, A.; Dyck, O.; Wang, K.; Xiao, K.; Geohegan, D. B.; Sumpter, B. G.; Vasudevan, R. K.; Jesse, S.; Kalinin, S. V.; Ziatdinov, M. Deep Learning Analysis of Defect and Phase Evolution During Electron Beam-Induced Transformations in WS₂. *NPJ. Comput. Mater.* **2019**, *5*, 12.
- (379) Goodfellow, I.; Bengio, Y.; Courville, A. *Deep Learning*; MIT Press: Cambridge, MA, 2016.
- (380) Long, J.; Shelhamer, E.; Darrell, T. Fully Convolutional Networks for Semantic Segmentation. Proceedings from the 2015 *IEEE Conference on Computer Vision and Pattern Recognition (CVPR)*, Boston, MA, June 7–12, 2015; IEEE: New York, 2015; pp 3431–3440.
- (381) Barthel, J. Dr. Probe: A Software for High-Resolution STEM Image Simulation. *Ultramicroscopy* **2018**, *193*, 1–11.
- (382) Ziatdinov, M.; Dyck, O.; Maksov, A.; Hudak, B. M.; Lupini, A. R.; Song, J.; Snijders, P. C.; Vasudevan, R. K.; Jesse, S.; Kalinin, S. V., Deep Analytics of Atomically-Resolved Images: Manifest and Latent Features. 2018, <https://arxiv.org/abs/1801.05133> (Accessed September 3, 2019).
- (383) Dyck, O.; Ziatdinov, M.; Lingerfelt, D. B.; Unocic, R. R.; Hudak, B. M.; Lupini, A. R.; Jesse, S.; Kalinin, S. V. Atom-by-Atom Fabrication with Electron Beams. *Nat. Rev. Mater.* **2019**, *4*, 497–507.
- (384) Wang, Z.; Bovik, A.C.; Sheikh, H.R.; Simoncelli, E.P. Image Quality Assessment: from Error Visibility to Structural Similarity. *IEEE Trans. Image Process.* **2004**, *13*, 600–612.
- (385) Lin, W.; Li, Q.; Belianinov, A.; Sales, B. C.; Sefat, A.; Gai, Z.; Baddorf, A. P.; Pan, M.; Jesse, S.; Kalinin, S. V. Local Crystallography Analysis for Atomically Resolved Scanning Tunneling Microscopy Images. *Nanotechnology* **2013**, *24*, 415707.
- (386) Vasudevan, R. K.; Laanait, N.; Ferragut, E. M.; Wang, K.; Geohegan, D. B.; Xiao, K.; Ziatdinov, M.; Jesse, S.; Dyck, O.; Kalinin, S. V. Mapping Mesoscopic Phase Evolution During e-Beam Induced Transformations via Deep Learning of Atomically Resolved Images. *NPJ. Comput. Mater.* **2018**, *4*, 30–38.
- (387) Ziatdinov, M.; Dyck, O.; Sumpter, B. G.; Jesse, S.; Vasudevan, R. K.; Kalinin, S. V., Building and Exploring Libraries of Atomic Defects in Graphene: Scanning Transmission Electron and Scanning Tunneling Microscopy Study. 2019, <https://arxiv.org/abs/1809.04256> (Accessed September 3, 2019).
- (388) Ross, D.; Strychalski, E. A.; Jarzynski, C.; Stavis, S. M. Equilibrium Free Energies from Non-Equilibrium Trajectories with Relaxation Fluctuation Spectroscopy. *Nat. Phys.* **2018**, *14*, 842–847.
- (389) Vlcek, L.; Vasudevan, R. K.; Jesse, S.; Kalinin, S. V. Consistent Integration of Experimental and *Ab Initio* Data Into Effective Physical Models. *J. Chem. Theory Comput.* **2017**, *13*, 5179–5194.
- (390) Vlcek, L.; Ziatdinov, M.; Maksov, A.; Tselev, A.; Baddorf, A. P.; Kalinin, S. V.; Vasudevan, R. K. Learning from Imperfections: Predicting Structure and Thermodynamics from Atomic Imaging of Fluctuations. *ACS Nano* **2019**, *13*, 718–727.
- (391) Vlcek, L.; Maksov, A.; Pan, M.; Vasudevan, R. K.; Kalinin, S. V. Knowledge Extraction from Atomically Resolved Images. *ACS Nano* **2017**, *11*, 10313–10320.
- (392) Wootters, W. K. Statistical Distance and Hilbert Space. *Phys. Rev. D: Part. Fields* **1981**, *23*, 357–368.
- (393) Goodfellow, I.; Pouget-Abadie, J.; Mirza, M.; Xu, B.; Warde-Farley, D.; Ozair, S.; Courville, A.; Bengio, Y. Advances in Neural Information Processing Systems. In *Generative Adversarial Nets*; Neural Information Processing Systems: San Diego, CA, 2014; pp 2672–2680.
- (394) Lillicrap, T. P.; Hunt, J. J.; Pritzel, A.; Heess, N.; Erez, T.; Tassa, Y.; Silver, D.; Wierstra, D., Continuous Control with Deep Reinforcement Learning. **2015**, <https://arxiv.org/abs/1509.02971> (Accessed September 3, 2019).
- (395) Jesse, S.; Hudak, B. M.; Zarkadoula, E.; Song, J.; Maksov, A.; Fuentes-Cabrera, M.; Ganesh, P.; Kravchenko, I.; Snijders, P. C.; Lupini, A. R.; Borisevich, A. Y.; Kalinin, S. V. Direct Atomic Fabrication and Dopant Positioning in Si Using Electron Beams with Active Real-Time Image-Based Feedback. *Nanotechnology* **2018**, *29*, 255303.
- (396) Hudak, B. M.; Song, J.; Sims, H.; Troparevsky, M. C.; Humble, T. S.; Pantelides, S. T.; Snijders, P. C.; Lupini, A. R. Directed Atom-by-Atom Assembly of Dopants in Silicon. *ACS Nano* **2018**, *12*, 5873–5879.
- (397) Wu, H.; Zhao, X.; Guan, C.; Zhao, L.-D.; Wu, J.; Song, D.; Li, C.; Wang, J.; Loh, K. P.; Venkatesan, T. V.; Pennycook, S. J. The Atomic Circus: Small Electron Beams Spotlight Advanced Materials Down to the Atomic Scale. *Adv. Mater.* **2018**, *30*, 1802402.
- (398) Jiang, N.; Zarkadoula, E.; Narang, P.; Maksov, A.; Kravchenko, I.; Borisevich, A.; Jesse, S.; Kalinin, S. V. Atom-By-Atom Fabrication by Electron Beam via Induced Phase Transformations. *MRS Bull.* **2017**, *42*, 653–659.
- (399) Kalinin, S. V.; Pennycook, S. J. Single-Atom Fabrication with Electron and Ion Beams: from Surfaces and Two-Dimensional Materials Toward Three-Dimensional Atom-By-Atom Assembly. *MRS Bull.* **2017**, *42*, 637–643.
- (400) Mishra, R.; Ishikawa, R.; Lupini, A. R.; Pennycook, S. J. Single-Atom Dynamics in Scanning Transmission Electron Microscopy. *MRS Bull.* **2017**, *42*, 644–652.
- (401) Zhao, X.; Kotakoski, J.; Meyer, J. C.; Sutter, E.; Sutter, P.; Krashenninnikov, A. V.; Kaiser, U.; Zhou, W. Engineering and Modifying Two-Dimensional Materials by Electron Beams. *MRS Bull.* **2017**, *42*, 667–676.
- (402) Gonzalez-Martinez, I.; Bachmatiuk, A.; Bezugly, V.; Kunstmann, J.; Gemming, T.; Liu, Z.; Cuniberti, G.; Rummeli, M. Electron-Beam Induced Synthesis of Nanostructures: a Review. *Nanoscale* **2016**, *8*, 11340–11362.
- (403) Mendes, R. G.; Pang, J.; Bachmatiuk, A.; Ta, H. Q.; Zhao, L.; Gemming, T.; Fu, L.; Liu, Z.; Rummeli, M. H. Electron-Driven *in Situ* Transmission Electron Microscopy of 2D Transition Metal Dichalcogenides and Their 2D Heterostructures. *ACS Nano* **2019**, *13*, 978–995.
- (404) Zhao, X.; Dan, J.; Chen, J.; Ding, Z.; Zhou, W.; Loh, K. P.; Pennycook, S. J. Atom-by-Atom Fabrication of Monolayer Molybdenum Membranes. *Adv. Mater.* **2018**, *30*, 1707281.
- (405) Susi, T.; Meyer, J. C.; Kotakoski, J. Manipulating Low-Dimensional Materials Down to the Level of Single Atoms with Electron Irradiation. *Ultramicroscopy* **2017**, *180*, 163–172.
- (406) Lin, J.; Cretu, O.; Zhou, W.; Suenaga, K.; Prasai, D.; Bolotin, K. I.; Cuong, N. T.; Otani, M.; Okada, S.; Lupini, A. R.; Idrobo, J.-C.; Caudel, D.; Burger, A.; Ghimire, N. J.; Yan, J.; Mandrus, D. G.; Pennycook, S. J.; Pantelides, S. T. Flexible Metallic Nanowires with Self-Adaptive Contacts to Semiconducting Transition-Metal Dichalcogenide Monolayers. *Nat. Nanotechnol.* **2014**, *9*, 436–445.